This is to certify that the

dissertation entitled

A Fundamental Study of K_2CO_3
Catalysis of Hydrogasification of Carbon
and the Role of Oxygen in the Catalysis

presented by

Hossein Zoheidi

has been accepted towards fulfillment
of the requirements for

Ph.D. degree in CHE

Dennis J. Miller
Major professor

Date 8/27/87

A FUNDAMENTAL STUDY OF K_2CO_3 CATALYSIS OF HYDROGASIFICATION OF CARBON AND THE ROLE OF OXYGEN IN THE CATALYSIS

By

Hossein Zoheidi

A DISSERTATION

Submitted to
Michigan State University
in partial fulfillment of the requirements
for the degree of

DOCTOR OF PHILOSOPHY

Department of Chemical Engineering

1987

ABSTRACT

A FUNDAMENTAL STUDY OF K_2CO_3-CATALYSIS OF HYDROGASIFICATION OF CARBON AND THE ROLE OF OXYGEN IN THE CATALYSIS

By

Hossein Zoheidi

The existing and projected shortages of natural gas in the United States have stimulated extensive research on production of synthetic natural gas (SNG) from coal, the largest fossil fuel resource in this country. Potassium carbonate has been identified as the most economically attractive catalyst for gasification. In this process, coal is reacted with steam to produce a mixture of CO and H_2. The product hydrogen can further react with either CO or coal to produce methane. However, understanding the mechanism is complicated by the reported strong retardation effect of product hydrogen on the kinetics of both uncatalyzed and the catalyzed steam gasification. This retardation effect and the catalyzed reaction of product hydrogen with carbon are relatively unexplored and are not fully understood.

Recently, studies have suggested that the catalyzed steam gasification rates are directly proportional to coverage of carbon surface by oxygen complexes, and that reaction of carbon with hydrogen is enhanced by the presence of oxygen, implying that interaction of K_2CO_3 and hydrogen with these surface complexes may be the key to understanding the mechanism of the retardation effect and hydrogasification.

In this work, therefore, fundamental experimental kinetic studies of K_2CO_3-catalyzed and non-catalyzed hydrogasification of carbon blacks at 700-865 °C and 500 psi hydrogen pressure have been conducted to gain more insight into the role of K_2CO_3 and oxygen complexes. In these studies, the effects of different catalyst loadings on hydrogasification rate, potassium loss at high temperature, the nature of oxygen

complexes in carbon black, and effects of oxygen chemisorption at 400° and 800°C and/or degassing at 1000°C on non-catalyzed and the catalyzed hydrogasification have been investigated.

From the effect of various oxygen surface groups on rate of hydrogasification, it is postulated that oxygen groups thermally desorb from the carbon surface and create 'nascent' active sites which act as active sites for hydrogasification, hence enhancing the reactivity of the carbon. K_2CO_3 catalytic activity and potassium losses are influenced by the nature of oxygen surface groups. The formation of stable and active potassium-containing species via interaction of K_2CO_3 and oxygen complexes leads to reduced potassium losses and enhanced hydrogasification rates. The interaction of K_2CO_3 with carbonyl groups forms both stable and active species. Interaction with basic oxygen complexes, which are relatively inactive in uncatalyzed hydrogasification, form active but unstable intermediate species. Interaction with acidic complexes is not well characterized from the experiments. Degassing removes non-basic groups and thermally anneals the 'nascent' active sites, resulting in reduced gasification rate and increased potassium loss.

Dedication

I would like to dedicate this work to my parents, Hassan and Forough Zoheidi, who provided me with love and support and gave me all I have, my brothers Mohammad Ali and Hammeed and my sisters, Afsauneh, Elauheh and Parvauneh. They made this work possible with their continued support and encouragement.

Acknowledgments

I would like to take this opportunity to express my gratitude to Dr. Dennis J. Miller, the chairman of my doctoral committee, for his guidance and support throughout this work, and Prof. Charles A. Petty for invaluable and constructive comments and suggestions during the preparation of this document. My thanks to Prof. Martin C. Hawley and Prof. Thomas J. Pinnavaia for kindly accepting the unpleasant duty of serving on my doctoral committee.

I wish to thank all of my good and valuable friends, in particular, Dr. Alireza Abbasabadi, Dr. Nikrouz Faroughi, Dr. Hamid Ghods, Dr. Touran Cheraghi, Mehrnam Sharif, Partash Moallemian, Sun (Natasha) Yong Hong, Javad Kalantar, and Farzin Khorasanizadeh, who bestowed me with nothing but their encouragement, understanding, patience and forgiveness. Thank you all for tolerating me during the hard period of consummating this work.

I would also like to thank the Department of Chemical Engineering at Michigan State University for supporting me financially through most of this work.

Finally, I would like to Thank Dr. Klaus Otto at Ford Motor Company for carrying out the XPS analysis and Mr. Xiao-Wen Qian at the Department of Physics at Michigan State University for providing the XRD analysis. Their help is greatly appreciated.

Table of Contents

List of Tables

List of Figures

Nomenclature

A = total heat transfer surface area in cooling coils, ft^2
A' = flange ring design parameter, see Eq. A-1
A'' = flange ring design parameter, see Eq. A-1
A_c = internal cross sectional area of copper cooling coils, in^2
A_{rw} = cross sectional area of reactor wall, in^2
A_{rd} = cross sectional area of rupture disc, in^2
A_t = atomic weight
a = constant
b = constant
C = flow constant of gases through rupture disc
C_A = molar concentration of reacting component A, $mole/cm^3$
C_p = specific heat capacity of cooling water, Btu/lb_m-°F
$C_{p,i}$ = specific heat capacity of the ith component of a reaction mixture, cal/g mole-°K
D_{AB} = gaseous binary diffusivity of H_2–CH_4 system, cm^2/sec
D_K = Knudsen diffusion coefficient, cm^2/sec
D_e = effective diffusivity, cm^2/sec
D_i = inside diameter of reactor vessel, in
D_d = diameter of γ-ray detector crystal. in
D_o = outside diameter of reactor vessel, in
d = inside diameter of cooling coils, in
E = Young modulus of elasticity, psi
E_a = intrinsic activation energy, kcal/g-mole
E_a' = apparent activation energy, kcal/g-mole
E_γ = γ-ray energy, MeV
f = fraction of potassium lost from a sample
f_d = fraction of surface covered by detector crystal
f_l = fraction of γ-ray radiation passing through shielding layers
G = shearing modulus of elasticity, psi
h_o = heat transfer coefficient, Btu/ft^2-h-°F
K = constant, set to 0.62 by ASME Code when rupture disc is the sole relieving device
K_p = equilibrium constant
K_1 = ratio of r_1 to r_0
k = ratio of specific heats
k_{CH_4} = rate constant of uncatalyzed hydrogasification, sec^{-1}
k^1_{rxn} = rate constant of a first order reaction, sec^{-1}
k^2_{rxn} = rate constant of a second order reaction, cm^3/gmole-sec
k_1 = constant
k_2 = constant
k_3 = constant
k_4 = constant
L = distance from cooling coils to furnace inlet, in
L_a = X-ray width of microcrystallites of carbon black, Å
L_c = X-ray height of microcrystallites of carbon black, Å
L_{cc} = length of cooling coils, ft
L_d = distance between sample and γ-ray detector crystal, in
M = total mass of potassium at any time, g
M_o = total initial mass of potassium, g
m = mass flow rate of cooling water, lb_m/h
$\dot{m}$ = mass flux of cooling water inside cooling coils, lb_m/in^2-h

N_{avo} = Avogadro's number, 6.023×10^{23} atoms/g-mole
N^{41} = number of atoms of ^{41}K at time t
N^{42} = number of atoms of ^{42}K at time t
N_o^{41} = initial number of atoms of ^{41}K
N_o^{42} = initial number of atoms of ^{42}K
n = number of major metal components in Haynes-25
P = effective load on flange, psi
p = reactor vessel total internal pressure, psi
p_e = exhaust pressure of rupture disc, psi
p_{H_2} = hydrogen partial pressure, psi
p_{CH_4} = methane partial pressure, psi
Q = total axial heat flow in reactor wall, Btu/h
Q_v = volumetric flow rate of gases through rupture disc, SCFM
q = axial heat flux in reactor wall, Btu/(in^2-h)
R = universal gas constant, cm^3-atm/mole-°K
$\overline{R}$ = rate of nuclear disintegration of ^{42}K nuclei in a sample, d/s
R = measured rate of nuclear disintegration of ^{42}K nuclei by γ-ray detector, d/s
R_{CH_4} = rate of evolution of methane, gmole CH_4/cm^3-sec
R_e = Reynolds number, dimensionless
R_h = hydraulic radius, cm
R_{rxn} = rate of reaction, gmole/cm^3-sec
r = radial distance from the central axis of reactor, in
r_e = mean radius of pores in a carbon black particle, cm
r_i = inside radius, in
r_o = outside radius, in
r_0 = inside radius of flage ring, in
r_1 = radius of bolt circle, in
S = total surface area of carbon black particles, cm^2/g
s = inverse of Poisson's ratio μ
T = temperature of reactor wall, °F
T_f = temperature of furnace, °F
T_m = room temperature, °F
T_i = inlet temperature of cooling water, °F
T_o = outlet temperature of cooling water, °F
T_{rxn} = reaction temperature, °K
t = time elapsed after the end of neutron bombardment, h
t_a = period of neutron bombardment of potassium atoms, h
U = flange ring design parameter which is 1 at weakest spot of flang ring
v_i = volume fraction of ith elemental component of Haynes-25
V = volume of a control element, in^3
W = molecular weight, g/mole
W_H = hydrogen molecular weight, 2.016 g/mole
W_{CH_4} = methane molecular weight, 16.043 g/mole
W_K = potassium molecular weight, 39.102 g/mole
x = fraction of carbon gasified
x = thickness of γ-ray shielding material, cm
x_{eq} = fraction of hydrogen converted to methane at equilibrium
y = flange ring deflection under stress, in
y_{CH_4} = methane mole fraction
Z = atomic number
z = distance along the central axis of reactor, in

Greek

α = thermal expansion coefficient, in/(in - °F)
Γ = Gamma constant of γ-ray radiation
ΔC_p = $\sum_i \nu_i C_{p,i}$
ΔH = heat of reaction, kcal/g mole
$\Delta H_{25 \cdot C}$ = heat of reaction at 25 °C, kcal/g mole
ΔpH = change in pH of a solution induced by carbon black oxygen surface groups
ΔT = heat transfer driving force in cooling coils, °F
ΔT_c = temperature rise of cooling water in cooling coils, °F
ΔT_{ln} = log-mean temperature difference, °F
Δr = radial thickness of a control shell, in
Δz = axial length of a control shell, in
ϵ = $ln\,2/t_{½}$ proportionality constant of radiation and mass, h^{-1}
ϵ_c = porosity of a carbon black particle
ϵ_p = porosity of carbon bed
ς = thickness of the reactor wall, in
ς_f = thickness of flange ring, in
ς_h = thickness of closed end of the reactor vessel, in
η = cross section of ^{41}K atom for neutron absorption, 1.5×10^{-24} cm^2
κ = thermal conductivity of reactor wall, Btu-in/ft^2-h-°F
κ_c = thermal conducitvity of cooling water, Btu/ft-h-°F
Λ = attenuation coefficient of γ-ray shielding material, cm^{-1}
λ = attenuation coefficient of pure elements, cm^{-1}
μ = Poisson's ratio
μ_v = viscosity, lb_m/in-h
ν = absorption coefficient of photoelectric effect, cm^{-1}
ν_i = stoichiometric coefficient of the ith component of a reaction mixture
ξ = compton scattering absorption coefficient, cm^{-1}
ρ = density, g/ml
σ_{max} = maximum overall normal stress, psi
σ_r = radial stress, psi
$\sigma_{rupture}$ = tensile rupture stress, psi
σ_z = longitudinal stress, psi
σ_θ = circumferential or tangential stress, psi
τ_t = tortuosity factor of carbon bed
τ_θ = circumferential or tangential shear stress, psi
τ_z = longitudinal shear stress, psi
τ_{zr} = radial shear stress induced from z-direction, psi
Φ = neutron flux, neutrons/cm^2-s
ϕ = Thiele modulus
χ = mass fraction of total potassium as ^{41}K

Chapter 1

Introduction & Background

In the United States, it has been realized for the last two decades that the natural gas resources (*e.g.* methane) are being depleted at a rate faster than it is possible to replace by nature, and the estimated reserves of some 2500 trillion cubic feet (in 1974) could easily be depleted by the turn of the century. These existing and projected shortages have stimulated extensive research to find viable alternatives and to develop the technology for commercial production of synthetic high BTU gases. Imported liquid natural gas can ease shortages, but it is much more expensive than natural gas (5-10 times) [1].

In this general effort, one of the most logical alternatives is to convert coal, the largest fossil fuel resource in this country, to gas and oil. Gasification of coal with steam is such a process, and today the technology for commercial

production of synthetic natural gas (SNG) exists, albeit possibly not in the most economical or elegant way. In this process, coal is reacted with steam to produce a mixture of CO and H_2 (synthesis gas)

$$C + H_2O \rightarrow H_2 + CO \tag{1-1}$$

which can subsequently undergo nickel-catalyzed methanation reaction

$$CO + 3H_2 \rightarrow CH_4 + H_2O \tag{1-2}$$

or, alternatively, the product hydrogen gas can directly react with carbon to produce methane

$$C + 2H_2 \rightarrow CH_4 \tag{1-3}$$

The products of these reactions can further react with steam, coal or other reaction products in secondary reactions:

$$CO + H_2O \rightarrow H_2 + CO_2 \tag{1-4}$$

$$CO_2 + 4H_2 \rightarrow CH_4 + 2H_2O \tag{1-5}$$

$$2CO \rightarrow C + CO_2 \tag{1-6}$$

Reactions 1-2, 1-3 and 1-5 produce the highly desirable methane and all are exothermic [1,2].

Therefore, the gasifier effluent gas stream is a mixture of H_2, H_2O, CO, CO_2 and CH_4, and its composition depends on the pressure and temperature inside the gasifier and on the catalyst used. The optimum reaction conditions are thus the conditions under which methane formation is maximized; *i.e.*, lower temperatures are favorable because of the exothermicity of Reactions 1-2, 1-3 and 5. In fact, it was the search for gasification conditions at lower temperatures (to favor methane formation) that led Exxon researchers and other investigators to explore the alkali-metal catalysis of steam gasification of coal, first realized more than a century ago [3].

As far as the catalytic activity is concerned, most transition metals of groups IIIB-VIIIB, such as nickel, are superior catalysts compared to alkali carbonates [4-7]. However, these metal catalysts are expensive and are easily poisoned by sulfur which is invariably present in coal. In contrast, alkali carbonates are not as effective, but are not poisoned severely by sulfur and are relatively cheaper and thus more attractive [8-10]. Among carbonates, catalytic activity increases with alkalinity; but, again the determining factor for commercial feasibility is cost effectiveness, or abundance in nature. In terms of abundance of the elements in earth's crust, sodium ranks sixth, and potassium at seventh is 90 times as plentiful as carbon [8]. Yet, potassium has more than enough activity relative to sodium to justify its somewhat higher cost. On the other hand, rubidium and cesium, though more active than potassium, are far too costly to be used commercially. Hence, potassium carbonate seems to be the most promising catalyst for any steam gasification of coal on a commercial scale.

To maximize gasifier throughput and to use potassium carbonate effectively it is essential to understand kinetics and mechanisms of various reactions taking place inside the gasifier and the influence of the catalyst on these reactions. A knowledge of mechanism and kinetics allows selection of optimum gasification conditions such as temperature, pressure, catalyst loadings, *etc.*, so that more economical processes and gasifiers can be designed. For instance, if the mechanism of catalyzed interaction of hydrogen with carbon is known, perhaps the strong retardation effect of hydrogen on reaction of steam with carbon [10-14] can be diminished and, at the same time, the rate of Reaction 1-3 can be enhanced significantly. This way, SNG (methane) could be produced at much higher rates and the process would be more economically attractive.

Catalysis of steam and carbon dioxide gasification by alkali carbonates, in particular K_2CO_3, has been studied extensively during the last few decades and several different mechanisms have been proposed. McKee *et al.* [15-18] have proposed a redox cycle which involves the decomposition and reformation of the carbonate on the surface of the carbon with the alkali oxide and hydroxide as intermediates in CO_2 and steam gasification, respectively. Veraa & Bell [19] and Huttinger & Minges [20] have supported this mechanism for steam gasification. Mims *et al.* [21,22,13] have believed that the formation of C-O-K complexes on the surface of the carbon is an essential step in the catalysis and thus determines the activity of the catalyst. Yuh & Wolf [23] have proposed a reduction-oxidation cycle involving these groups. Wood *et al.* [24,25] have postulated the formation of a non-stoichiometric oxide with excess alkali metal which acts as a center for extraction of oxygen from gaseous reactants and extraction of electrons from the carbon matrix, thus facilitating the reaction of adsorbed oxygen atoms [26]. Huttinger & Minges [14] have used this mechanism to

explain their steam gasification results, but have gone one step further and have suggested KOH as the active intermediate. Recently, Saber *et al.* [27] have concluded that presence of oxygen on the carbon surface is essential for the catalyst to remain active, implying that oxygen might be involved in the catalysis process. Wen [28] has outlined a mechanism involving formation of potassium-intercalation compounds of carbon. Wigmans *et al.* [29,30] have suggested that all three catalysis processes are simultaneously competing and dominate at different stages of the gasification.

Applications of FTIR [31], *in situ* FTIR [32,33], *in situ* e.s.r. [34,35] and EXAFS [36] have provided further support for each of the these proposed mechanisms. However, in spite of all these studies, and many similar ones employing a wide range of different techniques, the nature of active sites and the sequence of events are not yet fully understood.

Catalysis of hydrogasification is relatively unexplored compared to steam gasification. Much less attention has been given to this reaction and much less is known about the catalysis process, in spite of the fact that hydrogen is a product of steam gasification (Reaction 1-1) and is involved in an important step (Reaction 1-3) in production of SNG from coal. *A priori*, the above mentioned redox cycles cannot be accepted as reasonable mechanisms for hydrogasification, because the oxidizing gases (CO_2 or H_2O) which account for the oxidation step of these mechanisms are absent. This is further supported by the observation that hydrogen gas strongly inhibits the catalysis of steam gasification by alkali carbonates [10,14]. Thus, in the reducing environment of high temperature hydrogen gas, the driving force for maintaining these cycles operating is diminished if not completely eliminated.

Wood *et al.* [37] and Gardner *et al.* [38] have already shown that potassium carbonate can not only catalyze steam gasification but also catalyze reaction of hydrogen with carbon appreciably. The catalytic activity of K_2CO_3 in hydrogasification thus may arise via another reaction pathway or process. For uncatalyzed hydrogasification, Cao & Back [39] have shown that presence of oxygen in the gas stream enhances hydrogenation rate of pure carbon significantly and Blackwood [40] has related methane formation rate in pure hydrogen to oxygen content of a coconut char. However, the mechanism of this enhancement is not known. In addition, there has been no study on the influence of surface oxygen complexes on K_2CO_3 catalysis of hydrogasification.

The importance of oxygen in catalysis of steam gasification has only been realized very recently [27,41,42]. Hoshimoto *et al.* [41] have indicated that the rate of steam gasification is directly proportional to the amount of oxygen on carbon surface. In contrast, Sams *et al.* [42] have demonstrated that gasification rate is a function of potassium to carbon ratio only, and that heat treatment of carbon is immaterial. Saber *et al.* [27] have reconciled these findings by illustrating that the amount of potassium retained on carbon surface is indeed proportional to the amount of oxygen on carbon surface. Yet, no study has so far been done to examine the nature of oxygen groups in conjunction with their impact on catalysis process in steam gasification or hydrogasification.

The nature of oxygen containing groups on carbon surfaces has been the center of intensive studies for over six decades due to their important and vital impact on rubber reinforcing properties of carbon blacks. Numerous chemical techniques using different reagents have been devised to study the chemical behavior and hence the nature of these groups [43-48]. These studies have shown that a great part of the oxygen surface groups are chemically inert toward the reagents [46-48]. Aromatic ring-type ether groups have been proposed to

account for these inert groups [45,49]. The reactive part of the surface groups show acidic, basic or inert characteristics depending on the conditions under which they are formed [47] (acidic or basic in the sense that they neutralize dilute hydroxide solutions, such as NaOH or KOH, or dilute acid solutions such as HCl, respectively). For example, if carbon black is freed from all surface compounds by heating *in vacuo* followed by cooling in the absence of oxygen, its surface becomes covered with basic surface oxides upon exposure to oxygen [47]. It has also been found that oxidation at temperatures of 300-500 ° C establishes acidic groups on graphite [50], charcoal [51] and carbon blacks [52,53]. The nature of these acidic groups has been the source of great controversy. Different functional groups such as carboxyl and phenolic hydroxyl groups [47,48], a rather indefinite type of "CO_2-complex" [52], and lactone groups [40,49,54,55] have been proposed as the acidic surface complexes. These groups all decompose and give off CO_2 upon heating the carbon to higher temperatures. These studies have also shown that the amount of base neutralized by these groups is directly proportional to the amount of CO_2 evolved upon thermal decomposition. The optimum condition for the formation of these acidic groups has been suggested to be 400 ° C [43,51].

The oxygen surface groups formed at temperatures of 750 ° C or higher are predominantly basic in nature [56,57]. Pyrone-like structures [48] as well as benzpyran structures called chromenes [58] have been speculated to be responsible for the basicity of these surfaces; both thermally decompose to yield CO. It has been suggested that carbonyl groups also decompose to yield CO, but they are neutral in character [50]. The chromene structures are known to oxidize to lactones [58]. The chromene structures are also thought to be responsible for the low reactivity of residual chars toward hydrogen (to produce methane) at temperatures as high as 870 ° C [40]. These residual chars had lost

their highly active sites associated with lactone groups and temperatures above 1200 ° C were used to decompose their chromene groups completely.

Oxygen surface groups also play a key role in the wettability of the carbon surface. A well-cleaned graphitic carbon surface is essentially hydrophobic; the presence of oxygen complexes on some fraction of the surface renders that surface hydrophilic [59]. The wetting by water is due to the formation of hydrogen bonds both between the oxygen complexes on the surface and between the adsorbed molecules themselves [60].

As evident from the above literature survey (additional and more detailed and in depth review of the litrature will be given in the appropriate sections when seems necessary), various studies have concentrated on either just identifying the nature of oxygen surface complexes under isolated conditions or, at most, the influence of mere presence of oxygen on potassium retention. No study has yet been done to study the influence of 'different' oxygen complexes on potassium carbonate catalysis of either steam gasification or hydrogasification. Such a study is of vital importance since a knowledge of nature of the most active oxygen complex(es) would eventually provide more insight into the steps involved in the catalysis process and its mechanism.

The work presented here is an attempt to fill this gap. The study of the influence of different oxygen surface groups on alkali catalysis of hydrogasification (Reaction 1-3) of carbon blacks is the focus of the work presented here. Within this context, the influence of different oxygen groups on hydrogasification reaction in the absence of potassium carbonate is also reported and a mechanism is postulated. These fundamental studies of alkali carbonate-catalyzed hydrogasification of carbons are necessary to enhance our knowledge of the catalysis process and the nature of the active sites. Examination of similarities and differences in the behavior of the catalyst in

oxidizing and reducing environments will reveal more information about the steps involved in the catalysis process in oxidizing gasification as well as in hydrogen.

Chapter 2

Experimental Apparatus Design

2.1 Design Objectives

The design objectives are to design a complete high temperature/high pressure reactor system suited for gas-solid reaction kinetic studies. The heart of this system is a differential micro-reactor that can operate at 1000 ° C and 1000 psi pressure simultaneously and can handle severe oxidizing and reducing atmospheres of high temperature air and hydrogen gas, respectively. The operating temperature of 1000 ° C is chosen because this reactor is primarily to be used for gasification studies of carbons with hydrogen and, as will be discussed in Chapters 4 and 5, the previous studies have shown that temperatures above 700 ° C are needed to obtain reasonable reaction rates even for reactive chars and an additional temperature range of 100-150 ° C are

necessary to evaluate kinetic parameters such as activation energies. For graphite samples, which are the least reactive of carbons, even higher temperatures are necessary. Besides, degassing of carbon samples that is essential for studying of surface groups on carbons is traditionally done at temperatures higher than 950 ° C.

Gasification rates of carbons with hydrogen are much slower than those of other gas reactants such as steam or carbon dioxide and, therefore, in addition to using higher temperatures much higher pressures are also used. Pressures as high as 1000 psi are reported in the literature, but not simultaneously with 1000 ° C. Thus a set of design objectives of 1000 ° C and 1000 psi seems reasonable and practical.

2.2 Reactor System Design

A preliminary design outlay of this complete reactor system reveals that this system must consist of a differential micro-reactor, a gas collection system, a gas-analyzing system, a reactant-gas purifying system and a gas flow control scheme. A γ-ray detection unit is also needed to monitor the amount of potassium in K_2CO_3-loaded carbon samples during gasification experiments.

Such a system was designed, constructed and tested. As more experiments were conducted some unpredicted problems (such as presence of air inside the reactor even after prolonged purging of the system and interference of metallurgical carbon from the reactor wall with hydrogenation rate measurement of graphite) were faced and a new evacuation system and a quartz lining for the reactor were added to this system to resolve these problems. At occasions some minor revisions were also implemented and what is presented in Figure 2.1 and

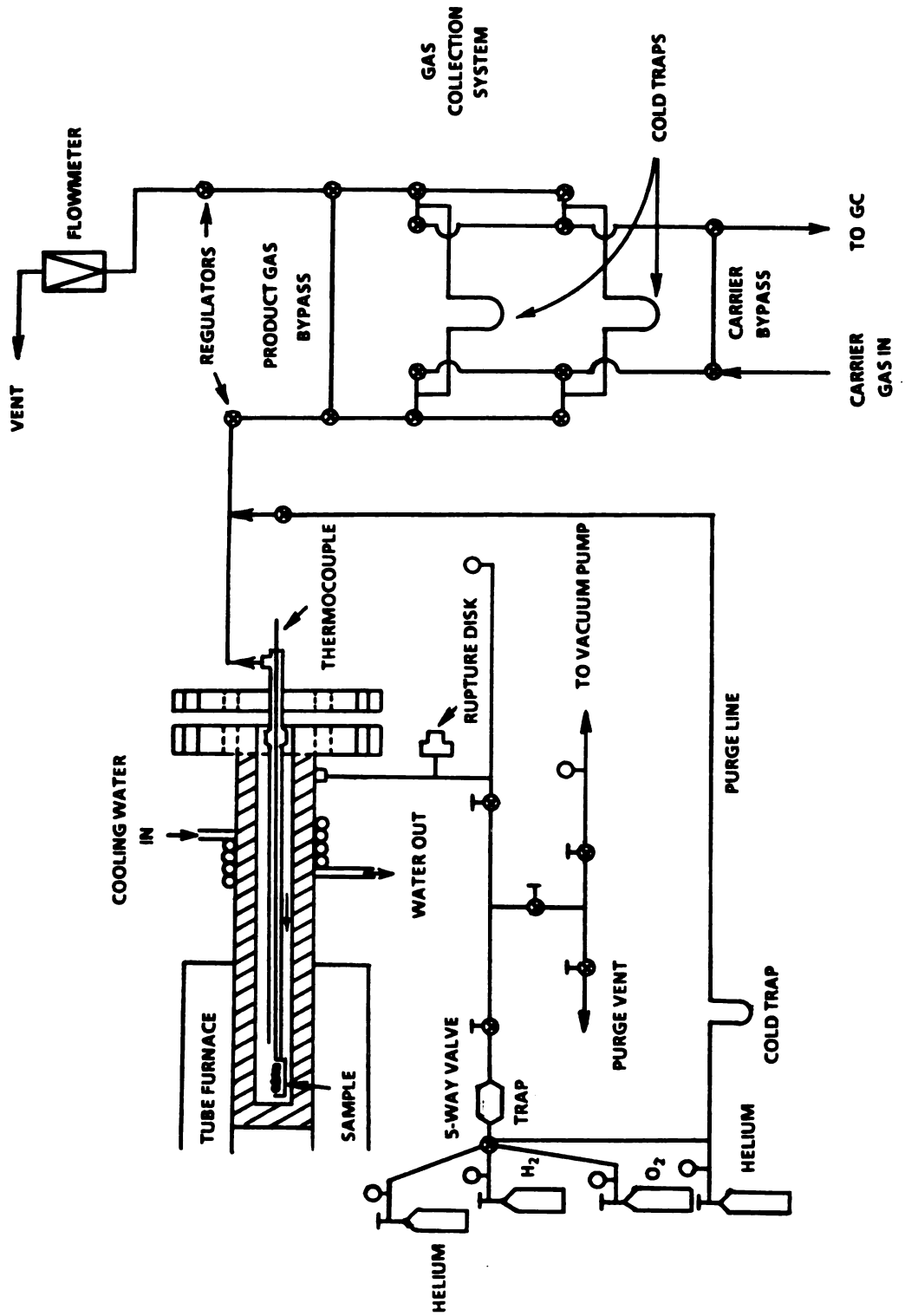

Figure 2.1 Schematic of the complete differential micro-reactor system.

is described hereafter is the final scheme of the system that was successfully used for gasification experiments.

2.2.1 Reactor Design

Due to the high operating pressure of 1000 psi the reactor to be designed is basically a high pressure cylindrical vessel closed at one end and a flange and a cover disk bolted together at the other end for enclosing the sample and isolating the reaction environment from the surroundings. The design and description of individual components of this reactor unit are discussed below.

2.2.1.1 Heating System

A heating system is needed to heat a sample under study inside the reactor to a desired temperature up to 1000 ° C. This could be achieved by either internal or external heating: internal heating being inserting some heating elements inside the reactor and heating the sample directly. Internal heating has three main advantages:

i) Much faster heating capability than the external heating can be obtained. The main mode of heat transfer from the heated surfaces to the sample inside the reactor is by radiation at the high temperatures of interest, and the sample can be heated fast if the hot surface of heating elements is close to the sample and faces the sample directly. In external heating the reactor wall has to be heated first and only then can the sample be heated by radiation from the reactor wall. This may take considerably longer times specially if the reactor wall material has low thermal conductivity and is thick.

ii) The heating elements inside the reactor can be insulated from the reactor wall and thus the reactor wall can be kept at much lower temperatures than the sample temperature inside the reactor. This translates into much higher

strength of the reactor wall material, and that in turn results in requiring a thinner reactor wall and lower construction costs.

iii) The heat loss from heating elements for internal heating are much less due to a smaller size and insulation from the reactor wall, so that heating is localized only around the sample. The smaller size of the heating elements and their better heating efficiency reduces construction and operating costs.

However, contamination is a big disadvantage to using internal heating. Both the heating elements and insulating materials (refractory bricks) contaminate the gaseous reactant stream and introduce complications and uncertainity into interpretation of the experimental results. This is highly undesirable, and therefore it was decided to concentrate on designing and evaluating the external heating option. For this purpose a Lindberg single-zone tube furnace model 54232 is chosen. This model has a 12"-long heating zone and is suited for heating tubes with 2" OD. This model is chosen for the reasons that will be discussed in Reactor Wall Thickness section. This implied that the reactor wall material has to be an alloy that is suitable for operation at 1000 ° C and 1000 psi pressure.

2.2.1.2 Material of Construction

The problem of selecting a suitable metal alloy for construction of the reactor is complicated by the so called "Hydrogen Environment Embrittlement" phenomenon (HEE) which is induced by hydrogen gas. This phenomenon has been observed over a wide range of hydrogen pressure, 10^{-8} Torr to 10000 psi. The exact mechanism of this process is not fully understood, but it has been well agreed upon that dissociative chemisorption of hydrogen molecule and absorption are necessary steps. The necessity of diffusion of the hydrogen atom into the alloy lattice has provoked marked disagreement [61]. Subsequent crack

initiation, internally or at the surface, and crack growth degrades one or more properties such as ductility of the alloy [62].

The high-strength structural alloys such as steels and nickel-base alloys are particularly susceptible to HEE [61]. Super strength alloys such as stainless steels 316, 304L, A-286 and some other alloys such as 19-9DL, N-155, IN 800 and aluminum, magnesium and copper alloys have excellent resistance to HEE but all lack structural strength that is needed at 1000 ° C [61,63,64]. Generally these alloys are usable only at temperatures below 800 ° C. Pure titanium is also a very good metal but is extremely expensive. The choice is then limited to some cobalt alloys such as Haynes-25 (L-605) that have acceptable resistance to HEE and have good structural strength at 1000 ° C. Haynes-25 alloy is thus selected as the material of construction for the micro-reactor. This alloy can also handle the oxidizing environment of air at 1000 ° C.

2.2.1.3 Reactor Wall Thickness

The differential micro-reactor to be designed here can be classified as a *thick-walled cylinder.* Traditionally, two widely accepted formulae are used to calculate the desired thickness of this vessel wall, Lamé's formula and Barlow's formula, which is only applicable to cylinders subject to internal pressures [65]. Barlow's formula embodies more assumptions on the side of safety than the Lamé's formula and thus is used as the design equation. This formula is

$$\varsigma = \frac{pD_o}{2\sigma_\theta} \tag{2-1}$$

where σ_θ is the circumferential or tangential stress, p is the internal pressure of the reactor, D_o is the outside diameter of the reactor and ς is the thickness of the reactor wall.

The rupture stress in 10000 hours at 1000 ° C is 2000 psi and is used as the value for σ_θ in the above equation [64]. Internal pressure p is set at 1100 psi to include a safety factor of 10% into the calculation. Equation 2-1 clearly shows that the wall thickness ς is directly proportional to the outside diameter of the reactor D_o and therefore smaller diameters are more favorable because the reactor wall material would cost less. However, the axial hole inside the reactor has to be big enough to provide sufficient space for convenient insertion and removal of samples inside the reactor and thus bigger reactor diameters are favored in this respect. Hence, a compromise has to be made for an optimal diameter size. It was then decided to try an outside diameter size of 2" as a first guess for the optimal size; a wall thickness of 0.55" was obtained from Equation 2-1. This leaves a cylindrical space with 0.9" diameter for housing the sample inside the reactor, which seems to be a reasonable and practical space for a sample. The actual size of the drilled hole is 7/8".

The required thickness of the closed end of the reactor vessel is calculated from an equation for circular flat plates [66]

$$\varsigma_h = \frac{D_i}{4}\sqrt{\frac{3p}{\sigma_{max}}} \qquad (2\text{-}2)$$

where ς_h is the head thickness, D_i is the inside diameter (7/8") and σ_{max} is the maximum allowable stress which for this case is equal to 2000 psi (rupture stress of Haynes-25 alloy at 1000 ° C in 10000 hours [64]). Substitution of these values into Equation 2-2 yields a thickness of 0.28". The actual thickness of the

fabricated head is 1" and thus the highest stress, which is at the edge is only 160 psi.

2.2.1.4 Flange Design

For the purposes of containing the high pressure reaction environment and convenient insertion and removing of samples from the open end of the reactor, three options are available; a flange, a screw cap and a clamp-on hinged cover disk. The last two options are not reliable due to leaks and inconvenience in handling and proper positioning of samples. Different types of flanges such as forged integral, loose or fusion lap-welded hubbed and ring flanges, *etc.*, can safely be designed and operated [67]. A plain fusion welded ring flange is chosen because of its simplicity of design and lower costs. This flange is made of Haynes-25 alloy so that it can be easily welded to the Haynes-25 reactor cylinder.

The surface contact between the flange ring face and the cover disk is not gas-tight enough to contain the high pressure reactant gas(es) and some gasket is thus required for this purpose. The type of gasket needs to be known *a priori* so that the required sealing stress can be included in flange stress analysis and thickness calculations. Metal gaskets generally require very large sealing stresses, much higher than the hydrostatic pressure in the present case, and furthermore are not reusable. O-ring gaskets, when mounted properly, are sufficient for handling 1000 psi design pressure. A 1¼" ID and 3/16" thick Viton O-ring is used with the mounting grooves on the cover disc. The sealing stress for this O-ring is 100 lb_f per inch of the O-ring [68]. The stress on the O-ring should be uniformly distributed for an optimum seal and thus larger number of bolts are favorable. Four to six bolts, with nuts and locker washers, are reasonable for a 3¼"-diameter bolt-circle. This bolt-circle diameter is the smallest diameter for

which the bolts and nuts can easily be put together without interference from the reactor wall and the flange welded laps.

The detailed calculations for the flange ring thickness are presented in the Flange Design section of Appendix A. The O-ring is assumed to be the only place of contact between the flange ring face and the cover disc and the analysis and design formulas [69] presented in Appendix A are true only for this particular case. The flange ring thickness is calculated to be 0.256" and for the sake of safety a plain ring flange ½" thickness was constructed. A 1"-thick stainless steel-316 cover disc was used because it is much cheaper than Haynes-25 alloy and has sufficient strength at room temperature. The calculated thickness is 0.611". The total deflection of the flange ring and the cover disc under the applied stresses (internal hydrostatic pressure plus the sealing stress of the bolts and the weight of the reactor) is 0.0011" at the bolt-circle. This value is too small to allow the flange ring and the cover disc to contact each other under stress bending and, therefore, the assumption of no contact other than at the site of the O-ring is not violated and the design analysis is valid.

2.2.1.5 Cooling System & Thermal Stresses

At the flanged end of the reactor vessel there are two NPT fittings for gas inlet/outlet and insertion of thermocouples that are leak proof at room temperature. The temperature rise from room temperature at this end of the reactor vessel, caused by heat transfer from the heated zone of the vessel during experiments, may cause these fittings to leak and therefore it is essential to keep the temperature at the flanged end at room temperature. Convective air-cooling requires a fairly long reactor. An existing 44" long Haynes-25 reactor at Department of Chemical Engineering at University of Florida at Gainesville provides enough length to air-cool the reactor to room temperature. Thus it was

decided to study the possibility of cutting down the reactor length to 22" by water-cooling the flanged end to room temperature without producing severe thermal stresses in the reactor wall. For this purpose a cooling system was devised which consisted of a rotary water pump, a ten gallon glass jar, a three way valve for draining the glass jar, a cooling coil around the reactor vessel near the flange, and some ¼" ID copper and Tygon plastic tubing.

2.2.1.5.1 Thermal Stresses

To calculate the thermal stresses, the length over which the reactor wall has to be cooled from the furnace temperature to room temperature has to be set first and only then can thermal stresses be calculated. However, in setting this cooling length some factors have to be taken into consideration. The cooling system cannot be mounted on the reactor vessel very close to the heated zone, because severe and damaging thermal stresses may develop inside the reactor wall. On the other hand, mounting the cooling coils on a long reactor vessel far away from the heated zone calls for a long and very expensive reactor, which is also inconvenient for insertion and removal of samples. Thus an optimum cooling length has to be found which will make the reactor short enough and at the same time will avoid development of severe thermal stresses.

Preliminary estimations established that at the flanged-end 2" is needed for mounting a 1/8" Swagelok tube fitting for gas inlet, mounting and supporting the reactor and welding the flange, and an additional 2½" for mounting cooling coils (6 to 8 laps). At the closed end 8½" is needed to be inserted inside the furnace for placing samples under study in the middle of the 12" heating zone of the furnace. That leaves 9" in between the heated zone and the cooling coils for gradual cooling of the reactor wall from furnace temperature to room temperature (Figure 2.2).

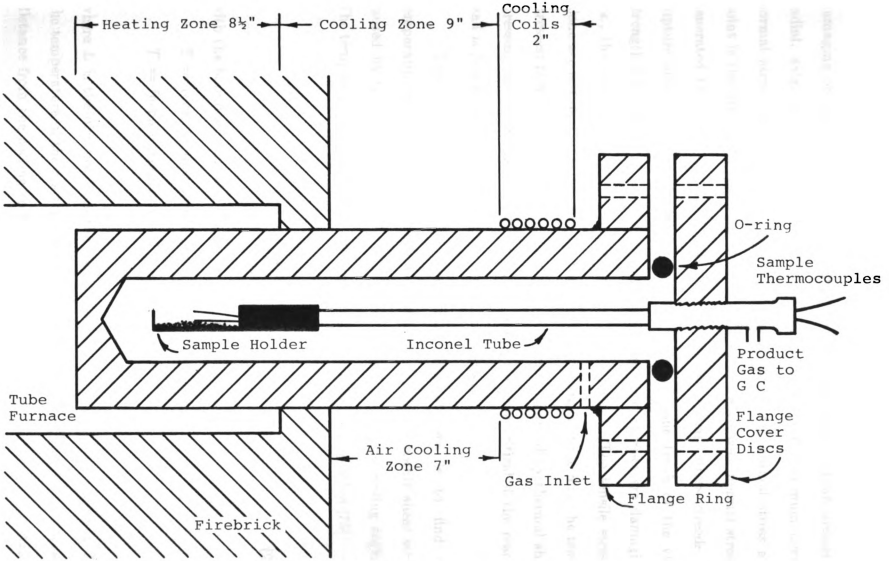

Figure 2.2 Differential fixed-bed micro-reactor and its temperature zones.

The criteria for determining whether or not the thermal stresses are damaging or not is to calculate all tensile stresses and thermal shear stresses in radial, axial and angular directions and then evaluate the maximum overall normal stress by Mohr's circle [72]. The maximum overall normal stress at a point is the highest combination of coupling tensile stresses with normal stresses generated by shear stresses. If this maximum overall normal stress exceeds the rupture stress in 10000 h (which at 1000 °C is only one tenth of the yield strength for Haynes 25 alloy) of the material, the shear stresses are damaging; *i.e.*, the reactor wall will fail much sooner than expected. The tensile stresses alone are not damaging because the wall is already designed to handle the tensile stresses; however, when coupled with normal stresses produced by thermal shear stresses, the result may be damaging. This may become critical if the reactor wall is just thick enough to handle only tensile stresses.

The underlying idea for evaluating shear stresses is to find the temperature profile of the cooling zone and then to estimate elastic shear strain caused by temperature gradients and thermal expansion in the cooling region. The temperature profile is calculated by solving the following equation [75]

$$\frac{d}{dz}(\kappa\frac{dT}{dz}) = 0 \tag{2-3}$$

with the boundary conditions

T = room temperature $T_m = 77\,^{\circ}\mathrm{F}$ at $z = 0$

T = furnace temperature T_f at $z = L$

where L is the distance from the cooling coils to the furnace heating zone, T is the temperature of the reactor wall, T_f is the furnace temperature, z is the axial distance from the cooling coils and κ is the thermal conductivity of the reactor

wall material. The important assumption made here is to ignore convective heat transfer to ambient air or gases inside the reactor; *i.e.*, there is no radial temperature gradient and heat is transferred only in the axial direction. This temperature profile yields the maximum heat duty of the cooling coils, but underestimates the thermal shear stresses in the hot regions of the wall because the reactor wall is cooled faster than what is predicted from this equation. The details of computing this temperature profile are presented in the Thermal Stresses section in Appendix A (Equations A-3 to A-9).

The next step is to relate elastic shear strain dr/dz to the above temperature profile. This is done using the following equation

$$\frac{dr}{dz} = \frac{dr}{dT} \cdot \frac{dT}{dz} \tag{2-4}$$

where r is the radial distance of a point from the axis of the cylindrical reactor vessel. The derivative dr/dT can be estimated from thermal expansion coefficient α of the reactor wall and the details can be found in Thermal Stresses section in Appendix A (Equations A-10 to A-14).

Once the elastic shear strain is known, the corresponding radial shear stress τ_{zr} can be calculated [66]

$$\tau_{zr} = G\frac{dr}{dz} \tag{2-5}$$

where G is the shear modulus of elasticity of the reactor wall. The final estimation from Appendix A for τ_{zr} is

$$\tau_{zr} = \frac{r\alpha G}{3} \frac{3561}{\sqrt{1+8.35\frac{z}{L}}} \tag{2-6}$$

It can be seen clearly that τ_{zr} is a function of both axial position z and radial position r for a given cooling length L. It can also be seen that the points of maximum shear stress are the points at $z=0$ and $r=r_o$; *i.e.*, the points next to the cooling coils on the outside of the reactor. At these points G is also a maximum. However, this does not mean that these points are the weakest points of the reactor wall, because the yield and the rupture strengths of the reactor wall at these points are also at a maximum.

Thermal shear stresses in axial and angular directions (τ_z and τ_θ, respectively) are zero because of assumed uniform and symmetric heating of the reactor wall.

Normal tensile stresses in radial, angular and axial directions (σ_r, σ_θ and σ_z, respectively) due to internal pressure p at a point (r,θ,z) of the reactor wall can be calculated from the following equations [66]

$$\sigma_r = -p \frac{r_i^2}{r_o^2-r_i^2}\left(\frac{r_o^2}{r^2}-1\right) \tag{2-7}$$

$$\sigma_\theta = p \frac{r_i^2}{r_o^2-r_i^2}\left(\frac{r_o^2}{r^2}+1\right) \tag{2-8}$$

$$\sigma_z = p \frac{r_i^2}{r_o^2-r_i^2} \tag{2-9}$$

It can be seen that these stresses are not functions of angular or axial positions. That is what is expected because pressure is the same for all z and the normal stress on the inner cylindrical wall of the reactor is independent of the angle θ. Radial stress σ_r is negative because it is compressive, angular and axial stresses are positive because they are tensile.

Therefore, the maximum overall normal stress σ_{max} at a point, which is calculated by Mohr's circle from the shear and tensile stresses at that point, is a function of the radial as well as the axial position. As discussed earlier, at the hot end of the reactor vessel the shear stresses are lower in magnitude than those at the flanged-end, but the strength of the wall material is also lower. Thus, at each point of the reactor wall σ_{max} should be calculated and compared with rupture or yield strength of the wall material at that point. The results of calculations for four different sets of points of the reactor wall are presented in Table 2.1. These four sets of points are two sets at the hot end, one on the outside of the reactor wall (r_o, L) and one on the inside (r_i, L), and the other two at the cooling coil, one on the outside of the reactor wall $(r_o, 0)$ and one on the inside $(r_i, 0)$. Again an operating internal pressure of 1100 psi was assumed for calculating normal tensile stresses.

Table 2.1 Maximum overall normal stresses in the reactor wall

point	σ_z (psi)	σ_θ (Kpsi)	σ_r (Kpsi)	τ_z (psi)	τ_θ (psi)	τ_{zr} (Kpsi)	dT/dz (°F/in)	G (Mpsi)	α (μ in/in-°F)	σ_{max} (Kpsi)
$(r_o, 0)$	260	0.52	0	0	0	11.8	395	13.1	6.83	11.9
$(r_i, 0)$	260	1.62	-1.1	0	0	5.16	395	13.1	6.83	4.79
(r_o, L)	260	0.52	0	0	0	1.56	129	3.85	9.41	1.69
(r_i, L)	260	1.62	-1.1	0	0	0.68	129	3.85	9.41	1.62

From Table 2.1 it can be seen that even though the maximum shear stresses and the maximum overall normal stresses are at the location of the cooling coils ($z=0$), the weakest spots of the reactor wall are at the inlet of the heated zone ($z=L$), where the overall normal stresses are 15% lower than the rupture stress $\sigma_{rupture}$ in 10000 h. The assumption that is made for calculating G at 1000 °C is that the Poisson's ratio μ does not change with temperature. This ratio is assumed to be equal to 0.3, as in flange design, and G is calculated from the following formula [72]

$$G = \frac{E}{2(1+\mu)} \tag{2-10}$$

where E is the Young modulus of elasticity. The value of μ is 0.25 for a perfectly isotropic elastic material, but for most metals it is closer to 0.33 [73]. Thus, even if Haynes-25 is assumed to be a perfect isotropic elastic material at high temperature, the value of G will be only 4% higher than G for μ equal to 0.3, and the overall normal stresses will still be less than $\sigma_{rupture}$.

Close examination of values of σ_θ and τ_{zr} in Table 2.1 reveals that at the inner wall of the reactor, the major contribution to $\sigma_{\max}$ is from tensile stresses, and thus the assumptions that were made for calculating τ_{zr} do not play an important role in evaluating the significance of shear stresses. At the outer wall, on the other hand, the major contribution comes from the shear stresses. The assumption of no radial heat transfer is justified by the fact that 2" of the reactor wall at the furnace inlet is insulated by fire bricks from outside and thus heat transfer to the surroundings by radiation or convection is minimal. Heat transfer by convection to gas(es) inside the reactor is also small because of high residence time of the gas(es) and the quartz lining inside the reactor. This has

been verified by recent experiments in which the temperature of a sample was measured under vacuum and in the presence of 500 psi hydrogen gas, the difference was found to be only about 10 ° C. The assumption of regarding the reactor wall as a solid cylinder, explained in Appendix A, is also reasonable because of the high thickness of the reactor wall.

Hence, the overdesign of the reactor wall, as calculated from Barlow's formula (Equation 2-1), is large enough to tolerate the additional normal stresses induced by thermal shear stresses; and a length of 9" for cooling zone is economical and safe (Figure 2.2).

2.2.1.5.2 Cooling Coils

The required total surface area A for heat transfer (and length of the cooling coils L_c) depends on the magnitude of the overall heat transfer coefficient h_o, the temperature driving force ΔT and the heat load Q

$$A = \frac{Q}{h_o \Delta T} \tag{2-11}$$

The magnitudes of both heat transfer coefficient h_o and temperature driving force ΔT depend on the flow regime inside the cooling coils [74]. Thus it is necessary to determine whether the flow regime is laminar or turbulent. This is done by a simple energy balance which determines the mass flux $\dot{m}$ of the cooling water; the Reynolds number R_e is then calculated from that:

$$R_e = \frac{\dot{m} d}{\mu_v} \tag{2-12}$$

The temperature driving force ΔT is calculated from the temperature rise of the cooling water and the temperature of the reactor wall. For this purpose the inlet temperature T_i of the cooling water was assumed to be at 70 °F with a temperature rise of 10 °F. The reactor wall temperature T was assumed to be at a constant temperature of 85 °F. The details are presented in the Cooling Coils section of Appendix A.

The important assumptions made are that *i*) the overall heat transfer coefficient h_o is equal to the heat transfer coefficient across the liquid film in the cooling coils, because the thermal conductivities of the copper tubes and the reactor wall are relatively high and thus impose negligible resistance to heat transfer, and *ii*) the temperature of cooling coils is uniform throughout, even though heat is transferred from reactor wall to cooling coils only at the side of cooling coils which is soldered to the reactor wall (which is less than half of the cooling coil surface area A). The very high thermal conductivity of the copper and the thick walls of copper cooling coils (3/64") justify these assumptions.

The results in Appendix A show that the flow regime inside cooling coils is turbulent and 2-3 laps of copper tubing around the reactor are required for keeping the temperature of the flanged end at room temperature. Six laps of copper tubing were used.

2.2.1.6 Reactor Quartz Lining

The reactor wall goes through the thermal cycles of heating and cooling from room temperature to reaction temperature or degassing temperature and back. During these thermal cycles some metallurgical carbon from the reactor wall alloy is deposited out on the reactor wall and reacts with hydrogen gas at high temperature to yield methane. The rate of this reaction, although very small, interferes with reaction rate measurements of graphite, as will be

discussed in Section 5.2. To reduce the reaction of hydrogen with this metallurgical carbon, a quartz lining was inserted inside the reactor. This quartz lining is a 22mm OD $\times$ 21" quartz tube closed at one end and 2" of one side at the other end cut off to accommodate the hydrogen inlet stream. This quartz tube fits snugly into the reactor; for hydrogen to react with the metallurgical carbon it has to diffuse through the very narrow space between the reactor wall and the tube to the hot end, and then product methane has to diffuse in the reverse direction to enter the hydrogen flow stream. The tube reduces the interference from the metallurgical carbon substantially.

2.3 γ-Ray Detection System

In the experiments involving potassium carbonate as a catalyst, determination of the amount of potassium in a sample at each point in time can provide a great deal of information on the catalysis process, as will be discussed in Chapter 5. One way of determining the amount (or relative amounts) of potassium is by *in situ* neutron activation analysis (NAA).

NAA involves bombarding nuclei of potassium atoms in a sample with a high flux of neutrons ($\sim 10^{12}$-10^{13} neutrons/cm^2-s) inside a nuclear reactor, and then monitoring the energy and intensity of radiation emitted by unstable isotope(s) formed. The energy of emitted radiation serves as a fingerprint of unstable isotope(s) formed, and the intensity serves as a measure of the quantity.

The high flux of neutrons interacts with the nuclei of potassium ^{41}K atoms, which constitute about 6.9% of the potassium found in nature, and yield ^{42}K nuclei. ^{42}K is an unstable radioactive isotope which decays by a β-decay mode with a half life $t_{½}$ of 12.36 h [76]. The products of this decay are β-

radiation (electrons) and ^{42}Ca nuclei, of which 81% are in ground state, 18% are in the lowest excited state (1.525 MeV, $t_{1/2} = 0.82 \times 10^{-12}$ seconds) and 1% are in excited states of higher energies with $t_{1/2}$'s of less than 10^{-9} seconds. The excited states of ^{42}Ca all decay to ground state or lower excited states by releasing their excitation energies as γ-rays (photons).

The Mech-Tronics Nuclear γ-ray detection system used consists of a Harshaw 3½"×3½" NaI(Tl) scintillation crystal with a photomultiplier, a model 450 preamplifier probe assembly, a model 500 RC pulse amplifier, a model 251 high-voltage power supply, a model 602 single channel analyzer, a model 1304 printer/interface, a model 706 scaler and a model 756 timer.

2.3.1 Theoretical Derivations

2.3.1.1 Mass-Radiation Relation

The radioactive decay of ^{42}K is a statistical process and the intensity of decay radiation (β-ray or γ-ray) at a macroscopic level is thus directly proportional to mass. Therefore, for a given sample a knowledge of weight fraction of total potassium as ^{42}K and the radiation rate or nuclear disintegration rate at each point in time indicates how much potassium is present in that sample at that particular time. The number of atoms $\bar{N}^{42}$ of radioactive potassium ^{42}K *in the sample* at any time is related to the nuclear disintegration rate $\bar{R}$:

$$\bar{R} = \epsilon \bar{N}^{42} \tag{2-13}$$

where ϵ is a proportionality constant equal to $ln\,2/t_{1/2}$. The number of atoms N_o^{42} of radioactive potassium ^{42}K at the end of neutron bombarding of N_o^{41}

atoms of ^{41}K for a period of t_a is calculated from the following equation

$$N_o^{42} = N_o^{41} \frac{\eta\Phi}{\epsilon}(1-e^{-\epsilon t_a}) \tag{2-14}$$

where Φ is neutron flux (10^{12}-10^{13} neutrons/cm^2-s) and η is the cross section of ^{41}K atoms for neutron absorption, which is equal to 1.5×10^{-24} cm^2. At time t after the end of neutron activation some portion of N_o^{42} decays away and what is left, N^{42} (not necessarily all in the sample), is calculated from the following equation

$$N^{42} = N_o^{42}\, e^{-\epsilon t} \tag{2-15}$$

If no potassium is lost from the sample, N^{42} and $\bar{N}^{42}$ are numerically equal. However, if some potassium is lost , say by vaporization from the sample during this time, the radiation rate will be lower and the fraction f of potassium lost from the sample is calculated from the following equation

$$f = \frac{(N^{42}-\bar{N}^{42})e^{\epsilon t}}{N_o^{42}} \tag{2-16}$$

The total mass M of potassium in the sample at any time is then related to initial total mass M_o of potassium according to the following formula

$$M = (1-f)M_o \tag{2-17}$$

Substitution of appropriate values from Equations 2-13 through 2-16 into the above equation yields

$$M = M_o \frac{\overline{R}}{N_o^{41} \eta \Phi} \frac{e^{\epsilon t}}{(1-e^{-\epsilon t_a})} \tag{2-18}$$

where N_o^{41} is calculated from M_o using the Avogadro's number N_{avo}, potassium molecular weight W_K, and the fraction χ of potassium as ^{41}K;

$$N_o^{41} = \frac{\chi M_o N_{avo}}{W_K} \tag{2-19}$$

2.3.1.2 Radiation Measurement

2.3.1.2.1 Problems

The only parameters that need to be measured during an experiment to calculate the amount of total potassium M in the sample at any time from Equation 2-18 are t_a,t and $\overline{R}$. The measurements of t_a and t are straightforward. The measurement of $\overline{R}$, however, presents a great deal of difficulty because there is no way of counting number of nuclear disintegrations directly. There are detection systems which detect a fraction of radiations by counting the number of electrical pulses generated proportionally by β-rays or γ-rays. Effective use of a detection system requires a knowledge of efficiency of its detector; that is, how many electrical pulses are generated and counted for each β-ray or γ-ray that enters the detector. This efficiency depends on the nature and energy of the radiation as well as the type of the detector.

The problem of measuring the $\overline{R}$ is further complicated by the fact that there are shielding materials between radioactive sample and the detector. The shielding materials interact with radiation via several modes and result in absorption of some or all of the radiation. If most of the radiation is absorbed by the shielding materials, there may not be enough radiation entering the detector to measure $\overline{R}$ reliably.

Thus the radiation rate as measured by the detection system $\underline{R}$ is substantially less than the actual nuclear disintegration rate $\overline{R}$ of the sample, due to absorption of radiation by shielding materials and inefficiency of the detector system to detect all the radiation reaching the detector. Therefore, the relationship between $\overline{R}$ and $\underline{R}$ should be established before Equation 2-18 can be used to calculate M.

2.3.1.2.2 β-Rays

As mentioned earlier, ^{42}K decays to ^{42}Ca with emission of β-rays and γ-rays, both with different but discrete energies. The β-rays have much lower penetrating ability than the γ- rays. The maximum energy that β-rays in ^{42}K can have is about 3.5 MeV, and the maximum range of penetration in Haynes-25 is about 0.075"[79]. This is much less than the Haynes-25 reactor wall thickness of 9/16". Therefore, no β-rays reach the detector outside the reactor, and detecting the β-rays as a means of measuring $\overline{R}$ is not possible.

2.3.1.2.3 γ-Rays

Of the unstable ^{42}K isotope formed by neutron bombardment, 18% decays to an excited ^{42}Ca nucleus, which subsequently decays to the ground state and releases its excitation energy of 1.525 MeV as a γ-ray. These γ-rays have a high penetrating ability even through metals, with a half value layer (the

thickness of shielding to reduce the intensity of the γ-ray emission by half) of 1.174 cm for lead. As the calculations given in the Radiation System section of Appendix A show, a 6 mg K_2CO_3 sample activated for 80 minutes emits enough radiation to allow reliable counting rates (10 times the background). Therefore, detection and counting the 1.525 MeV γ-ray is a practical means for $\bar{R}$ measurement.

2.3.1.2.4 Interaction and Absorption of γ-Rays

Any measurement of γ-ray emission, along with a knowledge of detector efficiency, can just determine the intensity of the radiation in the immediate neighborhood of the detector. To relate this measurement to radioactivity of ^{42}K in a sample and thus to total mass of potassium, it is necessary to estimate the interaction and subsequent absorption of the γ-ray by shielding material.

The extent of absorption generally depends on the energy of the γ-ray, the nature of the shielding material (atomic number Z and density ρ) and its thickness. If a γ-ray radiation of intensity I_o passes through a shielding material of thickness x, the radiation intensity is reduced to a value I which is calculated from the following equation [76,77]

$$I = I_o e^{-\Lambda x} \tag{2-20}$$

where Λ is the attenuation coefficient of the material. Its magnitude depends on the γ-ray energy and nature of the shielding material only; that is, it is independent of the thickness. Thus the extent of absorption of γ-rays by materials between a sample and the detector can be calculated from the thickness of the shields and their values of Λ.

2.3.1.2.5 Attenuation Coefficients

Computation of values of Λ requires a knowledge of mechanism(s) of interactions between γ-rays and atoms or molecules of shielding materials. These interactions can take place by eight different mechanisms [77], but for the γ-rays of interest practically only three mechanisms are responsible for the absorption [78]. These three mechanisms are the *photoelectric effect, Compton effect,* and *pair production.* Hence, Λ can be written as a sum of three terms, each of which is the contribution from one of these three mechanisms:

$$\Lambda = \nu + \xi + K \tag{2-21}$$

The variables ν, ξ and K are coefficients of photoelectric effect, Compton scattering, and pair production, respectively.

2.3.1.2.5.1 Photoelectric Effect

Photoelectric effect is the inelastic collision of a γ-ray with an orbital electron whereby all of the energy of the γ-ray is transferred to the electron (usually an inner K shell). The result is ejection of the electron from the atom and production of an ion pair. The photoelectric coefficient ν is estimated from the following relation [77,79]

$$\nu = 6.06 \times 10^{-33}\, \rho N_{avo} \frac{Z^{4.55}}{A_t} \tag{2-22}$$

where A_t is the atomic weight of the shielding material and ρ is the density of the shielding material. The photoelectric effect is more important at lower energies.

2.3.1.2.5.2 Compton Effect

Compton effect or Compton scattering involves a collision between a γ-ray and an electron in which a part of the energy of the γ-ray (as opposed to all of the energy in photoelectric effect) is imparted to the electron. The γ-ray energies from the collision in a new direction and with reduced energy. The Compton scattering coefficient ξ is estimated from Equation 2-23 [79]

$$\xi = \rho N_{avo} \eta_c \frac{Z}{A_t} \tag{2-23}$$

where η_c is the Compton cross section per electron. The value of η_c depends on the energy of the γ-ray; for the 1.525 MeV γ-ray of interest it is roughly 1.6×10^{-25} cm^2 [79]. Compton scattering is especially important for γ-rays of medium energy (0.5 to 1.0 MeV).

2.3.1.2.5.3 Pair Production

In pair production, a γ-ray passing close to a nucleus (*i.e.*, in the vicinity of a strong electromagnetic field) suddenly disappears and an electron (negatron) and a positron are created in its place. The rest-mass energy of these two particles is 1.02 MeV and therefore only γ-rays with energies in excess of 1.02 MeV can go through this process, with the difference in energy appearing as the kinetic energies of the electron and the positron. The coefficient K is computed from the following relationship [77]

$$K = 1.19 \times 10^{-29} N_{avo} Z^2 (E_\gamma - 1.02) \tag{2-24}$$

The above three equations are used to calculate the value of Λ for Haynes-25 alloy. The contributions from the three mechanisms to attenuation coefficients of individual components (major components) in Haynes-25 alloy are presented in Table 2.2. The attenuation coefficient Λ of Haynes-25 alloy is simply the volume-weighted sum of the attenuation coefficients of the individual components:

$$\Lambda = \sum_{i=1}^{n} v_i \lambda_i \tag{2-25}$$

where n is the number of components in the alloy, v_i is the volume fraction of component i, and λ_i is the attenuation coefficient of component i.

Table 2.2 Attenuation coefficients of lead and Haynes-25 components

element	ρ g/cm^3	wt %	v_i	Z	A_t cm^{-1}	$\nu\times10^3$ cm^{-1}	ξ cm^{-1}	$K\times10^3$ cm^{-1}	λ
Co	8.9	53.55	0.555	27	59	1.79	0.392	2.70	0.397
Cr	7.18	20.11	0.257	24	52	0.960	0.319	2.13	0.322
W	19.3	15.54	0.0741	74	184	122.5	0.748	20.3	0.891
Ni	8.902	10.8	0.114	28	59	2.116	0.407	2.90	0.412
Pb	11.35	100	1.00	82	207	102.1	0.433	24.3	0.559

The attenuation coefficients for other shielding materials used in this system are readily available in the literature [79] and are tabulated in Table 2.3 along with the estimated attenuation coefficient for Haynes-25 alloy from Equation 2-25.

Table 2.3 Attenuation coefficient Λ for various shielding media

Material	Attenuation coefficient Λ (cm^2)
Air	0.0000513
Firebrick	0.025
Iron	0.380
Lead	0.578
Haynes-25	0.416

2.3.1.2.6 Absorption

For a sample of radioactivity I_0, the fraction of radiation f_I passing through the shielding materials in Figure 2.3 can be calculated from

$$I = I_0 e^{(-\sum_{i=0}^{n} \Lambda_i x_i)} \tag{2-26}$$

where x_i is the thickness of the ith shielding layer and Λ_i is the attenuation coefficient of that layer.

Substitution of appropriate values for x_i from Figure 2.3 and Λ_i from Table 2.3 yields

$$f_I = \frac{I}{I_0} = 0.334 \tag{2-27}$$

The details of the calculations are presented in Appendix A in the section on γ-ray calculations. Therefore, only 33.4% of γ-rays emitted by ^{42}K in the sample pass through the shields and reach the detector.

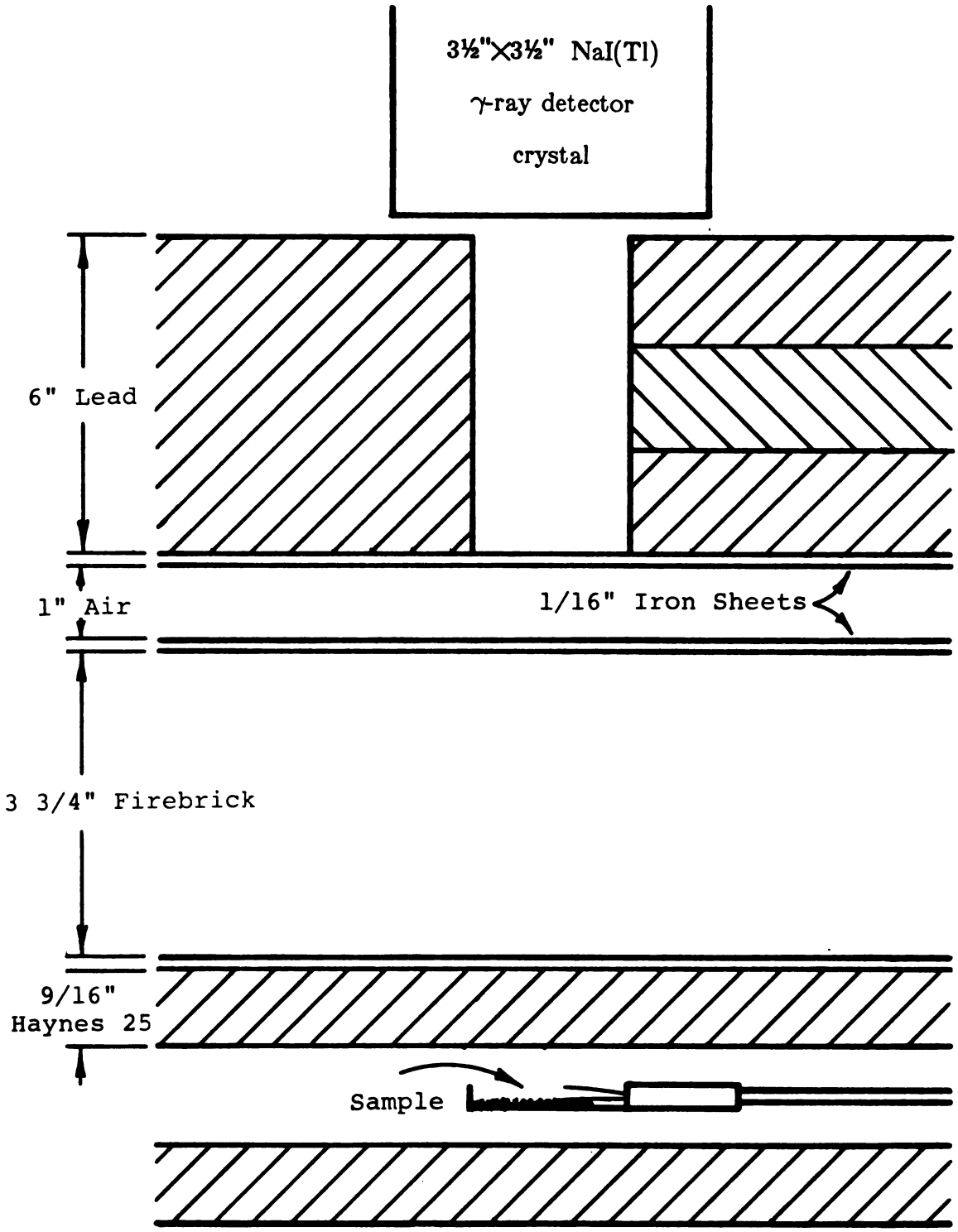

Figure 2.3 γ-Ray detection configuration

2.3.1.2.7 Geometric Factor

The γ-rays from a sample are given off in all directions and hence only a fraction f_d of the γ-rays are detected by the NaI(Tl) detector. This fraction f_d is equal to the fraction of the surface area of a sphere with radius L_d equal to the distance of the detector from the sample, which is covered by the surface of the detector. This is given by

$$f_d = \frac{\left(\frac{D_d}{2}\right)^2}{4L_d^2} \tag{2-28}$$

where D_d is the diameter of the detector crystal (3½"). This fraction turns out to be 0.0051.

2.3.1.2.8 Sample Activation

The efficiency ψ of the NaI(Tl) detector for γ-rays is 4-5% [80] and the measured background counting rate is 5-6 counts per second (c/s). Thus to obtain a counting rate of 60 cps (*i.e.*, ten times the background) the radioactivity I_0 of the sample needed is

$$I_0 = \frac{60\ cps}{\psi f_d f_I} \tag{2-29}$$

Note that I_0 and $\overline{R}$ are related but are not equal; I_0 is the rate at which γ-rays are emitted from a sample, whereas $\overline{R}$ is the rate of nuclear disintegrations (of which only 18% emit γ-rays). The required value of $\overline{R}$ from the Sample Activity section of Appendix A is 3.91×10^6 disintegrations per second (dps); or a

γ-ray intensity I_o of 7.04×10^5.

Now assuming that an experiment takes 2 hours and that during the experiment 80% of the potassium is lost, say via vaporization, then the nuclear disintegration rate needed at the beginning of the experiment $\overline{R}\,|_{t=0}$ is 590 μCi as calculated from the following equation

$$\overline{R}\,|_{t=0} = \frac{3.91 \times 10^6\ dps}{(1-0.8)}\ e^{\epsilon .2\ h} \tag{2-30}$$

The samples containing potassium are allowed to be activated to only 100 μCi because of restrictions imposed by Office of Radiation, Chemical and Biological Safety at Michigan State University.

The time t_a needed for activating a sample in the nuclear reactor to 100 μCi can now be calculated from Equations 2-13 and 2-14. For a typical 60 mg carbon-catalyst sample of 10 wt%-K_2CO_3 the amount of ^{41}K is 0.234 mg, or 3.44×10^{18} atoms. Disintegration rate $\overline{R}$ of 100 μCi corresponds to 2.38×10^{11} atoms of ^{42}K (Equation 2-13). Thus with a neutron flux of 10^{12} neutron/cm^2-s an activation period of 25.3 hours is required. For samples of this size, therefore, a neutron flux of 10^{13} is used so that the activation time is reduced to 1.41 hours or 84 minutes (see Appendix A, Sample Activation).

To prevent detecting γ-rays from sources other than the sample itself (say vaporized potassium which condenses on cooler parts of reactor vessel) at least 6" of lead bricks are used to focus the detector. The γ-ray absorption of these lead shields is calculated from Equation 2-20 and Table 2.2, and is found to reduce the intensity of the γ-rays from other parts of the reactor vessel by a factor of 7400 (see Appendix A, γ-Ray Absorption).

2.3.2 Potassium Content Measurements

Therefore $\bar{R}$ can be calculated from R;

$$\bar{R} = \frac{1}{0.18\psi f_d f_I} R \tag{2-31}$$

and can be substituted into Equation 2-18 to obtain

$$\frac{M}{M_o} = \frac{e^{\epsilon t}}{0.18 N_o^{41} \eta \Phi \psi f_d f_I \, (1-e^{-\epsilon t_s})} R \tag{2-32}$$

Comparison of the terms in the denominator with Equations 2-13 and 2-14 indicates the denominator is just $R \mid_{t=0}$, and thus

$$\frac{M}{M_o} = \frac{R}{R \mid_{t=0}} e^{\epsilon t} \tag{2-32}$$

if f_d and ψ stay constant with time.

2.3.3 Biological Effects of γ-Rays

The biological effect of 100 μCi of γ-ray radiation is calculated using the Gamma constant Γ of ^{42}K [78] which is

Γ = 0.14 Roentgens per hour per curie at 1 meter

= 0.13 rad/h per curie at 1 meter.

This yields

$$I = 0.013 \text{ m rem/h at 1 meter}$$

$$= 130 \text{ m rem/h at 1 cm}$$

which is in the relatively safe range.

2.4 Gas Collection System

The devised gas collection system consists of three ¼"-OD stainless steel ∪-shape cold traps (labeled A, B and C) each of which is connected on either side to two miniature 2-way Brunswick Technetics solenoid valves (model A-2013).

2.4.1 Solenoid Valves & Electronics

The response time to close or open these valves is 5-25 ms. Of the two valves on one side of a cold trap, one is attached to the reactor effluent line and is called the "reactor" valve, and the other valve is attached to the helium carrier gas line of the gas chromatograph and is called the "GC" valve. The two "reactor" valves or the two "GC" valves of a cold trap can only be activated simultaneously, from a switch board of 12-pole 3-position rotary switches. The switch board houses two of these switches, one for the "reactor" valves and one for the "GC" valves. Each position of the three positions on the switches (called positions A, B and C) activates the valves of the corresponding trap. Thus these traps can be put in-line with the reactor effluent stream for gas collection, and the GC helium stream for gas analysis by activating the corresponding valves. A cold trap can be in-line with both the reactor effluent stream and the GC helium stream at the same time.

2.4.2 Cold Traps

The cold traps are inserted into liquid nitrogen to condense and collect product gases such as CH_4, CO and CO_2 in the reactor effluent stream. The cold-trap tubes should be long enough such that the tube fittings connected to the valves do not experience very cold temperatures, otherwise they might leak. Stainless steel is used instead of copper to reduce the temperature drops at the fittings when the traps are inserted into liquid nitrogen. The cold-trap tubes are 29" long, and when inserted into liquid nitrogen there is at least 3" distance between the liquid nitrogen level and the fittings. Depending on the level of liquid nitrogen 5.5"-11" of the cold trap is inserted in liquid nitrogen.

2.4.3 Silica Gels

The liquid nitrogen temperature alone is not enough for cooling and condensing the product gases fast enough so that they can be collected quantitatively, because of low surface area for heat transfer. To alleviate this problem, 1.4-1.7 g of 6-16 mesh silica gel manufactured by J. T. Baker Chemical company is added to each cold trap. This silica gel is highly porous and can absorb more than 30% moisture. The problem with this amount of silica gel is that the gas flow rate through a trap cannot be raised very high; *e.g.*, a flow rate of $\sim$ 400 ml/min blows some of the silica gel out of the cold traps and to the solenoid valves. Thus for experiments flow rates of $\sim$ 310 ml/min are used.

2.5 Gas Analyzing & Calibration System

The gas analyzing apparatus includes a series 5750 F&M (Hewlett Packard) research gas chromatograph (GC), a Sargent-Welch recorder model XKR with an electronic integrator, 99.999%-pure helium gas, a six-port calibration valve, and a calibration gas mixture.

2.5.1 Gas Chromatograph & Recorder

The GC is equipped with a thermal conductivity cell (TC cell) and two 60/80 Carbosieve S-II stainless steel columns, 5′ ×1/8″, installed in parallel. The TC cell is operated at room temperature at a current of 150 mA. The Carbosieve S-II column is suitable for analysis of permanent gases and light hydrocarbons, and the recommended temperature programming is: "hold 2 min at 35 ° C, then to 175 ° C at 20 ° C/min and hold," with a helium flow rate of 30 ml/min [81].

In proposed experiments, however, no hydrocarbon other than methane is expected to be in the reactor effluent gas and thus each gas analysis cycle is expected to be completed in 8 minutes. The difficulty with this temperature programming is that the CO peak and N_2-O_2 peak overlap and cannot be accurately quantified. Various trials shows that holding at 50-60 ° C instead of 35 ° C for 2 min and flow rates of 37-40 ml/min improves the resolution and decreases the cycle time to 7.5 minutes. The pressure of helium carrier gas is 30 psi.

The recorder chart speed and voltage/full-range ratio can be varied from 0.05 to 20 cm/min and 10 to 100 mV, respectively. The voltage span of the integrator is 1 to 1000 mV. Thus a wide range of peaks can be analyzed with this recorder accurately, provided the GC column is not flooded.

2.5.2 Calibration Setup

Two gas mixtures have been used for calibrating the GC signals: a Linde helium gas mixture of 4.8% CH_4, 4.9% CO and 4.9% CO_2, and an Airco gas mixture containing 5.20%, 5.33% and 5.26% by volume CH_4, CO and CO_2, respectively.

A 6-port "43Y6" series Whitey ball valve (two-position) is used for sampling and injecting the calibration gases into the GC. A 20"×1/8" and a 10.5"×1/8" 304-stainless steel tube are used for sampling 1.81 ml and 0.87 ml of the calibration gases, respectively. The sampling tube is swaged to two opposite ports on the hexagonal base of the calibration valve; two ports on one side of these ports are connected to the calibration gas line, while the other two ports are placed in-line with the helium carrier gas. This way, the sampling tube is either in-line with the calibration gas stream or the carrier gas. By switching between the two positions a predetermined volume of the calibration gas is injected into the GC carrier gas stream and analyzed.

2.6 Gas Purifying System

The 99.999%-pure helium and hydrogen gases used in experiments still contain some contaminating impurities such as oxygen and water vapor, and to further purify these gases a purifying system has been devised. Linde molecular sieve 3A (Alpha Products) with a nominal pore diameter of 3 Å, which adsorbs any molecules with an effective diameter less than 3 Å, are used as purifying agents. 500 ml Whitey sample cylinders are filled with 1/8" pellets of the molecular sieves and are inserted in line with helium carrier gas and hydrogen gas lines. Each cylinder is enough for purifying five 250 ft^3-cylinders of

hydrogen or helium.

The molecular sieves are regenerated by heating them to 270 ° C *in vacuo* with 1"×8′ flexible Samox-insulated electrical heating tapes for 45-60 minutes.

2.7 Evacuation System

When samples are inserted into the reactor at the start of an experiment, or hydrogen gas is replaced with oxygen gas for oxygen chemisorption during an experiment, some air or hydrogen is trapped inside the reactor. It is essential to remove the undesirable gases to avoid complications arising from the oxygen present in the air or explosion of hydrogen/oxygen gas mixture at high temperatures. A model MS-90-AB Veeco leak test station is attached to the reactor vent line so that a vacuum of 1-10 μHg can be obtained on the rough pump of the station alone. Pressures as low as 10^{-5} Torr can be attained using the diffusion pump of this station, but leaks at some joints makes it impossible to obtain such low pressures in practice. Thus, only the rough pump is used in experiments.

2.8 Flow & Pressure Control

2.8.1 Flowmeters

The only device to control the reactant gas flow rate is a set of two parallel Cole-Parmer variable area flowmeters, one with glass float ball and one with 316 stainless steel float ball. With this set up an air flow rate range from 0.50 to 832 ml/min can be obtained. The flowmeters are calibrated for helium

and hydrogen gases by a soap-bubble flowmeter.

2.8.2 Pressure Regulators

There are three different pressure levels in this complete reactor system; reactor vessel pressure, pressure at the cold traps, and the pressure at the flow meters (which is virtually atmospheric). For each pressure level, pressure regulators are used: Matheson two-stage high-pressure regulators at the hydrogen and helium cylinders which feed the reactor, a two-stage Matheson pressure regulator model 3104A which reduces the reactor pressure to the GC carrier gas pressure of 30 psi, and a Fairchild-Kendall pressure regulator model 10 to reduce the pressure further to atmospheric pressure of the flowmeters.

2.9 Rupture Disc

The high pressure hydrogen gas is fed from a high pressure cylinder (2500 psi) to the reactor at 1000 psi pressure through a two stage pressure regulator. In case this pressure regulator fails or is misadjusted, or the reactant gases inside the reactor explode, the reactor pressure will exceed the maximum allowable working pressure (MAWP) and the reactor vessel will be damaged. Thus a rupture disc is installed in the feed line such that it will rupture if the pressure is raised above MAWP, thus releasing the pressure. For this purpose a Fike stainless steel 316 Conventional Prebulged rupture disc (½") is used. The details of the calculations for the specifications are presented in the Rupture Disc section in Appendix A.

The stamped burst pressure of the purchased discs is 1448 psi and the recommended ratio of operating pressure to burst pressure for this particular rupture disc is 70% [82]. The ASME code concerning rupture discs requires burst pressure not to exceed MAWP when the rupture disc is the primary or sole relieving device [82]. This implies that the reactor wall can be raised only to a temperature where the MAWP is 1448 psi, as opposed to 1100 psi MAWP at 1000 ° C. As calculations in the Rupture Disc section of Appendix A indicate, this maximum operating temperature is 970 ° C, which is very close to the original design temperature of 1000 ° C. The reason the temperatures are is that in the latter case the reactor was overdesigned using Barlow's formula, and in the former case Lamé's formula (Equation 2-28) was used with shear thermal stresses being taken into account.

2.10 Sample Holders

For intrinsic reaction rate studies two different types of sample holders were used as illustrated in Figure 2.4; a ceramic tube sample holder and a quartz sample holder. Both of these sample holders are inert toward carbon, hydrogen and methane, and with each one a 250 or 325 mesh 316 Stainless Steel 316 screen was used to avoid blowing the carbon out of the sample holder. The ceramic sample holder consists of a ceramic tube which was made into a boat (1" long and 1/8" deep) using Aremco high temperature 503 ceramic adhesive and which holds about 50 mg of Raven 16. The quartz sample holder is a custom designed boat (2½" long and ½" deep) made from 5/8" OD quartz tube, and holds 1.5 g of carbon.

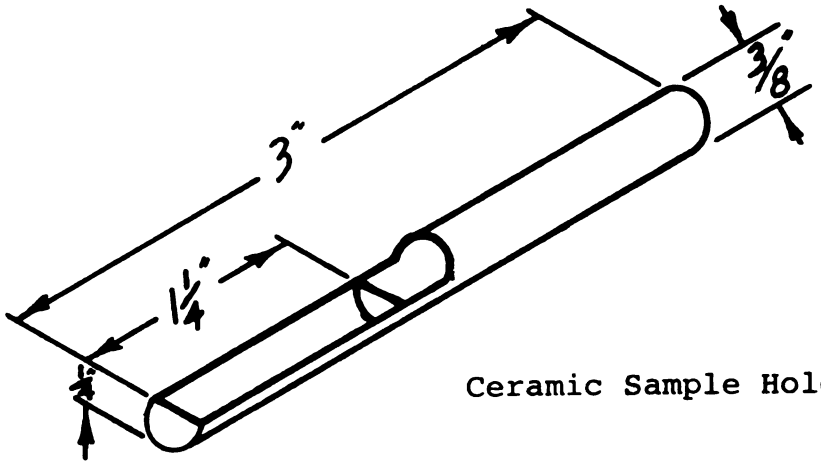

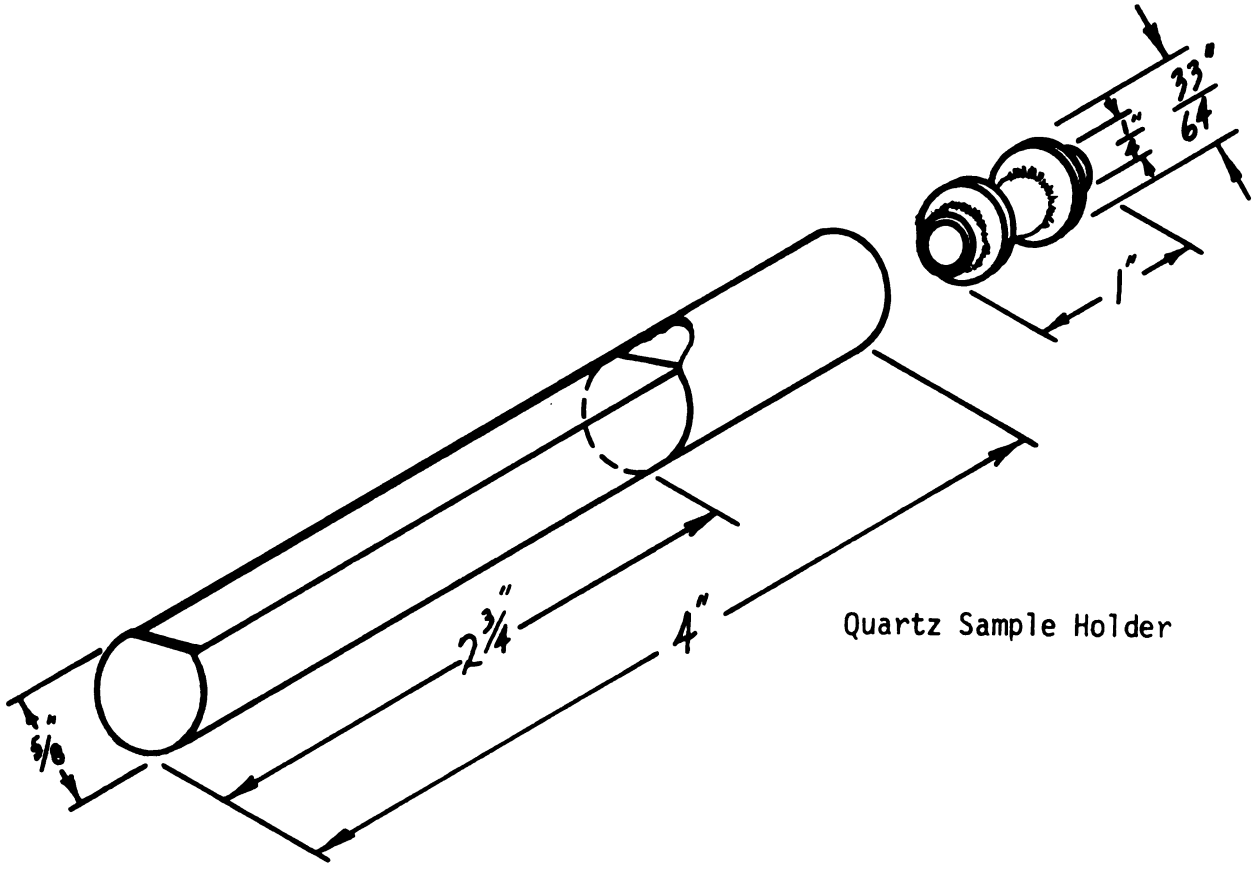

Figure 2.4 Sample holders used for hydrogasification studies.

2.11 Temperature Measurements

The temperature of carbon samples during experiments are measured using two 30" subminiature (0.040" sheath diameter) Chromel Alumel thermocouple probes with 304 Stainless Steel sheath, $\pm 1\,^{\circ}C$ accuracy. These thermocouples are inserted into the reactor through a two-hole Conax fitting (with Viton sealant), mounted on the reactor vessel cover disc, and the central exit tube. One thermocouple is inserted inside carbon bed and the other thermocouple is in the gas phase above sample holders. Chromel Alumel thermocouples are suitable for high temperature operations in reducing as well as oxidizing atmospheres.

Chapter 3

Characterization of Carbon

The reactivity of a carbon sample toward reactant gases depends on various parameters such as the extent of crystallinity and graphitization of the carbon, the amount and nature of impurities in the carbon, and the interfacial surface area available for reaction. For instance, a carbon sample with a high degree of order and crystallinity is less reactive than an amorphous carbon sample (carbon with no order at an atomic level). The impurities such as iron and sulfur in a carbon sample, on the other hand, may enhance or reduce the gasification rate, respectively, depending on the nature of reactant gases. A carbon sample with a high surface area would react with gases faster than a similar carbon with a lower surface area because more gaseous molecules would attack the carbon surface when the surface area is higher and hence a higher

reaction rate is obtained. Furthermore, these parameters may also influence the activity of a catalyst similarly. For example, the kinetic data obtained for gasification of a carbon might be very different from those for another type of carbon loaded with the same catalyst due to different degrees of crystallinity or impurity content.

Therefore, in kinetic studies of catalysis for carbon gasification it is essential to determine the extent of contributions from these sources to observed reaction rates before the sole effect of a catalyst is evaluated. However, before the extent of contributions from these sources to gasification rates can be measured, their relative magnitudes should be estimated; *i.e.*, the magnitude of surface area, the degree of crystallinity and the amount of impurities in a carbon sample should be known or, in other words, a carbon sample should be *characterized* first.

For gasification studies three kinds of carbons were used, as will be discussed in Chapters 4 and 5; activated coconut charcoal, graphite and carbon black.

3.1 Coconut Charcoal

The coconut charcoal used was a 50-200 mesh activated coconut charcoal obtained from Fisher Scientific Company.

3.1.1 BET Surface Area

The surface area of this carbon was measured by volumetric adsorption of nitrogen gas at liquid nitrogen temperature using BET analysis [83]. Nitrogen gas adsorption partial pressures were 59 Torr, 147 Torr and 212 Torr and

adsorptions at each nitrogen gas partial pressure were carried out in triplicate for the sake of accuracy. The calculated surface area was 577 m^2/g assuming a coverage of 16.2 $Å^2$ by a nitrogen molecule. Large carbon particle sizes and high surface area indicate a high degree of porosity of this particular type of carbon.

3.1.2 Ash Content

The ash content (the residue left behind after burning the carbon in air) was determined by burning three samples of this carbon (1.7363 g, 3.3485 g and 5.4090 g) at 850 ° C in air for 11 h in 60 mm ID evaporating dishes. The samples were then cooled down in a desiccator and subsequent weight measurements showed an average ash content of 3.70%.

3.1.3 Impregnation with K_2CO_3

The carbon samples were loaded with K_2CO_3 by wet-impregnation with a mixture of K_2CO_3 solution/acetone and subsequent drying. First, 200 ml of 1.799 M solution of potassium carbonate was prepared from analytic reagent Mallinckrodt granular anhydrous potassium carbonate. Then 8.0 ml, 16.0 ml and 24.0 ml of this solution were diluted to 60 ml with doubly distilled water in 200 ml beakers and were each mixed with 20.0 g of carbon to yield 9.04 wt%, 16.6 wt% and 23.0 wt%-K_2CO_3 samples, respectively. After 5 minutes of mixing, 2 ml of acetone was added to each beaker and the beakers were covered and were left overnight.

The samples were dried at 90 ° C overnight without mixing and the result was a large degree of recrystallization of potassium carbonate. Thus 45-50 ml distilled water was added to each beaker with 5 minutes of mixing to redissolve the potassium carbonate crystals. The samples were then slowly dried by heating them at 90 ° C for 8 h with stirring every 30-45 minutes. Following

that, the samples were kept at 60 ° C for one week and stirred once a day, and then kept at 120 ° C for two days. The samples were finally cooled down and were stored in 20 oz french square glass bottles with screw caps.

3.1.4 Reactivity

These K_2CO_3-impregnated samples were highly reactive toward 500 psi hydrogen gas at 865 ° C (see Section 5.3). The 23.0 wt%-K_2CO_3 sample was so reactive that more than half of the sample gasified before the steady state temperature of 865 ° C was reached. Thus, no useful kinetic data at low conversions could be obtained from this carbon and, therefore, it was decided to abandon this type of carbon for further studies, and to use other carbons such as graphite for the experiments.

3.2 Graphite

Since coconut charcoal was too reactive, it was decided to use a less reactive carbon sample; a carbon sample with a higher degree of crystallinity and lower surface area. For this purpose a non-porous -325 mesh Alpha Products graphite powder with a purity of 99.5% was tried.

3.2.1 BET Surface Area

The BET surface area of this carbon was determined using the same technique that was used for coconut charcoal with one minor modification; the graphite sample was degassed at 125 ° C for 30 min before nitrogen adsorption experiments. The nitrogen adsorption partial pressures were 49 Torr, 144 Torr and 215 Torr, and the surface area was calculated to be 6.58 m^2/g. However, it

has been reported that this calculated surface area is too low and the effective coverage area by nitrogen molecules should be taken as 20 $Å^2$ per molecule instead of 16.2 $Å^2$ that has traditionally been used [84]. A proposed explanation is that nitrogen molecules are localized at graphite lattice sites so that each nitrogen molecule fills four of the unit hexagonals, an area of 21 $Å^2$. Thus the actual surface area was 8.12 m^2/g.

3.2.2 Impregnation with K_2CO_3

This graphite powder was loaded with K_2CO_3 to 1.00 wt%, 4.73 wt% and 9.04 wt%-K_2CO_3 samples by wet-impregnation with a mixture of K_2CO_3 solution/acetone and subsequent slow drying. First, 0.8 ml, 4.0 ml and 8.0 ml samples of a 1.799 M potassium carbonate solutions were added to three 100 ml beakers using a 1 ml in 1/100 pipette and were diluted to 40 ml with doubly distilled water. Then 40 ml acetone was added to each beaker, stirred and 20.0 g graphite was added. After stirring the solid-liquid mixture well, the beakers were covered and were saved overnight. Samples were dried slowly at 65 ° C with stirring them every 15 to 30 minutes until the powders dried enough to agglomerate. After drying the samples completely at 120 ° C overnight, they were ground in a pestle and mortar and stored in 20 oz french square glass bottles with screw caps.

A blank graphite sample was also prepared along with other samples in an identical manner except for the fact that no potassium carbonate solution was used.

3.2.3 Reactivity

The measurement of gasification rates of this carbon at 865 ° C was, however, a problem. As will be discussed in Chapter 4, the gasification rate of

fresh carbon was so low that there were significant interferences from the reaction of the reactant hydrogen gas with metallurgical carbon that deposited out on the reactor wall during thermal cycles from room temperature to reaction temperatures and vice versa. These reaction rates in general were higher than the gasification rates of graphite samples.

Thus it was decided to insert a quartz tube lining into the reactor vessel to reduce the reaction of hydrogen gas with the metallurgical carbon. It was also decided to find an alternative carbon sample that has higher reactivity than this rather inactive graphite sample, but still less reactive than the coconut charcoal.

3.3 Carbon Black

The carbon black used for further studies was Fisher Scientific lampblack (Raven 16 carbon black) which is a graphitic furnace black. This carbon black is non-porous and consists of spherical particles with average diameters of 60-70 nm as determined by electron microscopy. The geometric surface area corresponding to 65 nm particles is 48.5 m^2/g.

3.3.1 Ultimate Analysis & Ash Content

The ash content of this carbon black was reported to be 0.3 wt%; this was verified by an independent ultimate analysis test carried out by Commercial Testing & Engineering Company. The elemental analysis of the ash is presented in Table 3.1.

An ultimate analysis revealed that this particular carbon black is 97% carbon; the remainder is impurities such as moisture, sulfur, *etc.*, as can be seen

in Table 3.2.

Table 3.1 Elemental analysis of ash in Raven 16

Element	Concentration (ppm)
Fe	450
Ca	250
Na	200
Mg	30
Al	30
Ti	10
K, Si	remainder

Table 3.2 Ultimate analysis of Raven 16

Impurity	wt%
Moisture	0.46
Carbon	96.92
Hydrogen	0.27
Nitrogen	0.29
Sulfur	1.54
Ash	0.31
Oxygen (difference)	0.21

Sulfur constitutes almost half of the impurities in the carbon and is present as S bonded to carbon black (free S<0.03 wt%). Volatile loss upon heating between 120 ° C and 950 ° C in inert atmosphere is 0.9 wt%.

3.3.2 Impregnation with K_2CO_3

Carbon black samples were impregnated with K_2CO_3 solutions to potassium carbonate loadings of 1, 5 and 10 wt%-K_2CO_3. These samples were prepared by first diluting 0.80 ml, 4.20 ml and 9.00 ml of a 1.799 M potassium carbonate solution to 90 ml with equal volumes of doubly distilled water and

acetone and then adding 20.0 g of carbon black to each solution. The solid-liquid mixtures were mixed thoroughly, covered and left overnight (14 h), then were heated in an oven at 80 ° C with occasional stirring until dry. The samples were then heated at 120 ° C for 24 h, ground in a mortar and pestle and stored in 20 oz french square glass bottles with screw caps. The actual potassium loadings of these samples were 1.02 wt%, 4.96 wt% and 9.99 wt%-K_2CO_3 which compares rather well with the NAA measurements of 1.1 wt%, 5.1 wt% and 10.0 wt%-K_2CO_3.

A blank sample was also prepared. This sample was treated similar to the impregnated samples except for the fact that no potassium carbonate solution was added.

For some later experiments some carbon black samples underwent treatments such as hydrogasification, degassing and combustion before impregnation. For impregnating these samples smaller proportions of acetone were tried and it was found that volumes of acetone as little as 1/3 of the volume of water used is enough for wetting hard-to-wet carbon surfaces like degassed carbon. For samples which were oxidized in oxygen the carbon surface could be readily wetted and no acetone was needed. This reduced the drying time period considerably. Furthermore, it was found that depending on the treatment prior to impregnation less water could be used to make a moderately thick slurry which could be dried much faster.

3.3.3 BET Surface Area

The surface area of this carbon black, fresh or gasified up to 70% conversion, was measured using the same technique that was used for coconut charcoal and graphite. The surface areas of the 10 wt%-K_2CO_3 samples at various levels of gasification at 865 ° C in 500 psi hydrogen gas were also

calculated after washing the samples with doubly distilled water thoroughly to remove residual catalyst, which normally blocks some of the pores making them inaccessible to N_2 gas. The adsorption partial pressure of nitrogen gas in all cases was less than 200 Torr. The results are presented in Figure 3.1.

It can clearly be seen from Figure 3.1 that the surface area increases linearly from 20 m^2/g to 400 m^2/g at 60% conversion. This increase is much higher than what is expected from a simple reduction in the diameters of the carbon particles (geometric surface area of 65 nm particles after 50% conversion is only 61.1 m^2/g), and development of a high degree of porosity is the only plausible explanation. This phenomenon has already been observed for combustion of carbon blacks [85,86].

BET analysis of N_2 adsorption isotherms has been used as a fairly accurate means of measuring the total surface area of both porous and non-porous carbon blacks [87-91]. Application of *t*-method to porous carbon blacks with substantial volumes of pores with diameters from 4 Å to 15 Å has shown that the classical BET analysis of N_2 adsorption data is within 15% of the results from the *t*-method [92]. Further studies of porous furnace blacks by *t*-method have showed much better agreement [93,94].

However, it has been suggested that the classical BET surface area may be incorrect due to capillary condensation of nitrogen gas in the micropores [95]. But, the application of a modified BET method to low temperature adsorption of nitrogen gas on coconut charcoal has shown no sign of capillary condensation for adsorption pressures of less than 150 Torr [96]. Furthermore, the application of Polanyi-Dubinin Potential Energy equation to CO_2 adsorption isotherms at -78 °C on coconut charcoal and some carbon blacks also has shown no sign of capillary condensation of CO_2 in the micropores, and the surface area thus calculated agreed very well with the BET area of CO_2 adsorption [97]. Hence,

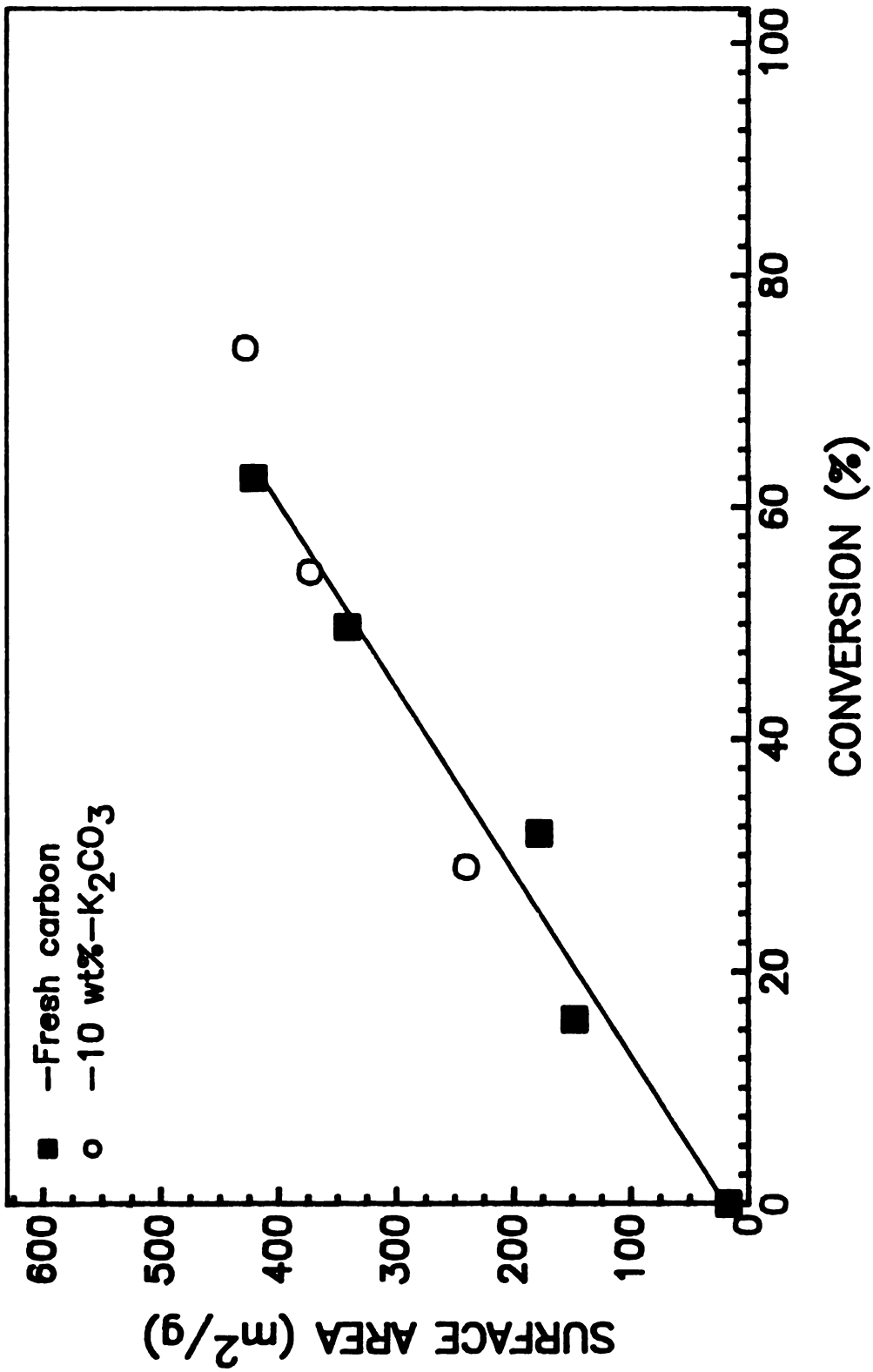

Figure 3.1 N_2-BET surface area of Raven 16 at various conversions.

the BET surface area from CO_2 adsorption isotherms seems to be a more reliable means of measuring the surface area.

The BET surface area of a 72% hydrogasified sample was measured, after washing off all the residual catalyst, from adsorption isotherms of both low temperature N_2 adsorption and CO_2 adsorption at -78 ° C. The surface areas were essentially the same, suggesting that there was no capillary condensation of nitrogen in the pores that were developed during gasification. Therefore, the measured N_2 BET surface areas presented in Figure 3.1 are fairly accurate at all conversions, and, in addition, indicate that loading carbon with potassium carbonate does not change the course of development of pores in a carbon sample during hydrogasification.

3.3.4 Reactivity

As expected, this carbon lampblack was more reactive than the graphite powder because of lower crystallinity and higher surface area, and still less reactive than the coconut charcoal due to its much lower surface area. The hydrogasification rates of this carbon black, catalyzed and uncatalyzed, were "ideal" (higher than 60% conversion in 8 h) and could be measured with reasonable accuracy (conversions obtained from graphical analysis were within 10% of the weight measurements). Furthermore, steady state conditions could be reached at less than 10% conversion, as opposed to more than 50% conversion for the charcoal gasification. Therefore, it was decided to use this carbon black for further studies of K_2CO_3-catalysis of hydrogasification, and thus this carbon was further characterized.

3.3.5 XRD Analysis

The X-ray diffraction analysis of this carbon black was conducted by Mr. Xiao-Wen Qian at the Department of Physics at Michigan State University, using the analysis discussed in detail by Heckman [98]. The average interlayer spacing of the layers was found to be 3.54 Å which is larger than 3.354 Å interlayer spacing of ideal graphite layers. The average diameter L_a of the carbon layers and the average distance L_c between the top layer and the bottom layer of a crystallite were calculated to be 37 Å and 30 Å, respectively.

The diffraction pattern and crystallite parameters indicated that there is a definite structure and order in this carbon black, and thus this carbon is not amorphous. However, the size of the crystallites are much smaller than the crystal sizes of graphite (on the order of μm) and from the interlayer spacings it can be inferred that the stacking of the layers and their relative orientations in this carbon black are completely random [99].

3.3.6 Microstructure of Carbon Black

The term microstructure refers to the internal (paracrystalline) organization of the carbon within the particles of the carbon black. By the late 1940's two different models had been proposed for microstructure of carbon blacks: *i*) 'random crystallite orientation model' based on X-ray results which assume that crystallite (parallel layer planes of carbon) orientation is random within particles and that dimensions of all crystallites are similar to the average values found by X-ray technique [100,101]; and *ii*) 'tangential layer plane orientation model' based primarily on dark-field electron microscope studies [102,103]. The major shortcoming of the latter model is that it does not distinguish clearly between crystallites and single layer planes and makes no allowance for distribution in crystallite dimensions.

In 1960's, with the advancement of high resolution electron microscopy, some new models were suggested. Donnet & Bouland [104] suggested a model consisting of uniform concentric crystallites throughout a carbon black particle. However, this model could not explain the mode of oxidation of carbon blacks; namely, combustion of thermal and furnace blacks were from inside out [105]. Based on this observation and further X-ray and electron microscope studies of oxidized carbon blacks, Heckman & Harling [105] proposed 'concentric crystallite model' in which outer crystallites of a carbon black particle are larger, more perfect and their layer planes are generally oriented parallel to the particle surface. In contrast, the central portion is made up primarily of small, imperfect crystallites, single layer planes and possibly disorganized carbon (carbon not incorporated into layer planes). Hess *et al.* [106] supported this model with their conventional and diffracted beam electron microscopic results. Donnet *et al.* [107] improved this model to incorporate their speculated closed porosity within the particles. Heidenreich *et al.* [108] proposed a similar model on the basis of results obtained using the lattice fringe imaging techniques which give a more detailed picture of the organized parts of the carbon.

However, independent X-ray studies of carbon blacks by Ergun [109] led to the conclusion that the fundamental microstructural unit of carbon black is the graphitic layer, not the crystallite. Ergun gave convincing evidence (from atomic radial distribution functions) that the crystallites of carbon blacks as derived from X-ray analysis are not true microcrystals, but are in reality a chance parallel alignment of successive carbon layers. He also concluded that the crystallite layer size L_a , derived from the width of the X-ray (hk) reflection, is less than half that of the distorted graphitic layer, and that layer stackings may be more extensive than the profiles of (001) reflection indicate. Ergun's paracrystalline model was composed of large anisotropically distorted layers

oriented in parallel stacks having a greater interlayer spacing than graphite, due to interstitials and gross distortions. From this model it is expected to observe crystallites with a variation or distribution in the interlayer spacing under electron microscope, rather than a single interplanar distance. This has been shown to be indeed the case [110].

Ban & Hess [111] obtained the first direct images (high-resolution phase-contrast transmission electron microscopy) of the defective and distorted, but generally concentric, graphitic layers in normal carbon blacks. Based on the above observations, Harling & Heckman [112] corrected their earlier model [105] to 'concentric layer orientation model' which incorporated many of the major aspects of the earlier paracrystalline and concentric crystallite models. According to this model, each carbon layer has one or more planar portions which when stacked roughly parallel and equidistant to adjacent planar domains will function as a crystallite plane in its ability to diffract X-rays. The central portion is composed of the smallest layers with the greatest curvature and, therefore, with a more open structure. This model can best explain the up-to-date experimental observations such as the combustion of furnace carbon blacks and is still current.

Hence, it seems that the calculated crystallite dimensions presented in the XRD Analysis section cannot provide any definitive information about the degree of microcrystallinity or order of the carbon black particles. However, they do indicate that the high temperature treatment (1000 ° C) does not induce any detectable changes in the microstructure of the carbon particles, otherwise the interlayer spacing would decrease and would have a narrower distribution [110], or would be reflected in the crystallite dimensions [109]. These effects were not observed; the diffraction pattern of the fresh carbon and the heat treated carbon were identical.

3.3.7 XPS Analysis

The surface of the carbon black was examined by XPS, which chemically characterizes the outermost 10 Å of the surface [113]. The surfaces of carbon black samples that were degassed at 1000 ° C under vacuum for 15 h or hydrogasified to 47% conversion at 865 ° C were also analyzed by XPS. It can be seen from the XPS spectra of these three samples (Figure 3.2) that there is no trace of nitrogen on the surfaces of these carbons (N_{1s} binding energy of nitrogen is 402 eV [114]) in spite of the fact that 0.29 wt% of the carbon is nitrogen. Sulfur, which constitutes half of the impurities, could be identified only on the surface of the fresh carbon, implying that bonds between sulfur and the carbon are weak and are readily broken upon heating to high temperatures.

In contrast, oxygen is present on the surface of all three carbons despite the fact that it is present in the bulk of carbon in amounts much less than sulfur. However, carbon is known to adsorb oxygen even at room temperature, and since the samples were exposed to air for a few days before they were analyzed by XPS, the measured concentrations of oxygen on the surfaces of these carbon are probably higher than those under experimental conditions. The XPS-measured surface compositions of sulfur, oxygen and carbon are presented in Table 3.3.

3.3.8 Oxygen Surface Complexes

As discussed in Chapter 1, the oxygen present on the surface of carbon may be in the form of acidic, basic or neutral complexes depending upon the conditions under which they are formed. The influence of these acidic and basic groups on hydrogasification rates as well as the catalysis by K_2CO_3, discussed in Chapters 4 and 5, is the cornerstone of the studies presented here. Thus, the formation and the nature of oxygen surface groups need to be characterized first.

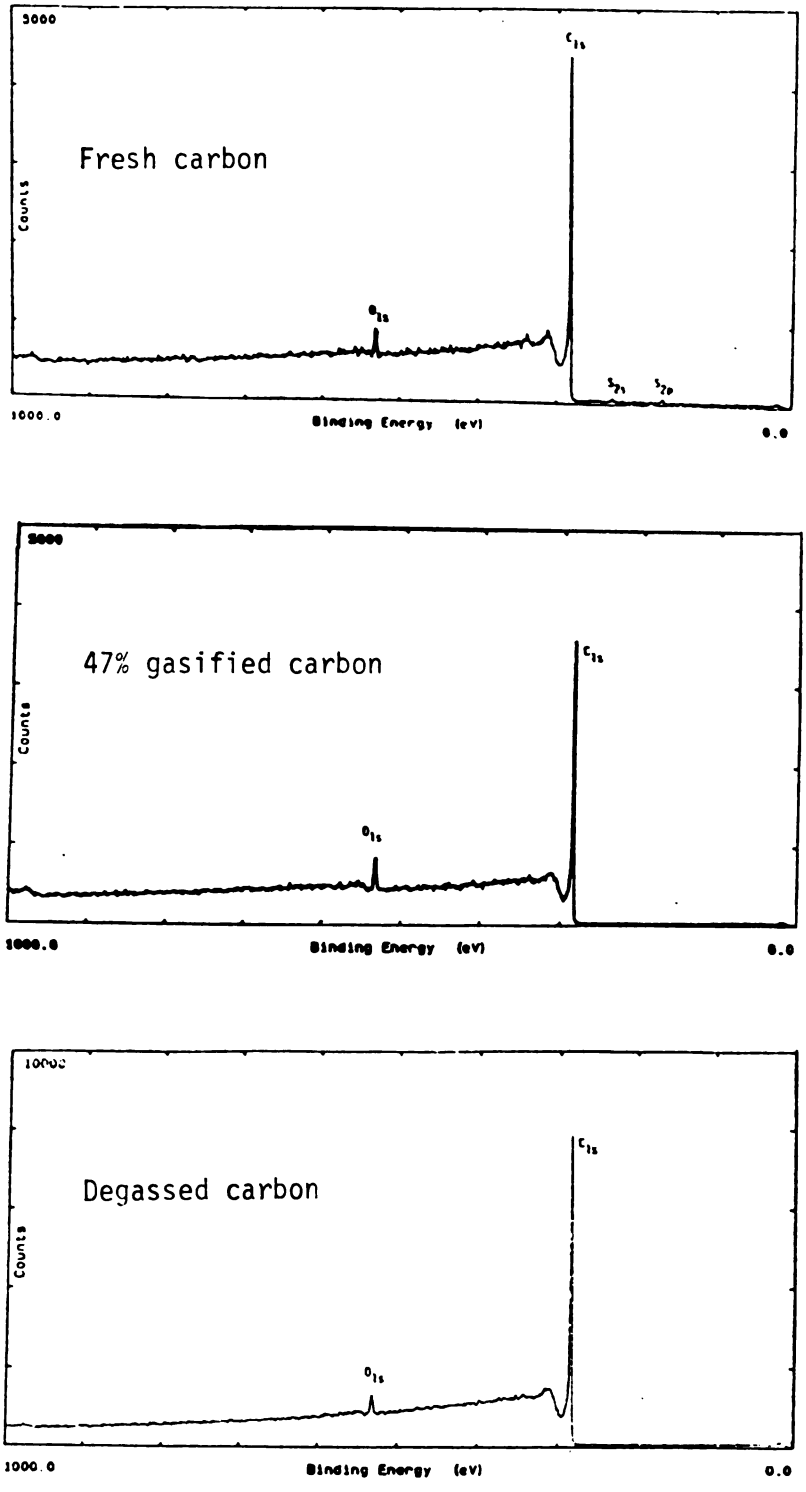

Figure 3.2 ESCA scan of fresh and heat treated Raven 16.

Table 3.3 Surface concentration (atomic %) of non-metallic elements in Raven 16

Element	Fresh carbon	47%-gasified carbon	Degassed carbon
C	94.52	94.11	95.75
O	4.63	5.89	4.26
S	0.85	0.00	0.00
Others	0.00	0.00	0.00

Acidic or basic surface groups were introduced onto the surface of the carbon via combustion in oxygen at 400 ° C and 800 ° C, respectively. However, no attempt was made to chemically analyze and identify individual oxygen-containing surface groups (initially present in the fresh carbon or introduced via combustion) at different stages of the experiments. Instead, pH measurements of suspensions of carbon samples were used as a gross and semi-quantitative means of identifying acidic or basic character. Furthermore, within the pH range of solutions of these experiments, the pH is expected to be related to the oxygen group concentrations, and thus 'relative' changes of the concentrations can be estimated from changes in pH. It has been shown that the pH values of these suspensions closely follow the acidic or basic nature of the samples in a qualitative way [115]; *i.e.*, basic surface groups give rise to a basic pH value in the suspension and acidic groups give rise to an acidic pH value.

3.3.8.1 Procedure

3.3.8.1.1 Combustion

Combustion of carbon samples (oxygen chemisorption) was carried out in the reactor used for hydrogasification studies (described in detail in Chapter 2). Oxygen chemisorption, either at 400 ° C or at 800 ° C, was carried out by first raising the temperature to the desired chemisorption temperature under vacuum

($\sim$ 10 μHg) followed by addition of about 0.33 cc (STP) O_2 gas per milligram of carbon sample. The reactor was isolated (two hours at 800 ° C or 12-15 hours at 400 ° C), then evacuated, and the next step was carried out.

3.3.8.1.2 pH Measurement

pH measurements were made in parallel 25 ml Erlenmeyer flasks to ensure that changes in pH were solely due to the presence of carbon. Carbon samples of 18-24 mg were added to the same flask every time and 10 cc of a 0.1 M KCl solution was added to each flask with a pipette. Potassium chloride solution was used instead of pure distilled water because oxygen groups on carbon surfaces produce a bigger change in the pH of KCl solution than of distilled water [115]. The flasks were then attached to water-cooled condensers and the solutions were boiled for 2-3 hours on a hot plate. After boiling the flasks were sealed with glass stoppers and cooled to room temperature. The solutions were then transferred to glass bottles and the pH of each was measured by a Fisher Accumet Model 825 MP pH-meter equipped with a Ω-Metrohm glass pH electrode or a Cole Parmer epoxy-body pH electrode.

3.3.8.2 Results

The results of pH measurements of various carbon samples in 0.1 M KCl solution are tabulated in Tables 3.4-3.8. The change in pH of the KCl solution, ΔpH, is a measure of the acidity/basicity of the oxygen complexes on the carbon surface; a positive ΔpH, for instance, demonstrates the presence of basic groups because the pH of the KCl solution is increased in the presence of carbon. For a few carbon samples, however, the oxygen surface groups could not be characterized from the pH measurements because of either the hydrophobic nature of the carbon surface or the presence of potassium on the surface. The

Table 3.4 ΔpH of 0.1 M KCl solution for fresh, degassed and gasified carbons

Treated Sample	ΔpH
Fresh carbon	did not wet
Degassed carbon	did not wet
Gasified 24% in H_2	+2.9
Gasified 24% in H_2	+2.6
Degassed and gasified 32% in H_2	+2.6
Heated at 400 ° C *in vacuo* for 2 h	did not wet
Heated at 800 ° C *in vacuo* for 2 h	+0.5
Heated at 800 ° C in helium for 2 h	+0.6

Table 3.5 ΔpH of 0.1 M KCl solution for carbons oxidised at 400 ° C

Treated Sample	ΔpH
Fresh carbon oxidized for 2 h	-0.75
Fresh carbon oxidized for 15 h	-2.1
Gasified 42% in H_2, then oxidized for 2 h	-0.4

Table 3.6 ΔpH of 0.1 M KCl solution for carbons oxidised at 800 ° C

Treated Sample	ΔpH
Fresh carbon oxidized for 2 h	+1.6
Fresh carbon oxidized for 2 h	+1.44
Degassed carbon oxidized for 2 h	+0.3
Gasified 22% in H_2	+2.7
Gasified 22% in H_2	+2.5
Gasified 43% in H_2, then oxidized for 15 min	+2.4
Gasified 43% in H_2, then oxidized for 2.5 h	+2.7

surface of a fresh untreated carbon or a degassed carbon sample did not wet for reasons that will be discussed later. Addition of a small amount of acetone to the solution resolved this problem, but it was observed that acetone influenced the pH value of any carbon suspension, although these changes were small. The pH values of the suspensions of these hard-to-wet samples were virtually the

same as that of the KCl solution. Potassium, whether in carbonate or reduced metallic form, yields a basic solution and if present on the surface of a carbon increases the pH value of its suspension drastically, thus making it impossible to characterize surface groups. Therefore, the only meaningful pH measurements were those of samples that contained no catalyst and were wet without acetone; *i.e.*, oxidized and/or partially gasified pure carbon samples.

Examination of the ΔpH values in Tables 3.4 and 3.6 also shows that the pH measurements are fairly reproducible. The ΔpH of duplicate suspensions of a 24% gasified sample in Table 3.4 and those in Table 3.6 indicate that the ΔpH measurements agree within 0.3 pH units.

Tables 3.4, 3.7 and 3.8 show that a partially gasified carbon black, irrespective of the treatment preceding the gasification, contained basic surface groups, provided that gasification proceeded to the extent that carbon surface influenced by treatments had been gasified away (> 10-20 wt%). This observation is further illustrated in Figure 3.3; different points represent carbon samples that have been treated differently (degassed, oxidized in oxygen or hydrogasified individually or in combination) and then all have been hydrogasified for at least an additional 10% conversion. These carbon samples all exhibit a basic surface character.

The surface of a carbon sample oxidized at 400 °C had an acidic character, as can be clearly seen from Table 3.5. Table 3.6 shows that when oxidation took place at 800 °C, basic groups were formed on the surface of the carbon. It can also be seen that time periods as low as 15 min were enough to saturate the surface with oxygen groups at 800 °C, whereas 15 h was necessary at 400 °C. Finally, an interesting result is the observation that a fresh carbon wetted easily once it was heated to 800 °C *in vacuo* or in helium. Similar treatment at 400 or 1000 °C did not give the same result (Table 3.4).

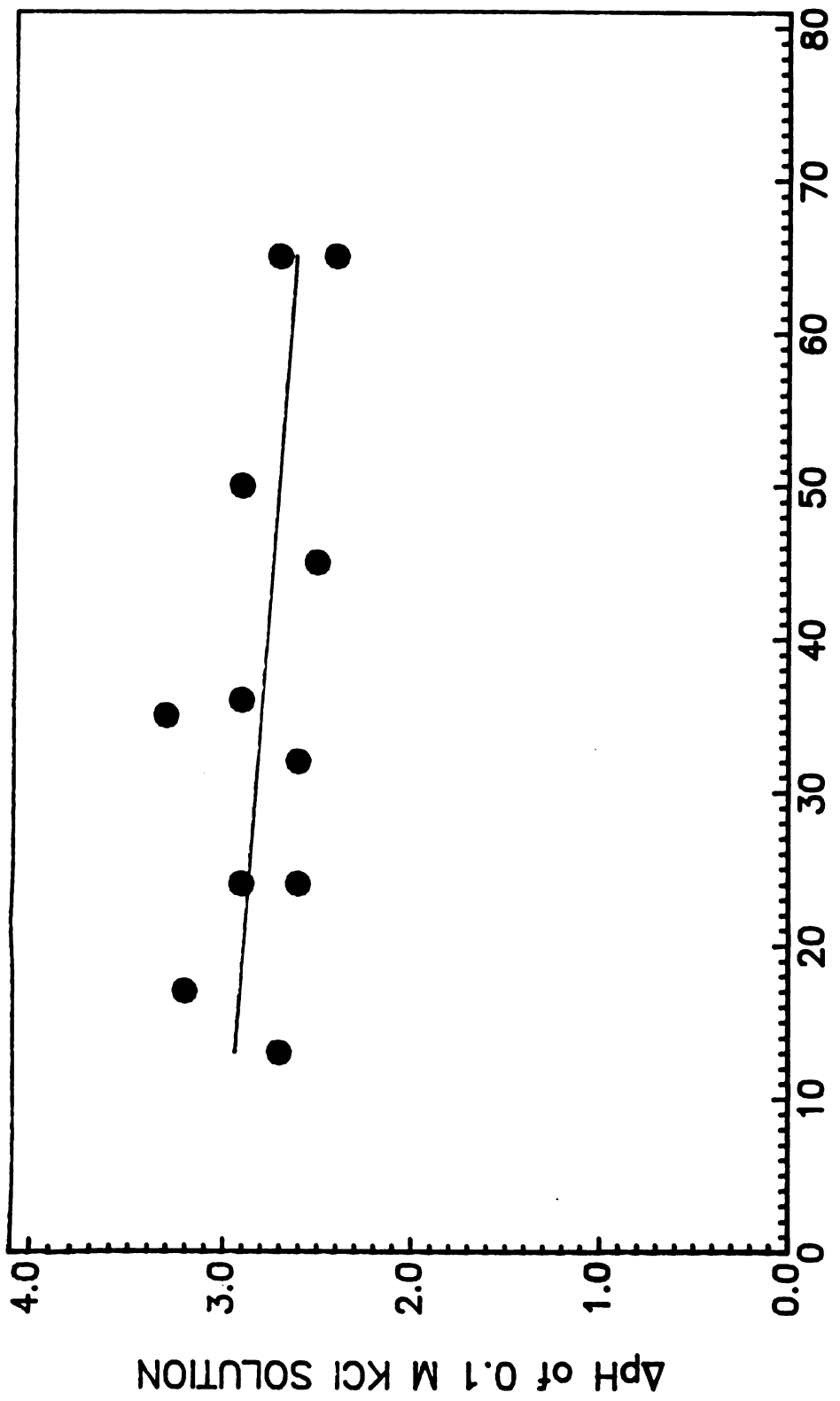

Figure 3.3 Nature of oxygen complexes in bulk Raven 16.

Table 3.7 ΔpH of KCl solution after combustion at 400 ° C and hydrogasifying

Treated Sample	ΔpH
Oxidized then gasified 8% in H_2	+2.7
Oxidized then gasified 11% in H_2	+3.2
Oxidized then gasified 31% in H_2	+2.9
Oxidized then gasified 38% in H_2	+2.5
First gasified 43% in H_2, then oxidized and then gasified additional 17% in H_2	+2.4

Table 3.8 ΔpH of KCl solution after combustion at 800 ° C and hydrogasifying

Treated Sample	ΔpH
First oxidized then gasified 30% in H_2	+3.3
First gasified 22% in H_2, then oxidized and then gasified additional 22% in H_2	+2.9
First gasified 43% in H_2, then oxidized and then gasified additional 16% in H_2	+2.7

3.3.8.3 Discussion

Examination of Tables 3.5 and 3.6 reveals that after oxidation of a carbon sample at 400 or 800 ° C, acidic or basic groups are formed on the surface of carbon consistent with literature results. The important result is the observation that carbon surfaces show basic character after being gasified in pure hydrogen for more than 10-20% conversion, irrespective of their treatment prior to gasification (Tables 3.4, 3.7 and 3.8). The presence of nitrogen, sulfur, hydrogen, or ash in the carbon cannot explain this basic character, because the XPS spectrum of a degassed or a 47% gasified sample (Figure 3.2) did not show any trace of the elements on the surface, and the ash content of 0.3 wt% is too low to account for such a high pH. Thus, it can be concluded that the oxygen surface groups are solely responsible for basic and hydrophilic character of the surface.

The results presented in Table 3.4 show hydrophobicity of the surface of fresh carbon sample, in spite of a surface coverage by oxygen groups of nearly 13% as measured by XPS. This hydrophobicity was also observed for a carbon sample degassed at 1000 ° C as well as for a fresh carbon heated *in vacuo* at 400 ° C, but not for a sample heated *in vacuo* at 800 ° C. This apparent anomaly is explained by two different effects. It may be that a small amount of residual hydrocarbon material (from which this particular carbon was produced) was adsorbed on the surface, making the XPS-detected oxygen surface groups present on the fresh carbon inaccessible and thus the surface hydrophobic even at 400 ° C. These organic deposits were desorbed or decomposed at some temperature between 400 and 800 ° C, thus exposing oxygen groups and making the surface hydrophilic. Further evidence for this argument was a yellow film deposit on the inner quartz lining of the gasification reactor which was observed upon heating carbon samples to high temperatures. This deposit was soluble in acetone but not in water. Once fresh carbon was wash with acetone and dried, the surface could be wetted in water easily. The prolong heating at 1000 ° C for degassing was apparently severe enough to remove oxygen groups from the surface, hence the lower surface oxygen coverage and the hydrophobic surface of the degassed carbon.

The GC analysis of the gas collected continuously during degassing at 1000 ° C of a fresh carbon sample indicated the release of large amounts of CO from thermal decomposition of oxygen groups of the carbon sample, 4.94 cc CO and 0.207 cc CO_2 per gram of carbon. This ratio of CO/CO_2 is virtually the equilibrium value at 1000 ° C, and consequently it is not possible to deduce whether the oxygen groups decomposed to CO or CO_2. The amount of oxygen in the evolved gas could cover about 78% of the total surface area of the initial fresh carbon if each atom of oxygen was assumed to cover 8.3 $Å^2$. But, the

XPS-measured oxygen surface coverage of fresh carbon was about 13%, implying that oxygen was released from groups both in the bulk carbon near the surface and from the surface. Apparently, the time it took for the oxygen-containing gases to diffuse out of the carbon particles and carbon bed into the gas stream was long enough to establish equilibrium.

Heating a fresh carbon sample at 865 ° C in helium for 3 hours produced 1.21 cc CO and 0.046 cc CO_2. This amount of oxygen desorbed corresponds to a hypothetical coverage of 19% of the surface area as opposed to the XPS-measured oxygen coverage of 13% of the surface of fresh carbon, implying that most of the oxygen was from the surface. In this case, the CO/CO_2 ratio is higher than the equilibrium value and so it follows that the oxygen groups near the surface of the fresh carbon were mainly non-acidic.

However, the pH measurements of a fresh carbon sample heated at 800 ° C (Table 3.4) indicates slight basicity of the surface (ΔpH = +0.5 - +0.6), and thus it can be concluded that the oxygen groups near the surface of the original fresh carbon are mostly C=O carbonyl groups. Furthermore, the pH measurements of the degassed samples after about 32% gasification (Table 3.4) indicate the presence of much higher concentration of basic surface oxides (ΔpH = +2.6), possibly chromene structures, which are believed to be responsible for the low reactivity of this sample after degassing. The pH measurements of other carbon samples that were not degassed yielded similar pH values after gasification (Table 3.4), suggesting that neither degassing nor gasification decomposed the stable basic groups within the bulk of carbon black. This is consistent with the results obtained by Blackwood [40], who attributed the low reactivity of high-temperature treated char samples to the stable chromene structures. The fact that ΔpH of the suspension of a carbon sample after 32% gasification is 2 units higher than that of a fresh sample implies that the

concentration of basic oxygen surface groups is on the order of 100 times higher in the former case. However, the BET surface area of the 32% gasified carbon is 8-9 times that of the fresh carbon (Figure 3.1) and the XPS-coverage of surface by oxygen is 1.1-1.3 times that of the fresh carbon (Table 3.3), so the net overall coverage of the surface of 32% gasified carbon by oxygen is only 10 times that of the fresh carbon. It thus seems that 10 times more basic oxygen groups are inside the fresh carbon particles than are on their surface.

In summary, it thus can be concluded that oxygen groups initially present near the surface of the fresh carbon are mainly carbonyl groups and those in the bulk carbon are dominantly basic in character. Furthermore, combustion of the carbon in oxygen at 400 ° C and 800 ° C establishes acidic and basic complexes on the carbon surface, respectively, as expected. The significance of these results will be discussed in Chapters 4 and 5 in relation to the activity of potassium carbonate catalyst and the reactivity of carbon toward hydrogen.

Chapter 4

Uncatalyzed Hydrogasification

The ultimate objective is to study the influence of addition of potassium carbonate and oxygen surface complexes on kinetics of hydrogasification of carbons. Thus, the hydrogasification kinetics of carbons in the absence and in the presence of potassium carbonate and oxygen surface complexes must be compared and any observed differences be carefully examined. For instance, if the addition of some oxygen complex on surface of a carbon sample enhances the hydrogasification rate of that carbon, that oxygen surface complex would be definitely involved directly or indirectly in the sequence of events taking place on the surface of carbon during hydrogasification. On the other hand, if addition of potassium carbonate does not result in an enhancement of the hydrogasification rate, the carbonate most likely will not be involved in a catalysis process, at

least in the mode or the way it is added to the carbon.

However, this task necessitates that the measured hydrogasification rates be the true intrinsic reaction rates; *i.e.*, the reaction rates should not be masked by mass transfer limitations within the carbon fixed bed as well as the pores of carbon particles that develop during hydrogasification (see Section 3.3). If there is a substantial mass transfer resistance within the carbon fixed bed, the rate of mass transfer of product gas(es) from within the fixed bed into the bulk gas stream would be much less than the hydrogasification rate deep inside the bed under the bulk gas conditions and, therefore, the partial pressures of gases at carbon-gas interface would be different from those in the bulk gas. Thus, the reaction environment at carbon-gas interface would be different from the bulk gas monitored conditions and, consequently, any correlation of the bulk gas reaction conditions with the observed reaction rates would be meaningless. In addition, this would also mask the true enhancement caused by the catalyst and make the apparent activation energy E_a' much lower than the true activation energy E_a depending on the extent of mass transfer resistance.

There are some other factors such as temperature variation inside the carbon fixed bed that need to be considered before comparing the measured reaction rates. The temperature of the carbon fixed bed could vary within the bed or in different experiments because the carbon sample size varies or the reactor vessel temperature may not be uniform throughout the furnace, and the location of the sample holder may not be exactly the same location for each experiment. The hydrogasification rate is strongly dependent on reaction temperature as is evident in a reported value of 63 kcal/g-mol [116] for the activation energy E_a of hydrogasification of Raven 16. Thus, if the temperature of the carbon fixed bed varies significantly within the bed, the reaction rate would also vary and might result in different overall reaction rates.

Hence, the mass transfer limitations and temperature variation within carbon fixed bed are discussed first and then the influence of oxygen surface groups are presented in this chapter. The influence of addition of potassium carbonate with or without the addition of oxygen surface complexes are presented in Chapter 5. However, a brief review of the literature on hydrogasification of carbons, in the absence of any external catalysts, seems appropriate at this point.

4.1 Background

4.1.1 Hydrogasification Products

Reaction of hydrogen gas with carbon produces compounds that contain hydrogen and carbon; *i.e.*, hydrocarbons. At temperatures above 800 °C the heavy hydrocarbons (C_4 hydrocarbons or higher) are thermally unstable and their formation is thus thermodynamically unfavorable. The C_2 hydrocarbons such as ethylene and acetylene are thermodynamically much more favorable than higher hydrocarbons. Nevertheless, methane formation is by far the most thermodynamically favorable reaction at temperatures below 1000 °C [117].

But, the question of how much of these hydrocarbons are actually formed under a given set of conditions is also a kinetic question; *e.g.*, if the formation of methane is kinetically very slow and that of ethylene is very fast, the only reaction product would be small amounts of ethylene. However, it has already been shown that at temperatures below 1200 °C methane formation is also kinetically favorable; *i.e.*, methane is by far the main product detected [118-122] with very small amounts of ethane [119]. In contrast, formation of small amounts of ethane and ethylene have also been reported in the temperature

range of 600 °-880 ° C over thin films of pyrolytic carbon [123].

The hydrogen pressures in these studies have been sub-atmospheric and since the kinetics depends on the the partial pressures of reactant gases, a substantial change in the partial pressures might alter the kinetics and thus change the composition of the product gas mixture. However, for hydrogen pressures of up to 40 atm and over a temperature range of 650 °-870 ° C methane has been found to be by far the main product of hydrogasification of chars [124]. Therefore, the relative kinetics of formation of various hydrocarbons are not influenced significantly by changes in the hydrogen partial pressure.

Hence, it can be concluded that for carbon blacks, which have a graphitic structure similar to chars, methane would be by far the main product of hydrogasification below 900 ° C and hydrogen partial pressures of up to 40 atm. Therefore, the hydrogasification rate of carbon and the rate of formation of methane can be taken to be equivalent and, thus, the problem of studying the kinetics of hydrogasification is reduced to just studying the kinetics of methane formation.

4.1.2 Thermodynamic Equilibrium

The thermodynamic equilibrium of a chemical reaction determines the maximum amount of the products obtainable under the given set of conditions. That is, no matter how long a reaction is allowed to proceed, the amount of product(s) cannot exceed a certain limit which is prescribed by the thermodynamic equilibrium of that reaction. Starting a chemical reaction with no product present, if at any time there appears to be more product than what is predicted from the thermodynamic equilibrium, either the equilibrium calculations are erroneous or some other reactions are taking place as well under the given set of condition. In contrast, if for a given chemical reaction the

product concentrations (partial pressures) are less than the equilibrium values, that reaction cannot be ruled out as a formulation of chemical changes because very slow kinetics could be responsible for low concentrations. Therefore, thermodynamic equilibrium calculations cannot explain or account for all the events taking place during a chemical reaction; instead, they provide some criteria on some physical limitations of what could take place.

The thermodynamic equilibrium of carbon-hydrogen-methane has been investigated experimentally [115-117] and theoretically [127,128] over the wide temperature range of 300°-2100°C. The results have shown that the hydrogasification of carbon

$$C + 2H_2 \rightarrow CH_4 \qquad \Delta H_{25 \cdot C} = -18 \ kcal/gmole \tag{4-1}$$

is an exothermic reaction and, thus, the equilibrium concentration of methane decreases as the reaction temperature is raised (at 870°C heat of reaction ΔH is -22 kcal/g mol). For this reaction the equilibrium constant K_p is

$$K_p = \frac{p_{CH_4}}{p_{H_2}^2} \tag{4-2}$$

in accordance with the law of mass action, if it is assumed that methane and hydrogen are ideal gases and thus their fugacities are equal to their partial pressures. This assumption is valid because of the nonpolar nature of both hydrogen and methane and the high reaction temperature, and, furthermore, the high pressure of hydrogen (up to 200 atm) has been shown to have no effect on the value of K_p at a given temperature [125]. In the above equation, p_{CH_4} and

p_{H_2} are the partial pressures of methane and hydrogen, respectively. The equilibrium constant K_p is normally evaluated from the heat of reaction ΔH by the so called *van't Hoff equation* [129];

$$\frac{d\ \ln K_p}{d\ T_{rxn}} = \frac{\Delta H}{R T_{rxn}^2} \tag{4-3}$$

where R is the universal gas constant and T_{rxn} is the reaction temperature.

The temperature dependence of ΔH is calculated from the specific heat capacity C_p data of the reaction components at various temperature [129]:

$$\Delta H_{T_{rxn}} = \Delta H_{25\,^\circ C} + \int_{298\,^\circ K}^{T_{rxn}} \Delta C_p\ dT \tag{4-4}$$

with

$$\Delta C_p = \sum_i \nu_i C_{p,i} \tag{4-5}$$

where ν_i is the stoichiometric coefficient of the ith component of the reaction and $C_{p,i}$ is its specific heat capacity. The heat capacity data for methane, hydrogen and graphite are readily available in the literature [130] and substitution of these data into the above equations yields

$$\ln K_p \mid_{T_{rxn}} = 28.46 + \frac{7365}{T_{rxn}} - 5.42 \ln T_{rxn} + 0.00181 T_{rxn} + 2.65 \times 10^{-7} T_{rxn}^2 \quad (4\text{-}6)$$

$$- 1.1 \times 10^{-10} T_{rxn}^3 + \frac{29440}{T_{rxn}^2}$$

where T_{rxn} is in Kelvin and K_p is in psi.

The fraction x_{eq} of hydrogen converted to methane at equilibrium is calculated from Equation 4-2 by first computing the mole fraction of methane y_{CH_4} in terms of x_{eq} by a complete mass balance

$$y_{CH_4} = \frac{1}{1 + 2\left(\frac{1}{x_{eq}} - 1\right)} \quad (4\text{-}7)$$

Substituting mole fraction times total pressure for the partial pressure of each gas into Equation 4-2 and solving for x_{eq} (assuming that only hydrogen and methane exist in the gas phase; *i.e.* , no other hydrocarbon or inert gases exist in the reactor) yields;

$$x_{eq} = 1 - \sqrt{\frac{1}{4pK_p + 1}} \quad (4\text{-}8)$$

This equation clearly shows that the equilibrium concentration of methane depends on the value of K_p which in turn depends on the kind of carbon used.

At 870 ° C and 500 psi inlet hydrogen pressure (total reaction pressure p) x_{eq} and y_{CH_4} are equal to 0.53 and 0.36, respectively. That is, if the hydrogasification reaction is allowed to achieve equilibrium under above

conditions, 36% of the reactor effluent gas stream would be methane.

However, these values are based on the calculations for graphite (data for C_p and $\Delta H_{25 \cdot C}$ are for graphite), and it has been shown that the value of the equilibrium constant K_p depends on the type of the carbon used [125,126,131]. These studies, nevertheless, have indicated that the equilibrium concentration of methane is the lowest in the presence of graphite. Thus, as long as the methane concentration in the reactor effluent gas stream is much below the above concentration of methane, the hydrogasification reaction is far away from equilibrium and the reaction kinetics can be studied (provided, of course, that there is not significant mass transfer resistance within the carbon fixed bed).

4.1.3 Kinetics

While the thermodynamic equilibrium sets the maximum possible conversion of the reactants in a chemical reaction under a given set of conditions, the kinetics of that reaction demonstrate how fast that maximum possible conversion is reached under those conditions. Kinetic expressions can be derived either empirically or from a proposed plausible mechanism for that reaction.

For hydrogasification of chars, Blackwood [124] proposed an empirical first order kinetic expression for pressures up to 40 atm, temperatures of 650°-870° C and under the conditions far from the equilibrium (*i.e.*, in the presence of very small amounts of methane);

$$R_{CH_4} = k_{CH_4} p_{H_2} \tag{4-9}$$

where k_{CH_4} is the reaction constant and R_{CH_4} is the rate of formation of

methane per unit mass carbon. This expression does not give any indication of the mechanism, nor does it readily suggest how the equilibrium relationship would appear in a general rate expression. For instance, at equilibrium where the reaction rate is zero this rate expression predicts a definite reaction rate. A true rate expression should predict the equilibrium condition and illustrate how the reaction rate varies as the equilibrium is approached.

Several mechanisms [132-135] have been proposed (discussed in Section 4.1.4) and some kinetic expressions have been derived from these mechanisms. Zielke & Gorin [132] suggested the following expression

$$R_{CH_4} = \frac{a p_{H_2}^2}{1 + b p_{H_2}} \tag{4-10}$$

which reduces to Equation 4-9 at high hydrogen pressures (a and b are constants). This expression, however, does not accommodate the influence of methane concentration on the reaction rate. This effect is significant for near the equilibrium conditions, and thus this expression fails to illustrate how the equilibrium is approached.

Blackwood [133] obtained a kinetic expression which incorporates the influence of methane concentration as well and, thus, satisfies the equilibrium requirements and predicts a zero order reaction in hydrogen at high hydrogen pressures. Further studies by Blackwood [134] and the reinterpretation of Blackwood's experimental results by Shaw [135] lead to a slightly different expression;

$$R_{CH_4} = \frac{k_1 p_{H_2}^2 - k_2 p_{CH_4}}{1 + k_3 p_{H_2} + k_4 p_{CH_4}} \tag{4-11}$$

where k_1, k_2, k_3 and k_4 are constants related to the specific rate constants of the elementary reaction steps in the proposed mechanism. The assumption made in deriving the above expression is that in the proposed mechanism (see reactions 4-15 and 4-16), the concentration of intermediate species reaches a steady state value. At low methane concentrations and high hydrogen pressures this expression again reduces to Equation 4-9.

4.1.4 Mechanism

Zielke & Gorin [132] have proposed a mechanism based on the hydrogenation of the exposed edges of the graphitic carbon layers as an example of a "reasonable" mechanism to explain their experimental observations;

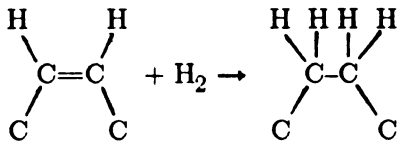
(4-12)

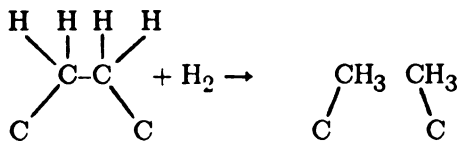
(4-13)

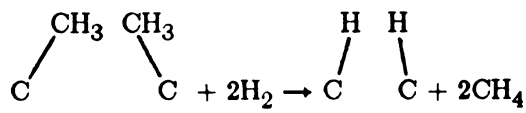
(4-14)

In this mechanism, on the average, an active site is generated for each one that is consumed. The kinetic expression 4.10 is derived from this mechanism by assuming that the intermediate product of the first step (Equation 4-12) is at a steady state and that the last reaction is much faster than the other steps.

In contrast, Blackwood [134] and Shaw [135] have suggested the following two step mechanism:

$$C + H_2 \rightarrow (CH_2) \tag{4-15}$$

$$(CH_2) + H_2 \rightarrow CH_4 \tag{4-16}$$

where (CH_2) is a surface complex which is formed by the chemisorption of hydrogen. If the surface concentration of this (CH_2) intermediate species is assumed to establish a steady state value, the kinetic expression 4.11 would be obtained.

None of these mechanisms, however, consider the possibility of the formation of products intermediate (for instance, C_2 hydrocarbons) to the formation of methane. Cao & Back [123] have modified the mechanism proposed by Zielke & Gorin to allow the intermediate formation of ethylene and ethane:

$$(CH) + H_2 \rightarrow (CH_2) + H \tag{4-17}$$

$$(CH_2) + H_2 \rightarrow (CH_3) + H \tag{4-18}$$

$$(CH_2) + (CH_2) \rightarrow (C_2H_4) \rightarrow C_2H_4 \tag{4-19}$$

$$(CH_3) + H_2 \rightarrow CH_4 + H \tag{4-20}$$

$$(CH_3) + (CH_3) \rightarrow (C_2H_6) \rightarrow C_2H_6 \qquad (4\text{-}21)$$

According to this scheme ethylene, ethane and methane are all primary products distribution of which depends on the competition between abstraction from hydrogen or dimerization of the intermediate radicals which have a degree of mobility on the carbon surface. Their experimental results led to the conclusion that at high temperatures ethane and ethylene undergo secondary reactions in the gas phase to form free radicals which eventually convert to methane.

4.2 Intrinsic Nature of Reaction Rates

The samples holders (Section 2.10) are mounted at the end of the exit tube positioned at the center of the reactor vessel and, thus, the carbon samples in these boats could experience different temperatures because they are positioned at different locations inside the reactor. The effect of this temperature variation and the depth of the carbon bed were examined to ascertain that the rate measurements are free from any masking effects due to temperature variations and mass transfer resistances.

4.2.1 Mass Transfer Resistances

The magnitude of the mass transfer resistances during hydrogasification of carbon black at 865 °C and 500 psi hydrogen gas was studies by measuring the reaction rates of a 75 mg and a 260 mg carbon sample, distributed evenly in the quartz sample holder. It is evident from Figure 4.1 that the depth of the carbon bed had no effect on the measured reaction rates; the rates are essentially the same. Therefore, for small sample sizes of carbon, 30-80 mg, (which had a

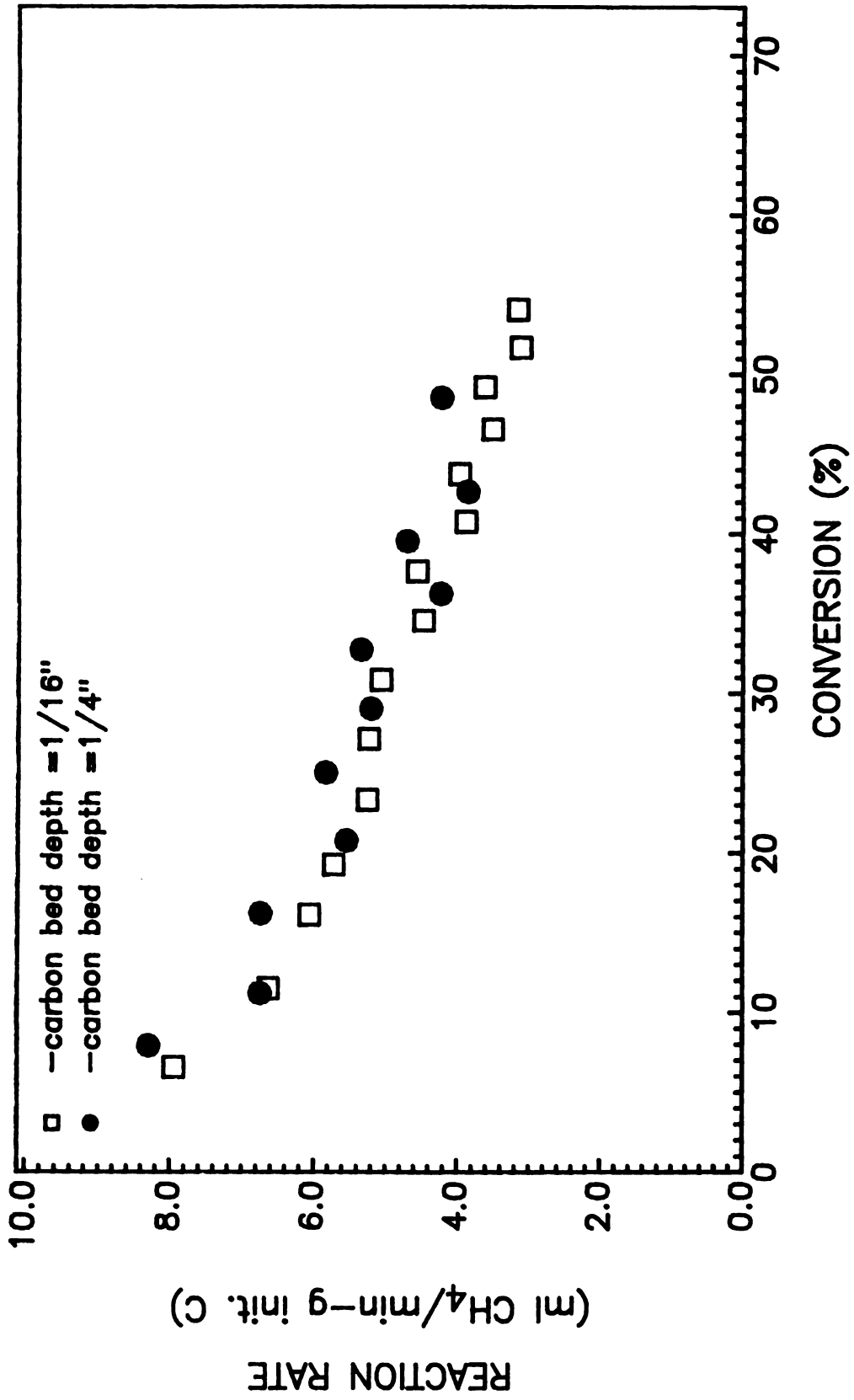

Figure 4.1 Mass transfer resistances during hydrogasification of Raven 16 at 865 °C and 500 psig.

typical bed thickness of ~1/8") mass transfer resistances within the carbon fixed bed are absent.

Another piece of evidence for the absence of mass transfer limitations is the magnitude of the activation energy E_a (Figure 4.2). E_a was evaluated by assuming a simple rate expression of some order in hydrogen concentration; *e.g.* Equation 4-9. This assumption is justified by the fact that methane concentration is very small. The value of the activation energy calculated over a temperature range of 800°-900° C was reported to be 63 kcal/g mole which is in direct contrast to a value of about 30 kcal/g-mole reported by Gardner *et al.* [38]. If the reaction rates were limited by external mass transfer (*i.e.*, by diffusion of reactant gases to the outside surface of the carbon bed), the observed activation energy would have had a typical value of 1-2 kcal/g-mole [136]. Obviously, this is not the case, because the measured activation energy is one order of magnitude higher.

In contrast, if diffusion inside the carbon bed were significant, the measured activation energy could have a value as low as one-half of the intrinsic activation energy depending on the severity of the diffusion limitations [137]. In this case, as the reaction temperature is raised and the reaction rates become faster the diffusion limitations become more important and thus the magnitude of apparent activation energy decreases. That is, the Arrhenius plot would not yield a straight line. Again, this does not appear to be the case, as evident from Figure 4.2. However, this point is studied further from a theoretical point of view.

The effectiveness factor for the carbon bed was calculated by first calculating the Thiele modulus ϕ [138] which is defined as

$$\phi = \frac{R_h}{3} \sqrt{\frac{k_{rxn}^1}{D_e}} \tag{4-22}$$

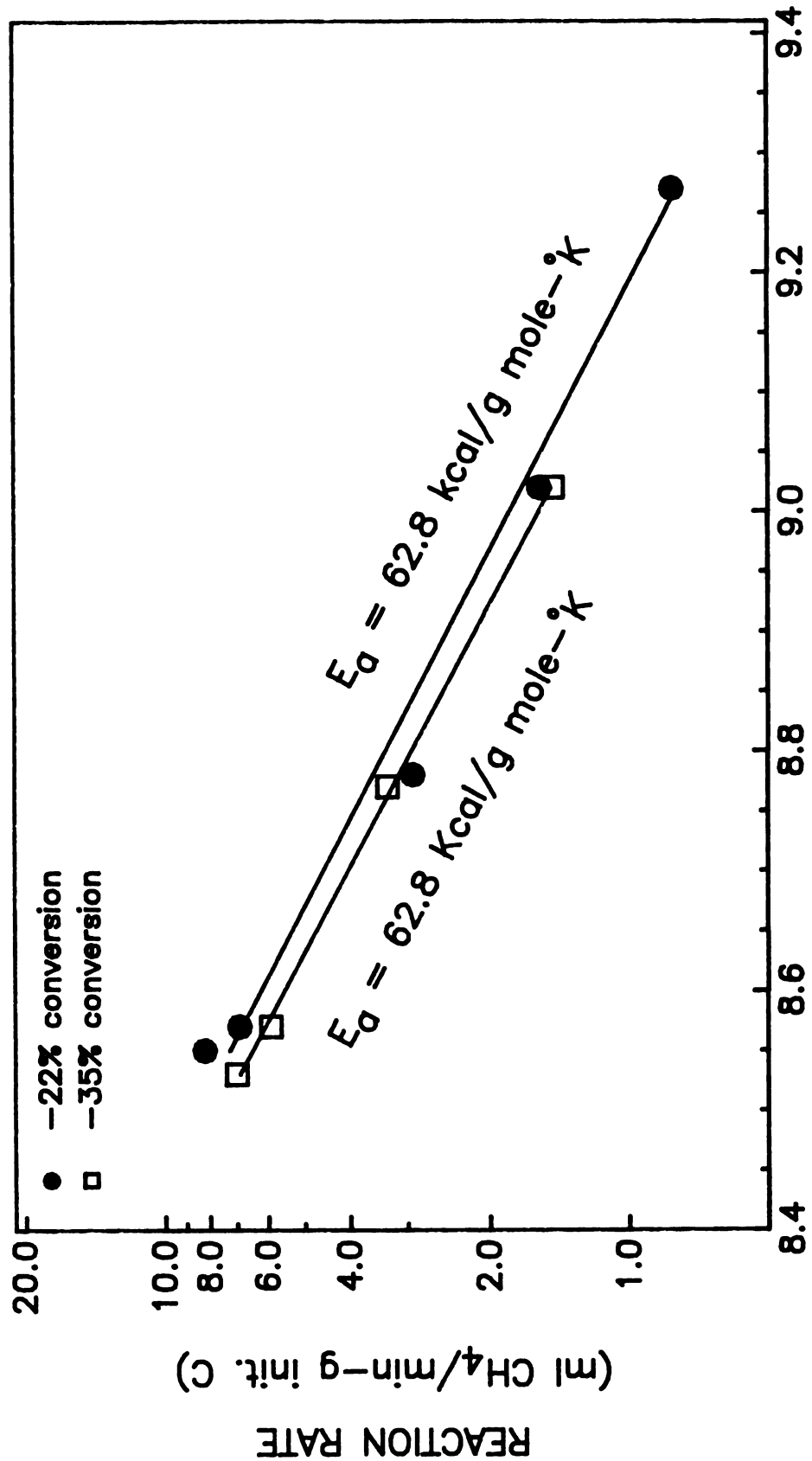

Figure 4.2 Arrhenius plot of hydrogasification of Raven 16 at 500 psig H_2.

for a heterogeneous reaction with first order kinetics such as the hydrogasification reaction (see Section 4.1.3)

$$R_{rxn} = k^1_{rxn} C_A \tag{4-23}$$

where C_A is the molar concentration of reactant A, k^1_{rxn} is the rate constant, R_{rxn} is the reaction rate, and R_h is the hydraulic radius defined as three times the ratio of volume to external surface area. The measured reaction rates presented in Figures 4.1 and 4.3 are less than 10 ml CH_4/min-g initial carbon, or 8.18×10^{-4} mole H_2/min-g carbon. The density of the carbon black particles used is 1.9 g/ml [139] and the bed porosity of fresh carbon was measured to be 80% and assuming a bed porosity of 90% at higher conversions (due to the development of porosity, see Section 3.3.3) a value of 0.19 g carbon/ml for the bulk density of the carbon bed is obtained. Thus the reaction rate R_{rxn} at most reaches a value of 2.59×10^{-6} mole H_2/sec-ml. At 865 °C and 500 psi hydrogen pressure the concentration of hydrogen gas is 3.64×10^{-4} mole H_2/ml. Substitution of these values into Equation 4-23 yields a value of 7.12×10^{-3} sec^{-1} for k^1_{rxn}.

The experimental diffusion coefficient D_{AB} of the binary system of H_2-CH_4 at 1 atm has been reported to be 0.625 cm^2/sec at 0.0 °C [140] and 0.726 cm^2/sec at 25 °C [141]. At 865 °C and 500 psi hydrogen pressure D_{AB} is calculated from the lowest of the above two values to be 0.156 cm^2/sec using the following conservative relation [142] for temperature and pressure dependence of D_{AB}

$$D_{AB} \propto \frac{T_{rxn}^{1.5}}{p} \tag{4-24}$$

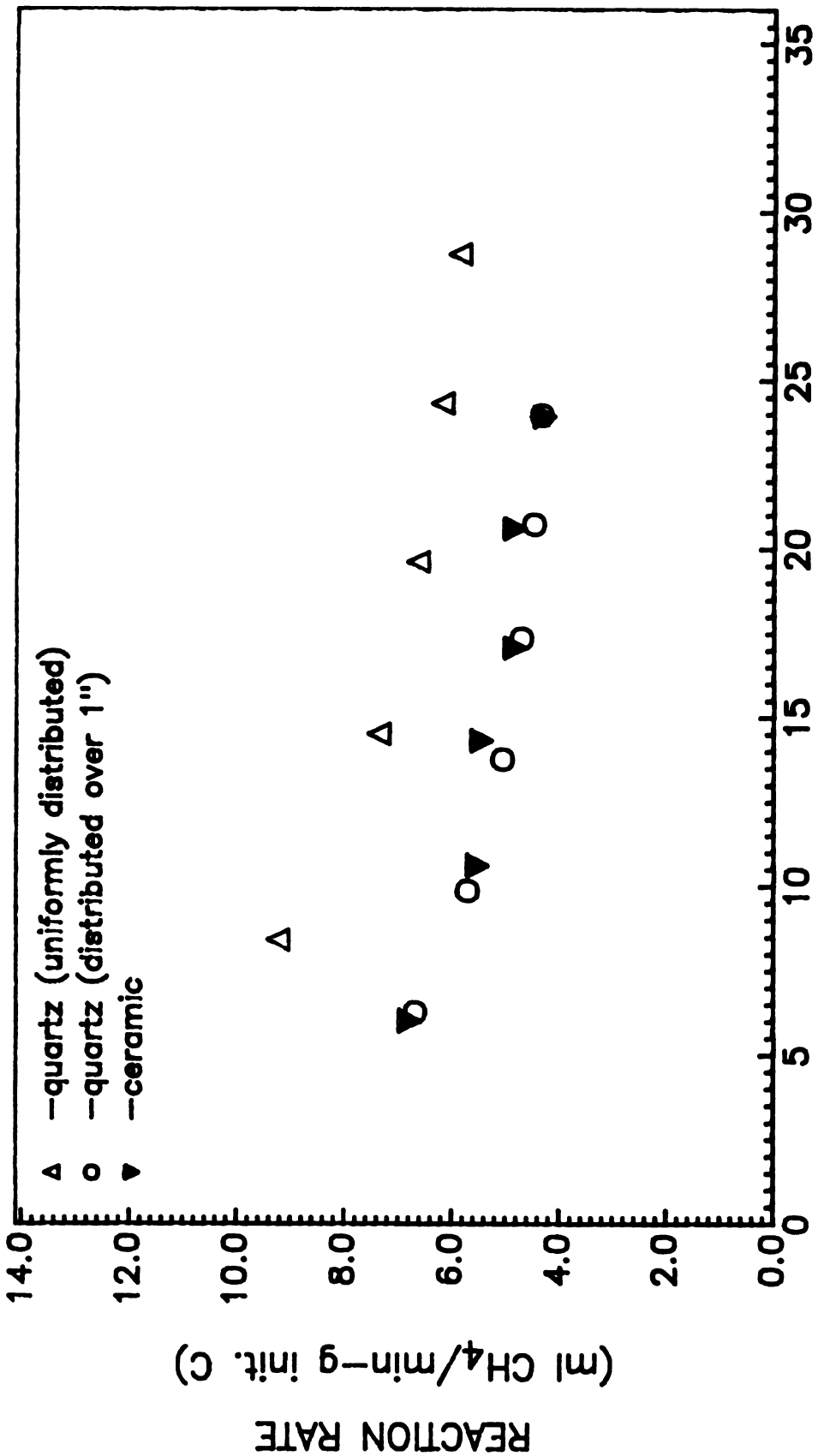

Figure 4.3 Effect of Raven 16 bed configuration on hydrogasification rate at 865 °C and 500 psig H_2.

The effective diffusivity D_e is related to D_{AB} according to the following relation [143]

$$D_e = \frac{\epsilon_p}{\tau_t} D_{AB} \tag{4-25}$$

Where ϵ_p is the porosity or void fraction and τ_t is the tortuosity factor of the carbon bed. Since the unit of D_e is based on unit cross sectional area of carbon bed, and not unit cross sectional area of the pores in carbon bed, the porosity ϵ_p which is a measure of how much of a unit cross sectional area of carbon bed is available for gas diffusion is introduced, and is taken to be 0.9. In addition, the rate of diffusion into the carbon bed is measured perpendicular to the surface of carbon bed, whereas the molecules diffuse along the direction of the carbon bed pores which, in general, are at an angle with the perpendicular direction. As a consequence, the diffusion rate in the perpendicular direction is lower than that in the direction of the pores. The tortuosity factor τ_t is introduced to account for the effect of difference in the directions of the pores and the perpendicular direction. There is no experimental value available for τ_t; however, for loose powders and beds of glass spheres having bed porosities of 0.35 to 0.43 tortuosity values of 1.4 to 1.6 are reported [143]. For a bed of fresh carbon the value of τ_t is expected to be even less because the value of τ_t is known to decrease with an increase in porosity. But, the development of porosity during hydrogasification tends to complicate evaluation of a value for τ_t since the carbon particles cannot be treated as spheres any more. The reported values for τ_t of various porous catalyst supports with various degrees of porosity are less than 10 and typical values of 2-6 are recommended [143]. Hence, a value of 10 seems to be a rather conservative estimate for the tortuosity factor τ_t of the

carbon bed during hydrogasification. Substitution of these values into Equation 4-25 yields a value of 0.0140 cm^2/sec for D_e.

The hydraulic radius R_h of the carbon bed is calculated by treating the carbon bed as a half cylinder of 1/8" radius. For the carbon bed in ceramic tube the value of R_h is then 0.748 cm.

Substitution of appropriate values into Equation 4-22 yields a value of 0.178 for the Thiele modulus ϕ. The corresponding effectiveness factor for a first order reaction, for the case of low concentration of products and a stoichiometric ratio of products to reactants of 1 to 2, is virtually 1.0 [138], indicating that diffusion limitations are not dominant. It should be noted that the assumptions made in calculating ϕ are rather conservative and the actual value of ϕ is most likely lower for the value τ_t is lower. Therefore, the reaction rates can still be faster and not be influenced appreciably by diffusion resistances, implying that the measured reaction rates are indeed the intrinsic reaction rates.

When large carbon samples (1.5 g) are used in the quartz tube, the hydraulic radius R_h of the carbon bed is 5.40 cm which makes the ϕ rise to 1.3. The corresponding effectiveness factor is about 0.75, indicating that internal diffusion resistances are not negligible. This result was verified experimentally; the conversion versus time behavior of these large samples were identical to those of small samples in the ceramic sample holders. The temperatures of the large samples are higher at some parts closer to the reactor wall and thus the reaction rates are higher (see Section 4.2.2 and Figure 4.1). But the observed overall reaction rates showed no enhancement, pointing to the fact that there were some mass transfer resistances present.

The above analysis focused on the mass transfer resistances in the carbon bed, *i.e.*, the voids among the carbon black particles and not inside the particles. As discussed earlier (Section 3.3.3), as hydrogasification reaction

proceeds, some degree of porosity is developed inside the carbon particles and, thus, the diffusion resistances inside these pores need to be considered. For a complete and accurate evaluation of these resistances, however, a knowledge of the pore size distribution is essential. The pore sizes would determine whether the diffusion is in the domain of Knudsen diffusion or it is a bulk diffusion.

No attempt was made to determine the pore size distribution; instead, the diffusion resistances are analyzed for Knudsen domain since Knudsen diffusion coefficients are typically one order of magnitude lower than the bulk diffusion coefficients. This would reveal the highest possible resistances to methane molecules diffusing out of the individual carbon black particles.

The Knudsen diffusion coefficient is calculated from the following equations

$$D_K = 9700 r_e \sqrt{\frac{T_{rxn}}{W}} \tag{4-26}$$

$$r_e = \frac{2\epsilon_c}{\rho S} \tag{4-27}$$

where r_e is mean pore radius, S is the total surface area of carbon particles, T_{rxn} is the temperature of carbon particle, W is the molecular weight of the diffusing gas, ϵ_c is the porosity of a carbon particle, and ρ is the bulk density of a carbon particle. The mean pore radius r_e defined in Equation 4-27 is in fact an empirical factor which is introduced because the internal geometries of the pores are not known. The carbon black particles have densities of 1.9 g/cm^3 [139], and at 50% conversion the measured BET surface area is 350 m^2/g (Figure 3.1) and ϵ_c has a value of 0.5. Substitution of these values into Equation 4-27

yields a mean pore radius of 15 Å. For a reaction temperature of 865 ° C, the Knudsen diffusion coefficient for hydrogen and methane calculated from Equation 4-26 is 0.0347 cm^2/sec and 0.0123 cm^2/sec, respectively.

Carbon black particles have a mean diameter of 700 Å (Section 3.3) and the corresponding hydraulic radius is 350 Å. Substitution of the Knudsen diffusion coefficient for methane, a porosity of 0.5 (at 50% conversion) and a tortuosity factor of 10 for the pore systems inside the carbon particles into Equation 4-25 yields an effective diffusivity of 6.15×10^{-4} cm^2/sec. The corresponding Thiele modulus calculated from Equation 4-22 is 4.0×10^{-6} which implies that mass transfer resistances during hydrogasification inside the carbon particles are virtually non-existent.

4.2.2 Temperature Variation of Carbon Bed

As discussed earlier, a given carbon sample might have different reactivity in the ceramic than in the quartz sample holder because of the temperature variation in the carbon bed. When the furnace temperature is set at 900 ° C, the thermocouples inserted at the center of the reactor at the inlet of the central exit tube register temperatures of 865±2 ° C, indicating a temperature difference between the reactor wall and the sample holder in the reactor. The heating of the carbon bed is achieved by radiation from the reactor wall and, thus, the closer a sample to the wall the higher its temperature. The quartz sample holder is much longer than the ceramic sample holder, and once inserted inside the reactor, its end would be much closer to the wall. This implies that the carbon particles near that end would have much higher reaction rates; for instance, if the carbon particles at this end were at 880 ° C instead of 865 ° C, their reaction rates would be 1.44 times higher, if $E_a =$ 63 kcal/g-mole (Figure 4.2). The average reaction rates, however, would be less than 1.44 higher because not all of

the carbon particles are located at that end.

The results presented in Figure 4.3 demonstrate this point clearly; when the carbon sample in the quartz tube is confined to only 1" of the boat to resemble the sample configuration in the ceramic boat, the reaction rates are virtually the same; but, when the sample is distributed evenly in the quartz boat, the reaction rates are much higher than the samples in the ceramic boat. The increase in reaction rate is more than 1.44 times, suggesting that the reactor wall temperature is higher than 880 ° C. If the reactor wall temperature is 900 ° C and the temperature of the carbon bed is assumed to vary linearly from 865 ° C at the end mounted on the exit tube to 900 ° C at the end which is almost touching the flat end of the reactor, the average reaction rate would be expected to be 1.57 times higher. Therefore, the sole temperature difference in the carbon bed can account for the observed difference in the reaction rates.

It, thus, can be concluded that the temperature variations inside the carbon fixed bed could be significant and they should be avoided in the experiments data which are to be compared.

4.3 Hydrogasification of Carbon Black

4.3.1 Procedure

To study the effect of presence of oxygen complexes on the carbon surface, samples were treated by degassing and oxygen chemisorption prior to hydrogasification. Degassing and gasification as well as oxygen chemisorption were carried out in sequential combinations in the reactor to avoid the exposure of the sample to air between steps. Degassing of the carbon samples was carried out by raising the temperature to 1000 ° C, holding for about 15 hours, and then

cooling to the desired temperature, all under vacuum (1-10 μ Hg).

Oxygen chemisorption was carried out at either 400 ° C or 800 ° C. The temperature was first raised to the desired chemisorption temperature under vacuum. About 0.33 cc (STP) O_2 gas per milligram of carbon sample was introduced into the reactor, which was then isolated. After oxidation (two hours at 800 ° C or 12-15 hours at 400 ° C) the reactor was evacuated and the next step was carried out.

Gasification procedure depended on whether or not it was preceded by degassing and/or oxygen chemisorption. For a fresh sample of carbon, the temperature was first raised from room temperature to 450 ° C under vacuum in about 45 minutes. The reactor was then pressurized with hydrogen gas to 500 psi, and the temperature was increased to the steady state value of 865 ° C in an additional 50 minutes. At the end of gasification, the reactor was evacuated and was either cooled to room temperature or to the temperature of the next step.

When oxygen chemisorption at 400 ° C preceded the gasification, the same gasification procedure was adapted. In the case of oxygen chemisorption at 800 ° C, the reactor was evacuated after chemisorption, hydrogen gas was introduced, and the temperature was raised to 865 ° C in 20 min. When gasification was preceded by degassing, the temperature was lowered to 800 ° C after degassing and the above procedure was used.

For all hydrogasification and oxygen chemisorption experiments Linde UHP or Airco grade 5 (99.999% pure) hydrogen gas and Airco grade 2.6 oxygen gas were used. The hydrogen gas (which was further purified by passage through a 3A molecular sieve trap, see Section 2.6) flow rate used was 310±10 ml/min.

4.3.2 Results

A set of raw reaction rate data (reaction rate versus time) for hydrogasification of fresh carbon (as-received carbon black) is presented in Figure 4.4. The start of experiment (time = 0) was taken as the time hydrogen flow was begun at 450 ° C. The reaction rate increased as reaction temperature was increased, reaching steady steady after 50 minutes. In this particular experiment and all other experiments, carbon conversion was less than 10% when the steady state temperature was reached. Furthermore, in all cases the total conversion of carbon as calculated from integration of the raw reaction rate data was close to the conversion determined by weighing the residual carbon samples after experiments, showing that all methane was accounted for. The experimental results were also fairly reproducible, as some duplicate experiments in Figures 4.6 and 4.7 indicate.

The manipulated kinetic results (reaction rate versus conversion) of carbon black, fresh or after degassing, with or without oxygen chemisorption, at 400 ° C and 800 ° C, are presented in Figures 4.5 through 4.8. In all cases, except for the degassed samples, methane evolution rate decreased at steady state temperature as carbon was consumed (Figures 4.5-4.7). Degassed carbon black, on the other hand, showed a relatively constant reaction rate, but exhibited much less activity than the fresh carbon irrespective of the combustion treatment (Figures 4.5 and 4.8). In contrast, heating a carbon sample for 3 hours at 865 ° C in helium before gasification had no significant effect on reaction rate (Figure 4.5).

The reactivity of carbon black, fresh or degassed, toward hydrogen was consistently enhanced by oxygen chemisorption prior to gasification. Oxidation at 400 ° C enhanced the rate of methane evolution from fresh carbon considerably (by a factor of 2 at low conversions) and from degassed carbon

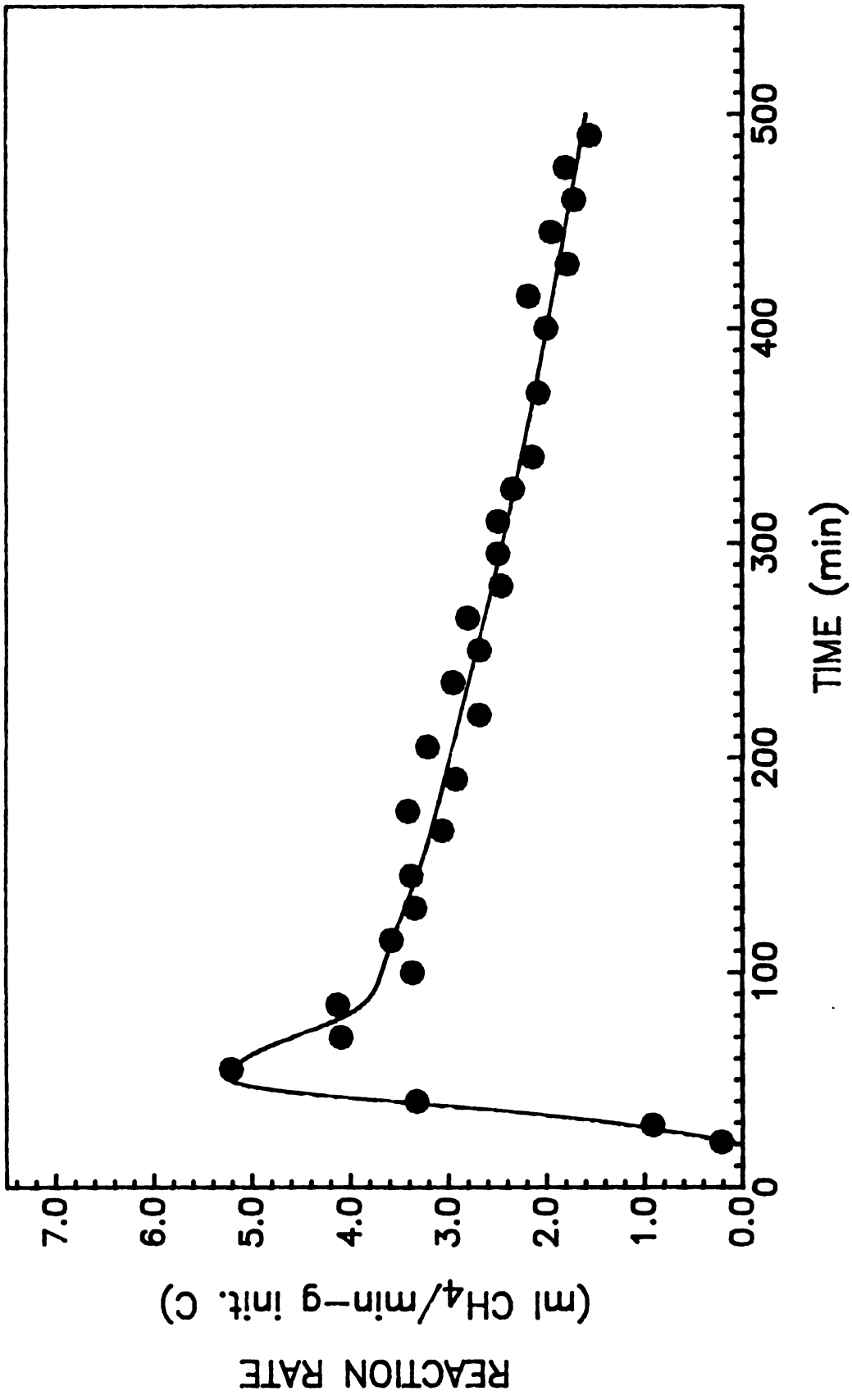

Figure 4.4 Raw hydrogasification rate data of Raven 16 at 865 °C and 500 psig H_2.

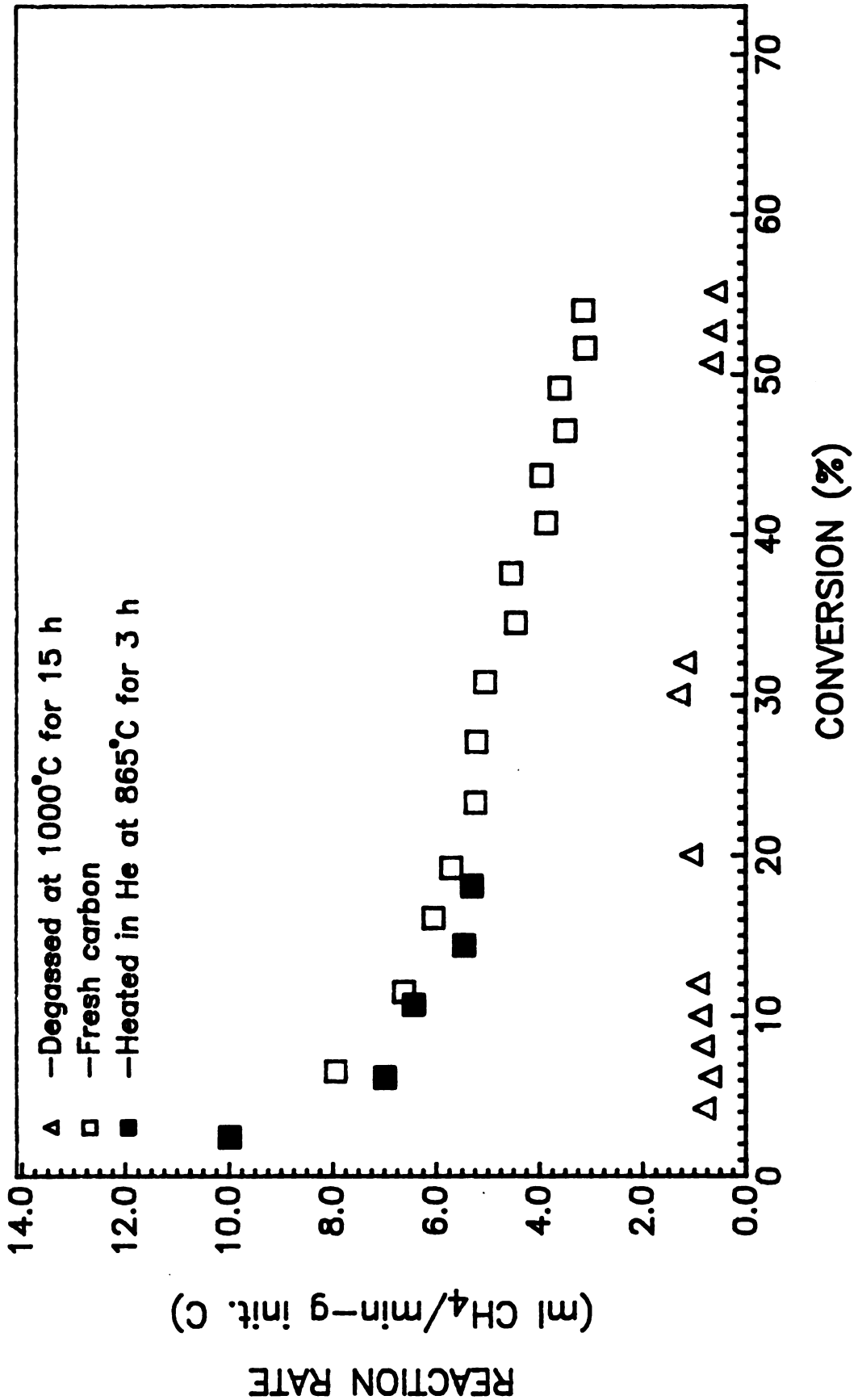

Figure 4.5 Effect of heat-treatment on hydrogasification rate of Raven 16 at 865 °C and 500 psig H_2.

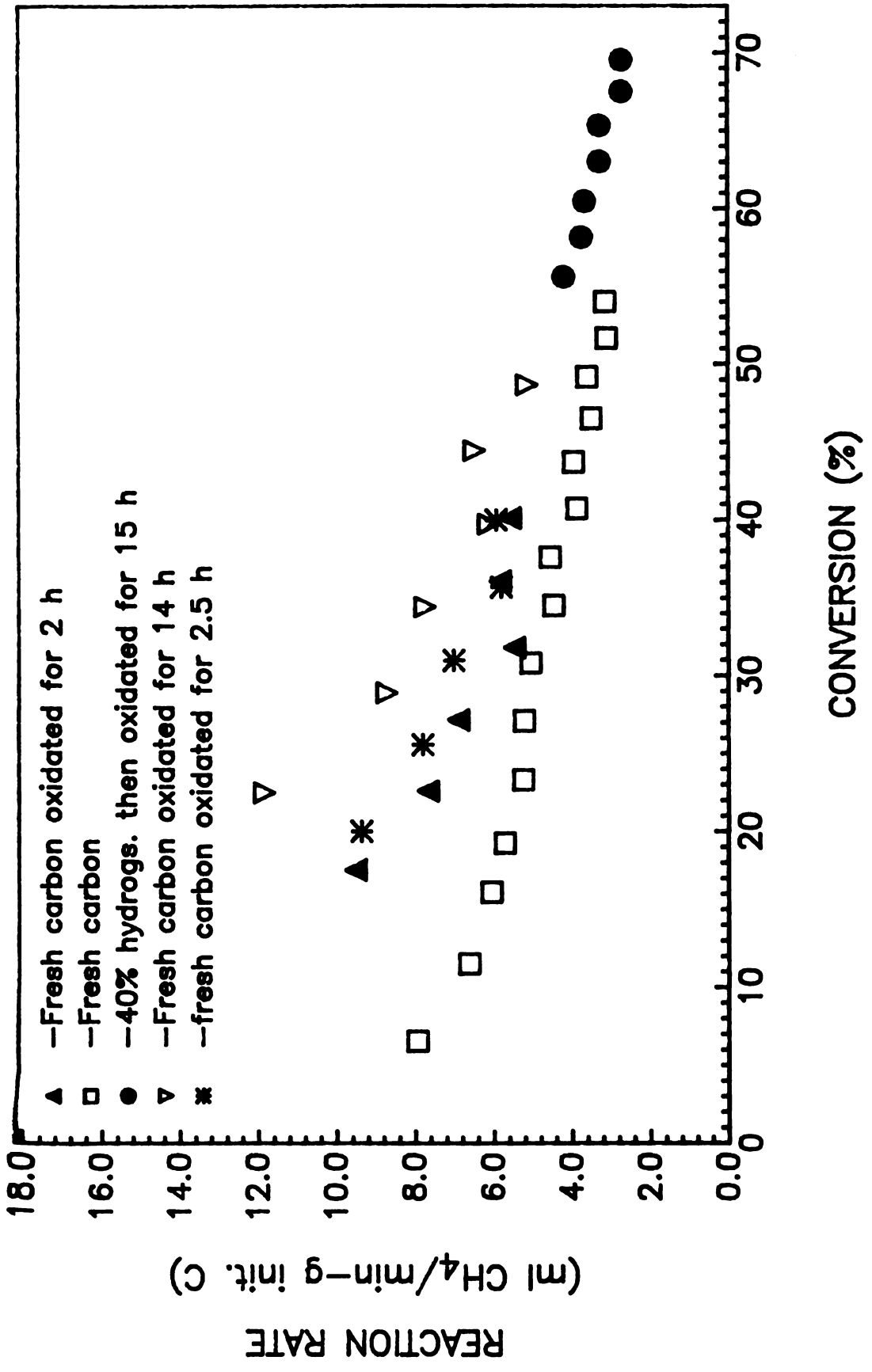

Figure 4.6 Effect of combustion at 400 °C on hydrogasification rate of Raven 16 at 865 °C and 500 psig H_2.

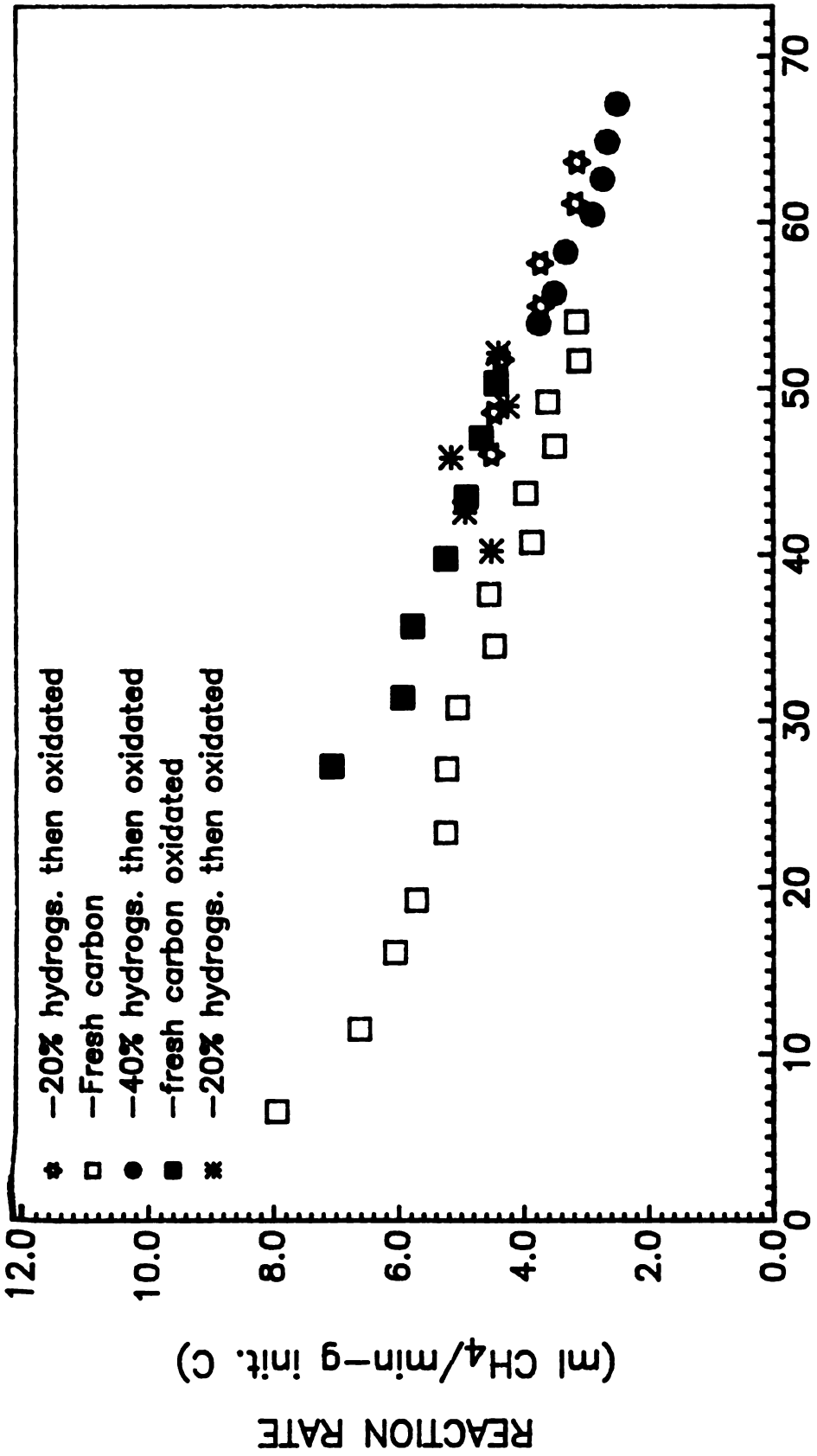

Figure 4.7 Effect of combustion at 800 °C on hydrogasification rate of Raven 16 at 865 °C and 500 psig H_2.

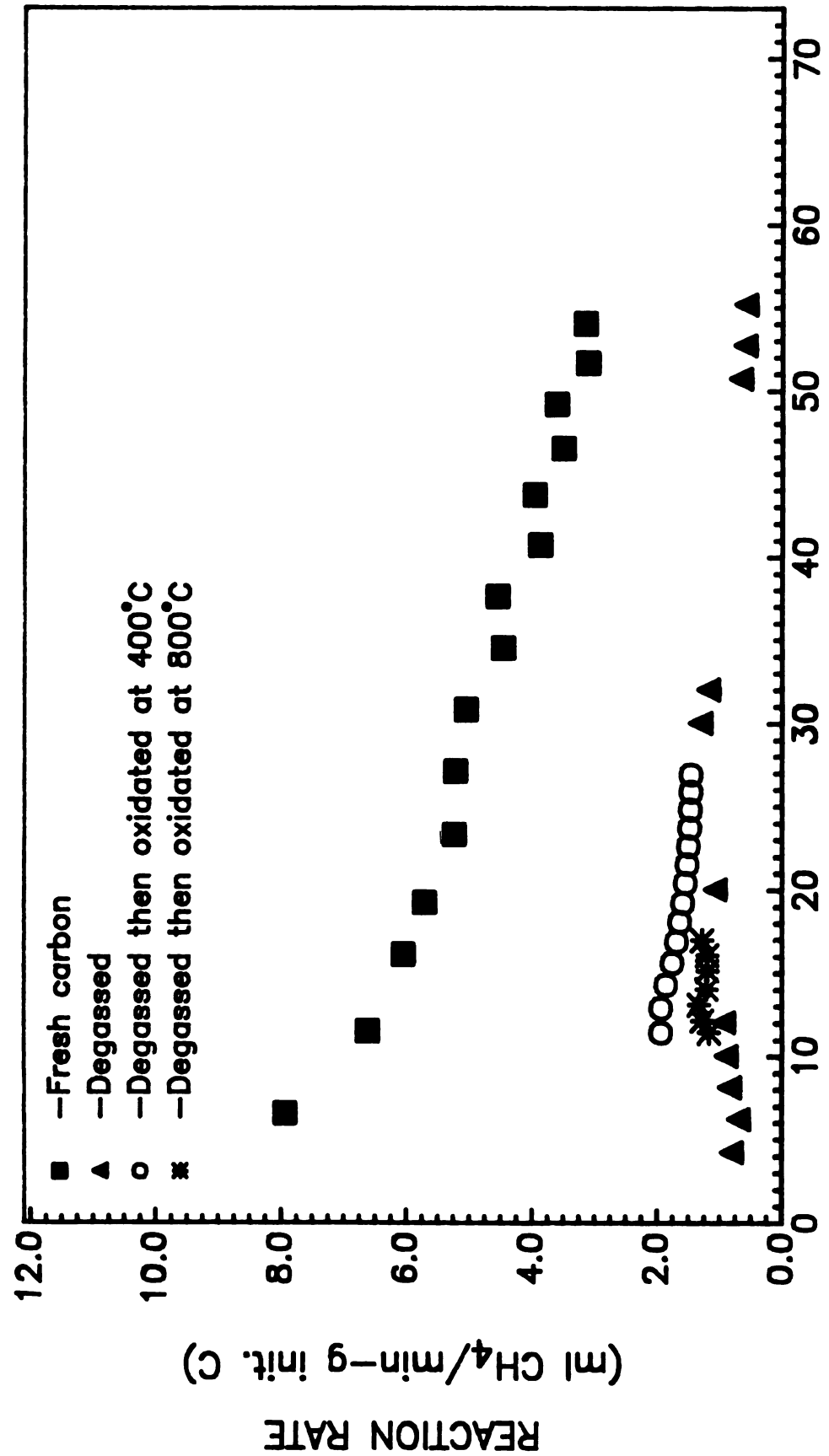

Figure 4.8 Effect of combustion on hydrogasification rate of degassed Raven 16 (1000 ° C) at 865 ° C and 500 psig H_2.

slightly (Figure 4.6). Oxidation at 800 ° C was not as effective (Figure 4.7). The oxidations were carried out at different levels of conversion by first gasifying a sample to a desired conversion, followed by chemisorbing oxygen, and then gasifying it further. It can clearly be seen that the carbon black is activated to a greater extent by oxygen at lower conversions. At higher conversions, the enhancement, although small, was consistently observed.

4.3.3 Discussion

The addition of oxygen surface groups by partial combustion enhances the reactivity of the carbon samples and is more effective at lower conversions (Figures 4.6 and 4.7). This enhancement, however, is not as high as that observed by Cao & Back, who attributed the enhancement to the oxide surface complexes formed from the oxygen present in the gas stream [39]. The formation of surface complexes requires chemisorption of the oxygen on the carbon surface and, therefore, the number of surface complexes is directly proportional to the active surface area (ASA) and not to the total surface area (TSA). The ASA of the pyrolytic carbon used by Cao & Back (which had no structure) was essentially equal to the TSA [144]; the carbon black used in this study, on the other hand, is highly graphitic and only a small fraction of the carbon atoms are located at the edge of the basal planes, where the active sites are believed to be located. Hence, relatively much less oxygen chemisorbs on this carbon, and the reactivity enhancement is expected to be much less compared to the pyrolytic carbon.

As discussed in Section 3.8.3, from pH measurement experiments it was inferred that the oxygen complexes present on and near the surface of fresh carbon are mainly C=O carbonyl groups, and the oxygen groups in the bulk of carbon are dominantly basic in character (and are not destroyed by prolonged

degassing at 1000 ° C). The oxygen groups fixed on the carbon surface via combustion at 400 ° C are acidic and at 800 ° C are non-acidic.

The rate data in Figure 4.8 shows much lower reaction rates for degassed samples, even after fixing oxygen groups on the surface by partial combustion. The possibility that the degassing temperature of 1000 ° C might have caused graphitization of the carbon, and hence lower reactivity, was ruled out because the diffraction pattern of this carbon was identical to that of the fresh carbon (see Sections 3.3.5 and 3.3.6).

The thermal desorption of oxygen surface groups into CO and CO_2 is known to produce highly reactive 'nascent' sites on the carbon surface [145,146]. The ASA generated by the decomposition of the initial oxygen surface groups has obviously been destroyed by the high temperature degassing of the carbon sample. The high temperature degassing of carbons and graphite has been reported to cause surface annealing and to change the ASA [147], resulting in much less chemisorption of oxygen and fewer active sites. The small reaction rate, following the thermal destruction of active sites, is attributed to existence of the basic oxygen groups as was suggested by Blackwood [40].

However, if the basic oxygen groups are responsible for a very small portion of the activity of the carbon, then the large activity of a fresh carbon sample must be associated with either some other oxygen complexes or some other active sites which are not related to oxygen in the carbon, or both. In the former case, these active oxygen complexes are decomposed, followed by thermal annealing of the generated active sites, or transformed into basic complexes by degassing. The basicity of the surface of a carbon sample gasified after degassing does not differ from that of a gasified fresh carbon (Table 3.4), suggesting that the transformation of other oxygen groups into basic groups is unlikely. Thus, thermal annealing of active sites seems to be responsible for the

observed large loss of the activity of a degassed carbon sample. Once these active sites are thermally destroyed, less oxygen is chemisorbed and less active sites are generated. This explains the much lower reaction rates of the degassed carbon samples even after oxidizing. At this point, however, it is not clear whether these active sites have their origin exclusively in thermal decomposition of oxygen complexes or some other sources.

The higher enhancement of reactivity observed for oxygen groups formed at 400 ° C can be attributed to their lower stability at the reaction temperature of 865 ° C. These oxygen groups decompose at temperatures higher than 750 ° C; the desorption of CO and CO_2 is known to produce highly reactive 'nascent' sites on the carbon surface [146] and these sites are postulated to act as active sites for gasification. The oxygen complexes formed at 800 ° C, on the other hand, are much more stable at this high temperature and would remain on the surface occupying the active sites. However, the reactivity is still higher than that of the fresh carbon because oxidation of the surface is known to increase the ASA [145,146] and the added ASA compensates for the active sites occupied by the oxygen complexes.

The reaction rate of the fresh carbon has been observed to be higher at the early stages of the gasification than at higher conversions (Figures 4.1, 4.5-4.8). This is attributed to the presence of C=O carbonyl groups on the surface of the fresh carbon samples. At early stages of gasification, decomposition of these carbonyl groups creates the reactive 'nascent' sites and thus enhances the reactivity of the sample. At higher conversions, these active sites are consumed or thermally annealed and less carbonyl groups are present to generate active sites. The reaction rate therefore slowly decreases.

It may be argued that high initial activity is due to the electronic effect of carbonyl groups on the carbon lattice, so that upon their slow desorption the activity also decreased slowly. If this were the case, the reaction rate would decrease after 3 hours of heating a sample at 865 °C in helium, due to both desorption of carbonyl groups and the thermal annealing of the active sites. The reaction rate of such a sample, however, showed no noticeable decrease (Figure 4.5). The desorption of oxygen surface complexes creates more active sites and the thermal annealing tends to reduce the number of the active sites. These two competing processes apparently compensate and no net effect is observed.

From the above results a mechanism for the observed enhancement of the hydrogasification rates by the surface oxygen complexes is postulated: oxygen surface groups enhance the reactivity of the carbon in hydrogen by generating active 'nascent' sites on the surface upon decomposition, not by the so called "electron-transfer" mechanism in which the chemisorbed oxygen alters the electronic state of the crystalline lattice. If the "electron-transfer" mechanism was responsible for the activation of the carbon, the enhancement would be observed only as long as oxygen was bound to the surface. However, the result presented in Figure 4.5 suggests the opposite; *i.e.*, the enhancement was observed following desorption of the surface complexes. It should be noted that this is not to say that all the active sites are exclusively associated with the oxygen groups in the carbon and that the degassing deactivation is purely an annealing process of these sites. There may very well be other active sites associated with impurities in the carbon.

Chapter 5

Catalyzed Hydrogasification

In Chapter 4, the reactivity of carbon black toward hydrogen gas and the influence of oxygen surface complexes in the absence of potassium carbonate or other catalysts were discussed. In the present chapter the effect of the presence of different amounts of K_2CO_3 and the role of oxygen surface groups in the catalysis process are discussed. This is done by first presenting the results of kinetic rate measurements and then comparing them with the results presented in Chapter 4.

5.1 Background

5.1.1 Thermodynamic Equilibrium

By definition, a catalyst is a substance that increases the rate of a reaction and can be recovered chemically unchanged at the end of the reaction [148]. The catalyst provides an alternate mechanism which is faster than the mechanism in the absence of the catalyst. The equilibrium constant for the overall reaction is, however, determined by the Gibbs free energy of the reaction, which is calculated from free energies of formation of the reactants and products, and therefore is independent of the reaction mechanism. That is, the presence of a catalyst does not change the thermodynamic equilibrium constraints of the reaction; instead it merely enhances the reaction rate.

K_2CO_3 cannot be recovered chemically unchanged, because some interactions with carbon form intermediate species (for instance, free potassium metal) which vaporize at the high reaction temperatures (see Section 5.1.3). In this respect, K_2CO_3 is not a catalyst in the traditional sense of the word. Nevertheless, the presence of K_2CO_3 on carbon enhances the methane evolution rate significantly [38], and, furthermore, methane is by far the main product, similar to the case of the uncatalyzed hydrogasification (see Section 4.1.1). Hence, it seems that the interaction of K_2CO_3 with carbon and the products thus formed (CO, CO_2, *etc.*) are not substantial enough to alter the course and the overall reaction of the hydrogasification of carbon. Instead, the interaction forms some active intermediate species which catalyze hydrogasification. Therefore, the equilibrium constant K_p assumes the same value for the catalyzed and the uncatalyzed hydrogasification of carbon.

5.1.2 Kinetics & Mechanism

The catalyzed gasification of carbon is an enormously complicated reaction, and its kinetics are too complex to allow any theoretical derivation of a kinetic expression. The major difficulty is a lack of knowledge of overall mechanisms. Even though some intermediate species (for instance, >C-O-K [12,21,22] or some non-stoichiometric potassium oxides [24,25]) have been identified, the exact sequence of event leading to formation of these species and their exact role in the overall mechanism is not fully understood. Thus, the various proposed mechanisms [12,14-30] are only in the realm of speculation.

Since the reaction rate depends on the nature of the carbon used as well as the nature and loading of the added catalyst, any empirical kinetic expressions have very limited applicability. Very few attempts have been made to study the kinetics of catalyzed hydrogasification of carbons, and probably the most detailed study of the kinetics are those by Gardner *et al.* [38]. They found a kinetic expression of 3/2 order in hydrogen for coal chars at pressures up to 1000 psi and temperatures as high as 1000 ° C in the presence of $KHCO_3$ (which had about the same activity as K_2CO_3). They also found the following relation for the activation energy E_a

$$E_a = E_a \Big|_{x=0} + 2.43x \tag{5-1}$$

In the absence of the catalysts they found

$$E_a = E_a \Big|_{x=0} - 2.43x \tag{5-2}$$

Thus the activation energy for hydrogasification of their coal char was not

affected by the presence of the catalyst at low conversions, but was reduced at higher conversions.

5.1.3 Carbon-K_2CO_3 Interaction

Potassium is not active as a catalyst in its carbonate form; active intermediates are produced via interactions of the carbonate with carbon. The extent of the interaction depends on the degree of dispersion of the carbonate on carbon surface. For instance, if carbon particles and K_2CO_3 grains are mixed mechanically so that there is a very small contact area between carbon and the carbonate, carbon-K_2CO_3 interaction and thus the activity would be minimal. The carbonate is activated substantially as long as there is a good degree of dispersion of the carbonate molecules on the carbon surface, and the impregnation method to achieve this high level of dispersion is immaterial [12]. When highly dispersed, the carbonate evenly spreads into a thin film on graphite [149] and other carbon surfaces [24,33] at temperatures as low as 550 ° C (compared to its melting point of 891 ° C) followed by reaction with carbon surface and formation of active species.

The exact nature of the intermediate species formed during interaction of the carbonate and carbon surface has been studied extensively for over a century; but still remains a point of great controversy. Roscoe & Schorlemmer [150] and Fox & White [151] have proposed the carbothermic reduction of potassium and sodium carbonates to free alkali metals and carbon monoxide at temperatures above 800 ° C

$$M_2CO_3 + 2C \rightarrow 2M + 3CO \qquad (5\text{-}3)$$

where M stands for potassium or sodium. Verra & Bell [19] have presented some

results in support of this reaction. Furthermore, McKee *et al.* [15,18] have suggested this reaction as the first and the rate controlling step of the catalysis during steam and CO_2 gasification of graphite at temperature above 700 ° C and coal and chars at above 600 ° C. Sancier [35] has also used this reaction as the first step in explaining his *in situ* e.s.r. results.

However, in some other studies in addition to the CO (Reaction 5-3) some CO_2 has been detected, the origin of which is a point of dispute. For instance, Yuh & Wolf [23] observed Reaction 5-3 for graphite at temperatures above 700 ° C, but for Illinois No. 6 coal they also detected CO_2 in the temperature range 500 ° -700 ° C and attributed this observation to the following reaction

$$Na_2CO_3 + C \longrightarrow 2Na + CO + CO_2 \qquad (5\text{-}4)$$

Freriks *et al.* [31] have shown that the decomposition temperature depends on the dispersion level of K_2CO_3 and above 700 ° C the products were CO_2 and a potassium containing surface complex the nature of which could only be speculated. In addition, Moulijn *et al.* [30,33,152] have observed, by using *in situ* FTIR technique, that at 500 ° C K_2CO_3 disappears on carbon surface and CO_2 and CO evolve. They have explained their findings by

$$K_2CO_3 \longrightarrow K_2O + CO_2 \qquad T_{rxn} < 900\ ^\circ K \qquad (5\text{-}5)$$

with further reaction of the oxide with carbon

$$K_2O + C \longrightarrow 2K + CO \qquad T_{rxn} > 900\ ^\circ K \qquad (5\text{-}6)$$

They showed, in addition, that if the contact between K_2CO_3 and carbon is poor, say because of dry mixing, no interaction is observed at temperatures below the melting point of K_2CO_3, and that part of the free alkali metal thus formed further reacts with carbon to form surface complexes which thermally decompose at above 800 ° C (no elaboration was made on the nature of these complexes). The excess free metal (above the saturation ratio K/C of 0.18 atoms of K per atom of C, or $KC_{5.5}$) evaporated readily at above 500 ° C. Huhn *et al.* [153] and Yokoyama *et al.* [154] have proven the existence of the sequence of Reactions 5-5 and 5-6 by experiments with ^{13}C-labeled K_2CO_3.

The findings of Saber *et al.* [27] are in direct contrast to Reaction 5-5. From studies with $K_2^{13}CO_3$ they concluded that below 730 ° C the evolved CO_2 does not originate from the carbonate, because the carbonate did not decompose to a large extent. Instead, any $^{13}CO_2$ evolved arises from isotope-exchange reactions. Above 730 ° C, where the carbonate did decompose substantially, they suggested that oxygen surface complexes stabilize the free metal formed via formation of surface compounds in which K/O ratio is 2, irrespective of the initial oxygen surface concentration.

Huttinger & Minges [20] support the formation of K_2O on coal (Reaction 5.5) at above 500 ° C, but ruled out the feasibility of the formation of K_2O and the free potassium metal on graphite based on thermodynamical considerations. Instead, they proposed a scheme which involves formation of KOH followed by formation of a potassium/oxygen oxide (K_xO_y with $y<x$) which they believed to be the active intermediate species. In agreement with this scheme, Wood *et al.* [24,25] inferred that the carbonate in contact with char undergoes a chemical and physical transformation to form a molten potassium oxide film that covers the char surface. Their measured equilibrium vapor pressure of free potassium metal (by Knudsen cell diffusion technique) over the temperature range of 450 ° -

700 ° C above this film was orders of magnitude below that appropriate to the carbothermic reduction of the carbonate to free metal.

Interpreted in a somewhat different direction are the studies by Mims & Pabst [155], who report CO_2 evolution following interaction of K_2CO_3 with carbon or coal at ~450 ° C. They believe that [12] the interaction of carbon with the carbonate involves bonding of potassium to surface anionic groups on carbon (phenolates being the most likely candidates) to form alkali phenolates (C-O-K complexes) and thus stablizing oxygen bonded to carbon:

$$K_2CO_3 + 2C{-}OH \rightarrow 2K^+ \; O^- \; C + H_2O + CO_2 \qquad (5\text{-}7)$$

Hoshimoto *et al.* [156] have verified the existence of these C-O-K complexes on carbon surface by FTIR technique and by showing that the amount of surface oxygen and potassium were in a 1:1 proportion.

The above studies have mostly concentrated on evaluating the individual reactions and determining the primary and secondary reactions (CO and CO_2 evolution). Very few researchers, most notably Sams *et al.* [157], have paid much attention to the kinetics of the loss of the free potassium formed via interaction with carbon surface. These researchers have observed rapid potassium loss at above 700 ° C following the reduction of the carbonate with carbon, with the vaporization rate being faster under a reducing atmosphere than that under oxidizing conditions. They have concluded that the interaction of the carbonate and carbon is a prerequisite for the potassium vaporization, and, furthermore, the gasification rate depends only on the K/C ratio (as long as it is below the saturation ratio of 0.025) and is independent of the heat treatment history of the carbon.

In diversion from the above popular schools of thought regarding the nature of active species and their formations, some researchers have speculated the involvement of potassium-carbon intercalation compounds in the catalysis process of steam and CO_2 gasifications [28,30]. Kapteijn *et al.* [158] have illustrated (using X-ray analysis) the formation of potassium-graphite intercalation compounds from mixtures of K_2CO_3 with activated carbon or coal (but not with graphite) in nitrogen at 830 °C. However, no experimental evidence has yet been provided to actually support either the formation of the intercalation compounds under gasification conditions or, more importantly, their involvement in the catalysis process.

In fact, Tromp & Cordfunke [159], by using a high temperature XRD technique, have shown that no formation of potassium-carbon intercalation compounds can be expected during K_2CO_3-catalyzed carbon gasification because they are not thermodynamically stable at gasification temperatures (680 °-880 °C). Ferguson *et al.* [160] have provided further evidence for the thermal instability of potassium-graphite intercalation compounds under gasification conditions using SEM and *in situ* XRD techniques.

From the above studies, in summary, it appears that when K_2CO_3 is highly dispersed on carbon, it spreads into a thin film at temperatures as low as 500 °C, followed by reduction to metallic potassium via interaction with carbon surface groups. The free potassium metal thus formed reacts with oxygen surface groups to form surface complexes such as C-O-K which prevent the vaporization of potassium and, hence, retain the free potassium metal on carbon surface. In an oxidizing atmosphere such as CO_2 or H_2O, where a constant supply of oxygen is available, an alkali oxide liquid layer with excess alkali metal is formed. This oxide layer reduces the vapor pressure of the alkali metal by orders of magnitude and, therefore, reduces potassium losses from the surface at

the high gasification temperatures. In reducing environments, no such oxide film can be formed and thus more potassium is lost via vaporization. Also, formation of potassium-graphite intercalation compounds seems to be highly improbable at the high gasification temperatures.

However, the mechanisms or even the nature of active intermediate species and the exact sequence of events taking place on carbon surface during gasification are yet far from being understood. In addition, although the importance of the presence of oxygen on carbon surface has been demonstrated, no attempt has yet been made to study the nature and the functionality of surface oxygen groups as related to the catalysis process. That is, it is not known whether different oxygen surface complexes (acidic, basic, *etc.*) behave similarly, or whether their influence on the catalysis depends on their nature.

5.1.4 Effect of Carbon Impurities on Reactivity

The Ravon 16 used for hydrogasification studies has various impurities such as sulfur, nitrogen and ash (see Section 3.3.1). The ash content is too small to cause any deactivation of the catalyst via formation of aluminosilicates (kaliophilite) [161-163], and other elemental impurities such as iron are too small to increase the reactivity noticeably. The nitrogen impurities also do not create any complications because they readily leave the carbon surface at high temperatures, as evident from XPS results of Section 3.3.7. The hydrogen impurities are not significant because, firstly, they are very small and, secondly, they are in the same form as the hydrogen complexes formed during hydrogasification, namely, C-H bonds. The effect of oxygen impurities will be discussed in the following Sections.

Sulfur, however, is present in substantial amounts, 1.54 wt%, and could form potassium sulfide which is not active. Sulfur exists in carbon either as highly stable C-S-C structures in which sulfur may be present in the aromatic rings of the carbon layers, or as sulfides and hydrosulfides [164]. The C-S-C structure is formed by addition to unsaturated sites and does not decompose completely even at 1200 ° C. Upon thermal decomposition this structure yields mostly carbon disulfide CS_2. The sulfide and hydrosulfide groups, on the other hand, are formed by substitution through interaction with certain oxygen groups which come off as carbon monoxide on high temperature decomposition, and are relatively unstable (start to decompose at a temperature as low as 400 ° C).

The XPS results of Section 3.3.7 indicate that samples of Raven 16 degassed at 1000 ° C or hydrogasified at 865 ° C show no trace of sulfur on their surface. It thus follows that the sulfur present in Raven 16 is not in the form of stable C-S-C structures. The sulfur impurities thermally decompose to hydrogen sulfide, H_2S, or are substituted by hydrogen to form H_2S. Any potassium sulfide, K_2S, formed during hydrogasification via reaction with the carbonate, is reduced to free potassium metal by hydrogen under reaction conditions [20]

$$K_2S + H_2 \rightarrow 2K + H_2S \qquad (5\text{-}8)$$

Therefore, the presence of sulfur does not interfere with the activity of K_2CO_3.

5.2 Intrinsic Nature of Reaction Rates

For kinetic studies of catalyzed hydrogasification, a ceramic boat (described fully in Section 2.10) was used. This sample holder was not deep enough for the carbon samples to exhibited any mass transfer limitations within the carbon bed during the uncatalyzed hydrogasification reactions (Section 4.2.1). However, in the case of catalyzed hydrogasification, where the reaction rates are much faster, the mass transfer resistances might become significant, and thus diffusion limitations need to be examined. The temperature variation of carbon bed associated with using sample holders of different geometries and configurations (see Section 4.2.2) is absent because only one type of sample holder is used for these studies.

5.2.1 Mass Transfer Resistances

Typical sets of raw data of methane evolution rate versus time for fresh carbon as well as carbon samples impregnated with K_2CO_3 to 5 wt% and 10 wt% are presented in Figure 5.1. The maximum measured rate of the 10 wt%-sample is about 30 ml CH_4/min-g initial carbon which is three times faster than the methane evolution rate used for the analysis of diffusion limitations in Section 4.2.1. Similar analysis would predict the magnitude of mass transfer resistances during hydrogasification of the impregnated samples. However, a few assumptions must be made because of the presence of the catalyst in the carbon bed. The first assumption is that the porosity development during the hydrogasification (see Section 3.3.3) is not altered by the presence of the catalyst. This assumption is justified by the observation that the surface area development is not altered by the presence of the catalyst.

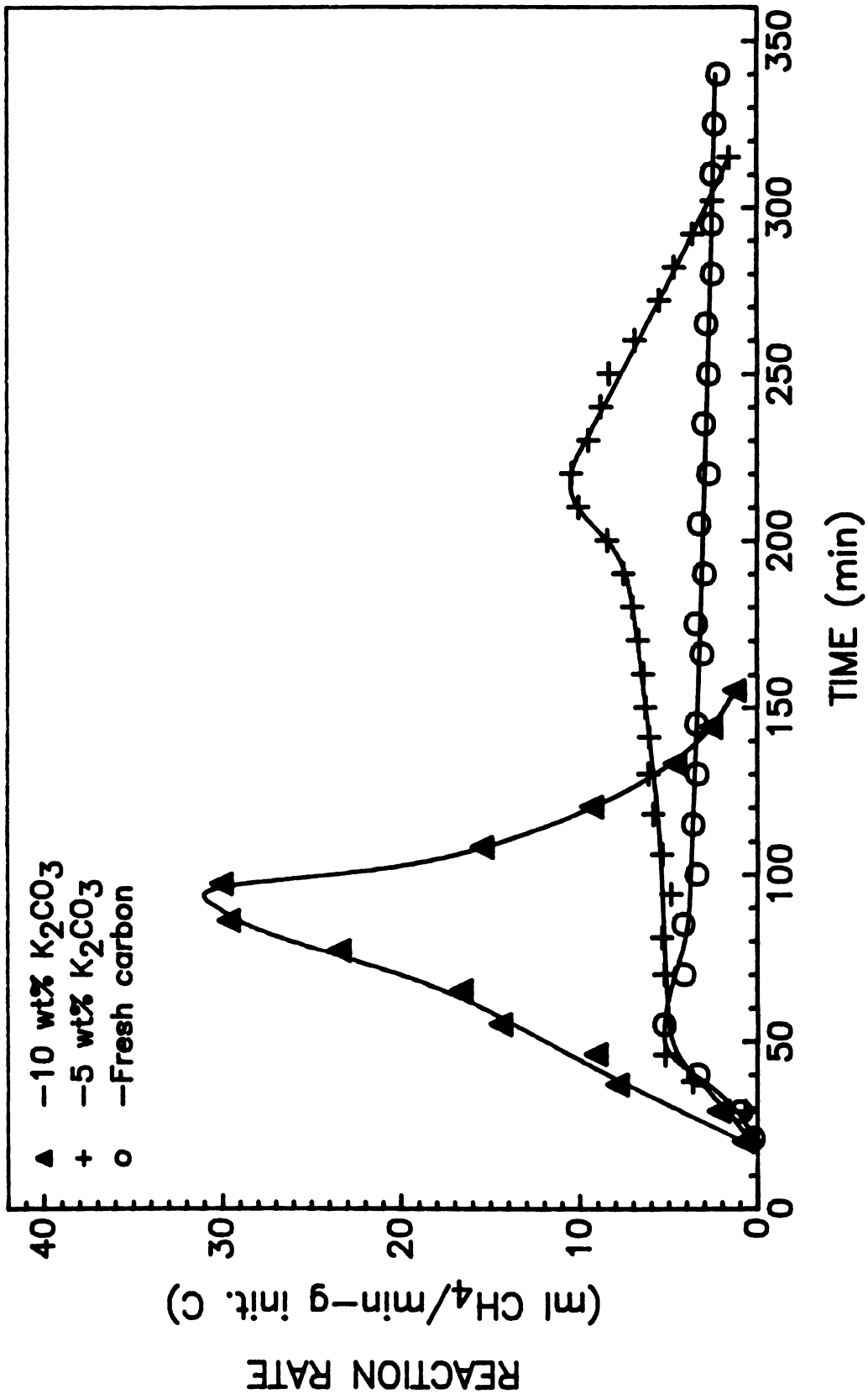

Figure 5.1 Absolute methane evolution rate from Raven 16 at 865 °C and 500 psig H_2.

The second assumption is that the presence of potassium carbonate on the surface of the carbon does not influence mass transfer processes within the voids and pores of the carbon bed. This assumption is plausible because the vapor pressure of free potassium metal (see Section 5.1.3) and partial pressures of other gases such as CO and CO_2 are very low compared to those of hydrogen and methane. Furthermore, the catalyst has a high degree of dispersion on the carbon surface and readily spreads into a very thin film on the carbon surface during reaction, thus not blocking the pores and voids appreciably. These two assumptions make the values of ϵ_p, τ_t and thus D_e independent of the catalyst loadings of interest in the experiments.

The value of hydraulic radius R_h of the ceramic boat sample holder used for the catalyzed experiments (see Section 4.2.1. and Equation 4-22) is not changed by the presence of the catalyst. Hence, the presence of the catalyst merely increases the magnitude of the rate constant k_{rxn} by a factor of 3, which in turn results in a Thiele modulus of 0.308 and an effectiveness factor of 0.96 if the catalyzed hydrogasification reaction exhibits first order kinetics. However, as discussed in Section 5.1.2, the kinetics of K_2CO_3-catalyzed hydrogasification is 3/2 order in hydrogen concentration. For a second order reaction

$$R_{rxn} = k_{rxn}^2 C_A^2 \tag{5-9}$$

where k_{rxn}^2 is the rate constant of the second order reaction [138] and C_A is the concentration in the bulk gas, the Thiele modulus ϕ is defined as

$$\phi = \frac{R_h}{3} \sqrt{\frac{k_{rxn}^2 C_A}{D_e}} \tag{5-10}$$

These two equations indicate that the value of the Thiele modulus does not depend on the order of the reaction, at least for reactions with simple kinetics. Thus, for a given hydrogen partial pressure an N-fold increase in the reaction rate simply increases the value of ϕ by a factor of $\sqrt{N}$. Hence, the value of ϕ equals 0.308 even for the 3/2 order hydrogasification.

For a given value of ϕ less than 0.5 the effectiveness factors for a second order reaction is at most 0.05 units lower than those for first order reactions [138]. Therefore, the effectiveness factor for the catalyzed hydrogasification of 3/2 order is expected to lie in between those of first order and second order reactions; *e.g.*, at least about 0.91. This implies that diffusion resistances again are negligible.

However, the assumptions made regarding the estimation of D_e may not be completely valid and thus the diffusion resistances were examined experimentally. Figure 5.2 represents the results of such a study in which the carbon bed depth was varied by a factor of three and the reaction rates were compared. The measured reaction rates of the two samples are essentially the same within the experimental error (see Figure 5.3). It clearly shows that reduction in the carbon bed thickness does not result in the enhancement of the measured reaction rates, implying that diffusion resistances are insignificant.

The absence of substantial mass transfer resistances is further supported by the results of activation energy measurements (Figure 5.4) [116]. As mass diffusion resistances become more significant, the magnitude of the apparent activation energy E_a' gradually decreases [137,138,165]. For ϕ greater than 3 the reaction kinetics are controlled by diffusion resistances and the value of E_a' reduces to half the value of the intrinsic activation energy E_a. In this range the Arrhenius plot would yield a straight line.

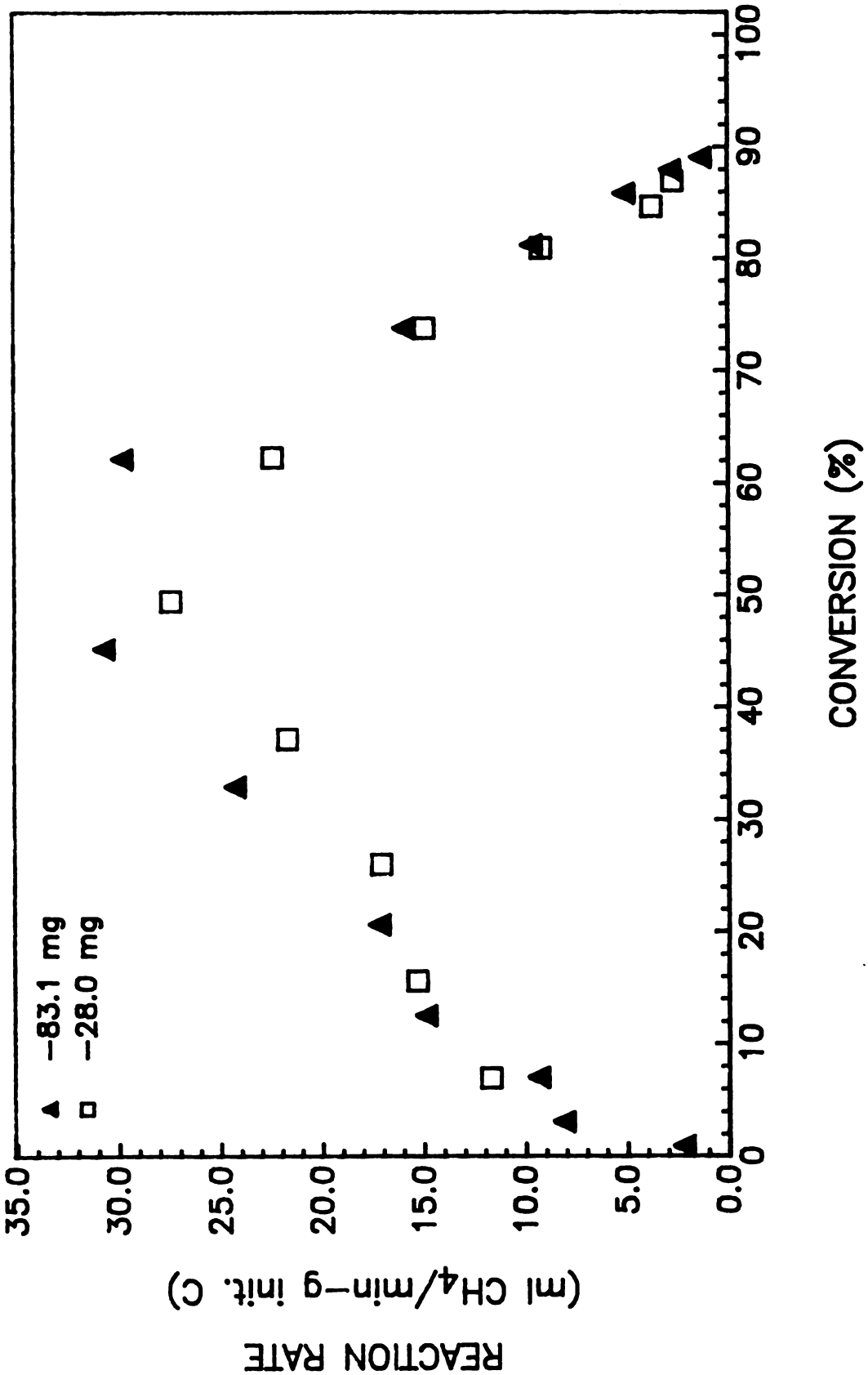

Figure 5.2 Mass transfer resistances during hydrogasification of catalyzed Raven 16 bed at 865 °C and 500 psig H_2.

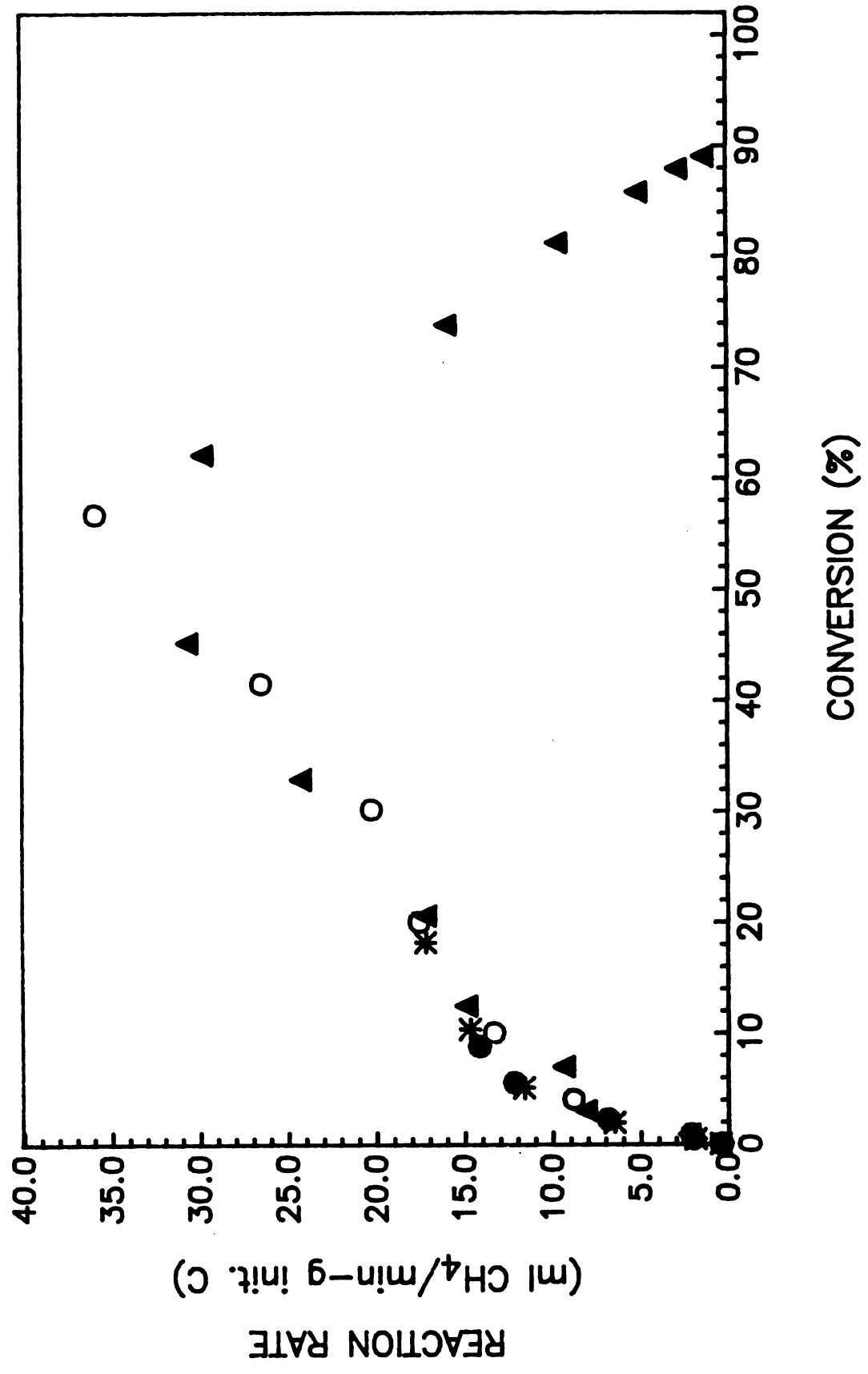

Figure 5.3 Reproducibility of hydrogasification rates of 10 wt%-K_2CO_3 samples at 865 °C and 500 psig H_2.

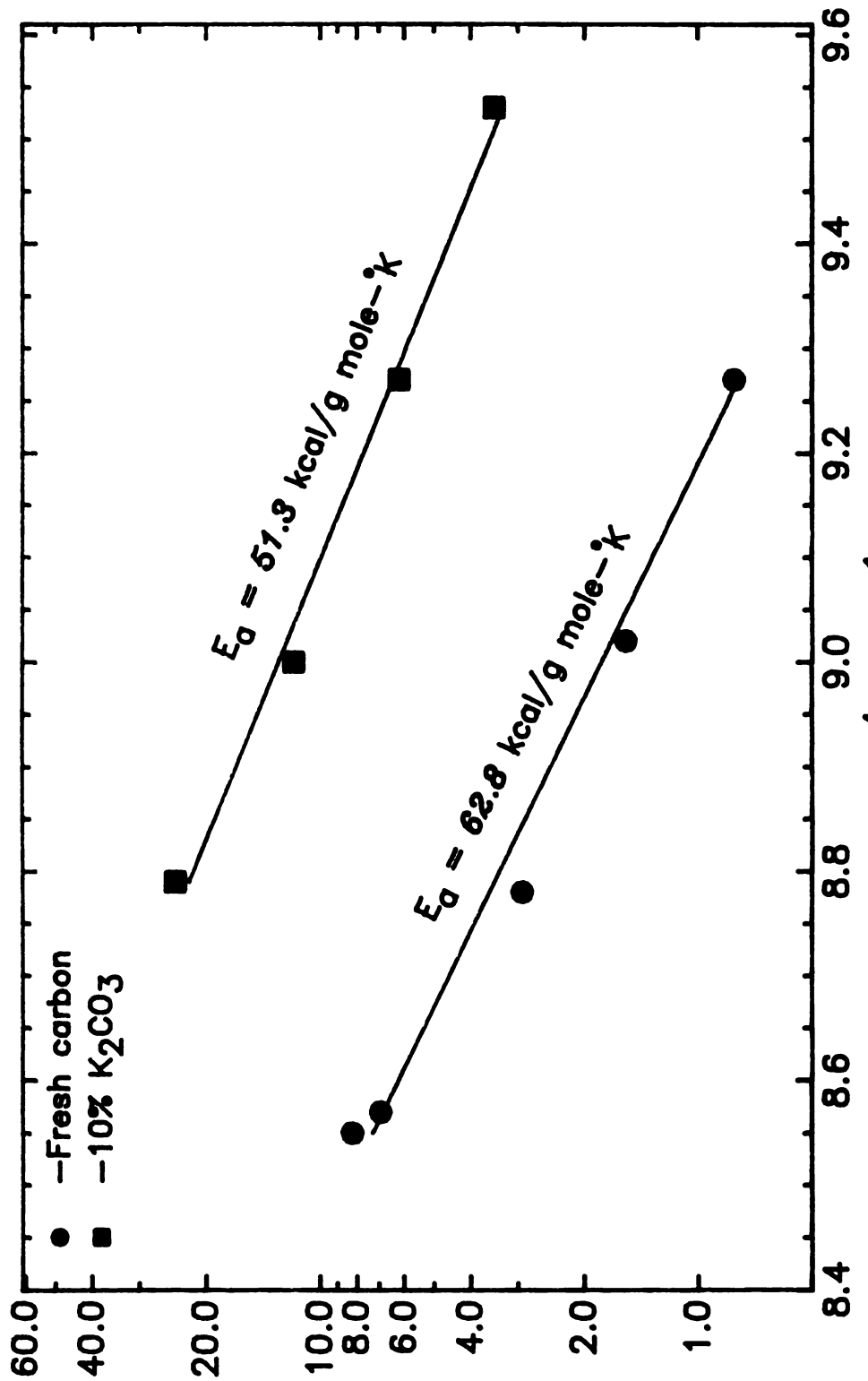

Figure 5.4 Arrhenius plot for hydrogasification of Raven 16 at 22% conversion under 500 psig H_2.

The Arrhenius plot of Figure 5.4 for 10 wt%-K_2CO_3 samples at 22% conversions is a straight line, and the calculated value for ϕ at 865 ° C, based on conservative assumptions, is however only 0.308. This value is not high enough to obtain a straight Arrhenius plot with substantial diffusion limitations present. Hence, it follows that strong diffusion limitations within the carbon bed of K_2CO_3-impregnated samples are absent, at least at lower conversions. It would be worthwhile to measure E_a at higher conversions where higher degrees of porosity are present. Furthermore, a value of 51.3 kcal/gmole-°K for E_a indicates that external mass transfer limitations are absent (see Section 4.2.1).

Therefore, the measured reaction rates for the catalyzed hydrogasification reactions for small sample sizes (~80 mg) are free from masking by significant diffusion limitations.

5.3 Hydrogasification of Coconut Charcoal

The hydrogasification procedure and conditions for K_2CO_3-catalyzed hydrogasification of coconut char were the same as the non-catalytic hydrogasification of carbon black discussed in Section 4.3.1 (865 ° C and 500 psi H_2).

Hydrogasification of samples of 150-200 mg (22.9 wt%-K_2CO_3) in ceramic sample holders yielded very high methane evolution rates, as can be seen in Figure 5.5. On one hand, the bulk density and the BET surface area of coconut char is higher than those of carbon black (see Sections 3.1.1 and 3.3.3) indicating larger particle sizes and a much higher degree of micro-porosity in coconut charcoal. On the other hand, the measured reaction rates in Figure 5.5 are about four times faster than those of the K_2CO_3-impregnated carbon black

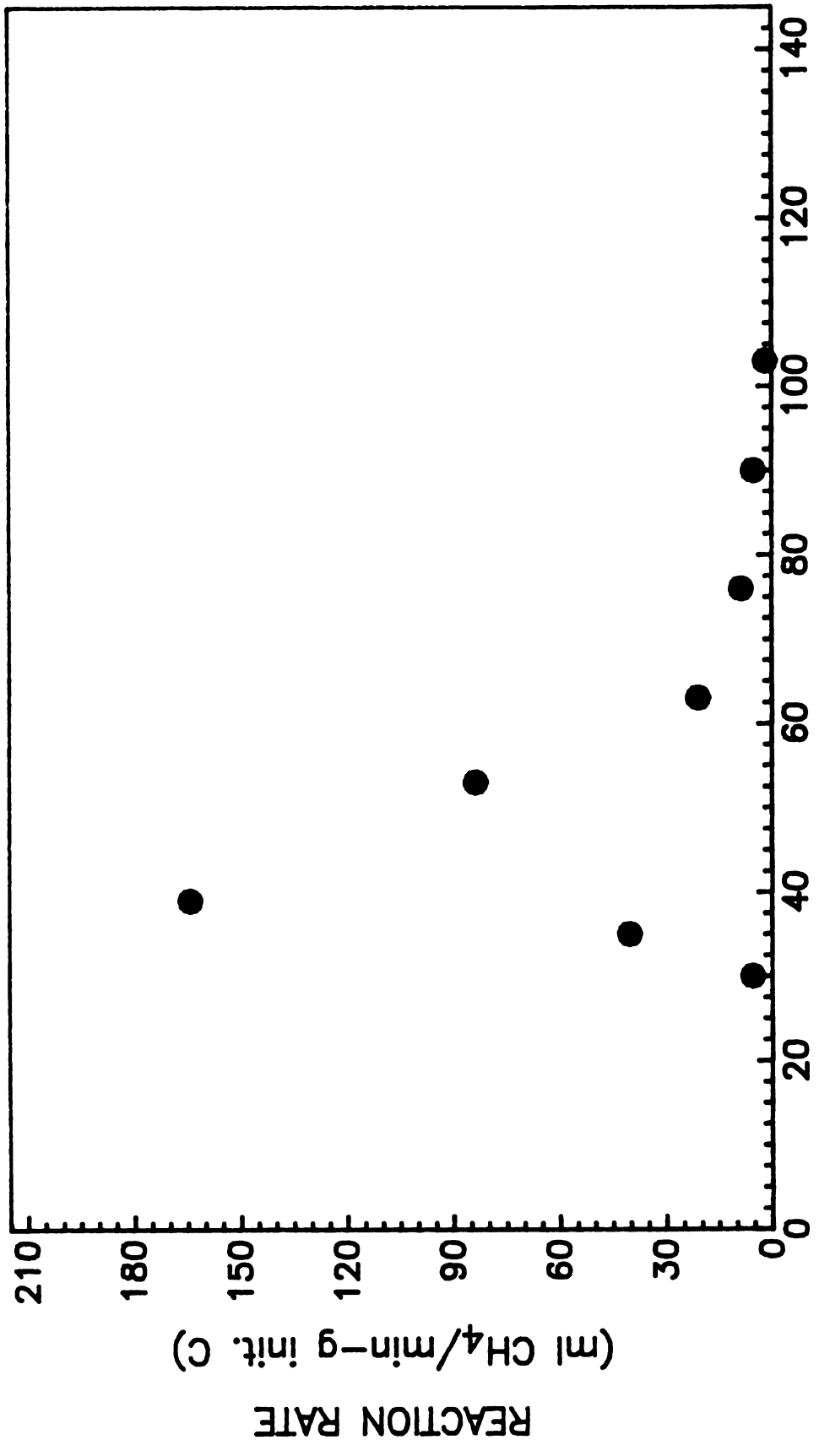

Figure 5.5 Absolute methane formation rate from coconut charcoal at 865 °C and 500 psig H_2.

samples and, thus, it follows from the discussion in Section 5.2 that diffusion limitations are definitely significant.

Furthermore, most of the carbon is hydrogasified before the steady state temperature of 865 ° C is established, making the determination of the actual solid carbon temperature at low conversion complicated. The high ash content of the coconut charcoal of more than 3.7% also introduces an element of uncertainity into the interpretation of the role of the catalyst.

Therefore, it was decided that the coconut charcoal was not a suitable choice for studying the catalysis of hydrogasification by K_2CO_3, and the experimentation with this char was not pursued.

5.4 Hydrogasification of Graphite

After using coconut charcoal, it was decided to use a carbon sample which had lower surface area and lower activity than the coconut charcoal so that mass diffusion resistances could be eliminated and the hydrogasification rates at low conversions under steady state temperatures could be measured. For this purpose, graphite powder samples impregnated with up to 9 wt% K_2CO_3 were tried (for characterization of this graphite see Section 3.2). The gasification procedure and conditions were the same as those for coconut charcoal.

The measured reaction rates for graphite samples were very low (even for 9 wt%-K_2CO_3 samples), but much too high to be accounted for by sample weight loss during hydrogasification. With a 9 wt%-K_2CO_3 sample in the reactor, maximum methane evolution rates (irreproducible) of only 2 ml/min were measured, and in experiments with no carbon sample inconsistent rates up to 0.9 ml/min were obtained. This indicated that in the former case, only a fraction

(which could not be determined with acceptable accuracy) of methane was from the graphite sample. The origin of the extra methane detected was determined to be the metallurgical carbon from the reactor vessel wall and the stainless steel screen used to keep the particulate carbon bed in place, which deposited out during thermal cycles from room temperature to the reaction temperature. The irreproducibility of the hydrogenation rate of these carbons made the accuracy of the measurements of the graphite hydrogasification rates highly uncertain.

Hence, it was decided to insert a quartz tube lining inside the reactor to eliminate contact between the high temperature bulk hydrogen gas and the wall of the reactor vessel in the hot zone. In addition, it was decided to use a more reactive sample so that the rate measurements of hydrogasification of carbon samples were not complicated by the methanation of the metallurgical carbon. Thus, further study of graphite hydrogasification was abandoned and carbon black Raven 16 was used for further studies.

5.5 Hydrogasification of Carbon Black

5.5.1 Procedure

Hydrogasification, oxygen chemisorption, and heat treatment procedures for K_2CO_3-impregnated carbon black samples were basically the same as those for the uncatalyzed samples (Section 4.3.1). However, minor modifications had to be made in a few cases to accommodate the presence of K_2CO_3 on the carbon surface; in experiments with degassed carbon black, degassing was carried out before impregnation with K_2CO_3, but in the case of heat treatments at 865 °C for three hours in He, the K_2CO_3 impregnation was done first. Furthermore, in experiments involving oxygen chemisorption on the carbon surface, the

chemisorption was done before the impregnation with K_2CO_3 (in one experiment oxygen was chemisorbed on carbon surface at 400 ° C after K_2CO_3 impregnation). The impregnation procedure and details are discussed in Section 3.3.2.

Some experiments were carried out on partially hydrogasified carbon black which was subsequently impregnated with K_2CO_3. For these experiments, fresh carbon black samples were hydrogasified to a desired conversion at 865 ° C in 500 psi H_2 and then were impregnated to the same level of potassium content that a fresh 10 wt% sample would have after gasifying to that conversion. These latter samples are referred to as "10 wt%" samples, although, the actual potassium carbonate loadings after 47% and 65% conversion were 11.8 wt% and 14.3 wt% of the impregnated samples, respectively.

Reaction rates were measured by collecting product gases in cold traps and subsequent analyzing by gas chromatography. The product gases were collected at steady state temperature of 865 ° C for a period of 10 sec to 1 min depending on the activity of the samples.

5.5.2 Results

5.5.2.1 Catalyzed Hydrogasification

5.5.2.1.1 Fresh Carbon Black

Raw hydrogasification rate data for the four carbon black samples studied are reported in Figures 5.1 and 5.6 as methane evolution rate versus reaction time. These results are typical of repeated experiments which exhibited good reproducibility (Figure 5.3). The start of experiment in the Figures 5.1, 5.5 and 5.6 (time = 0) is taken as the time hydrogen flow is begun (at 500 ° C) and

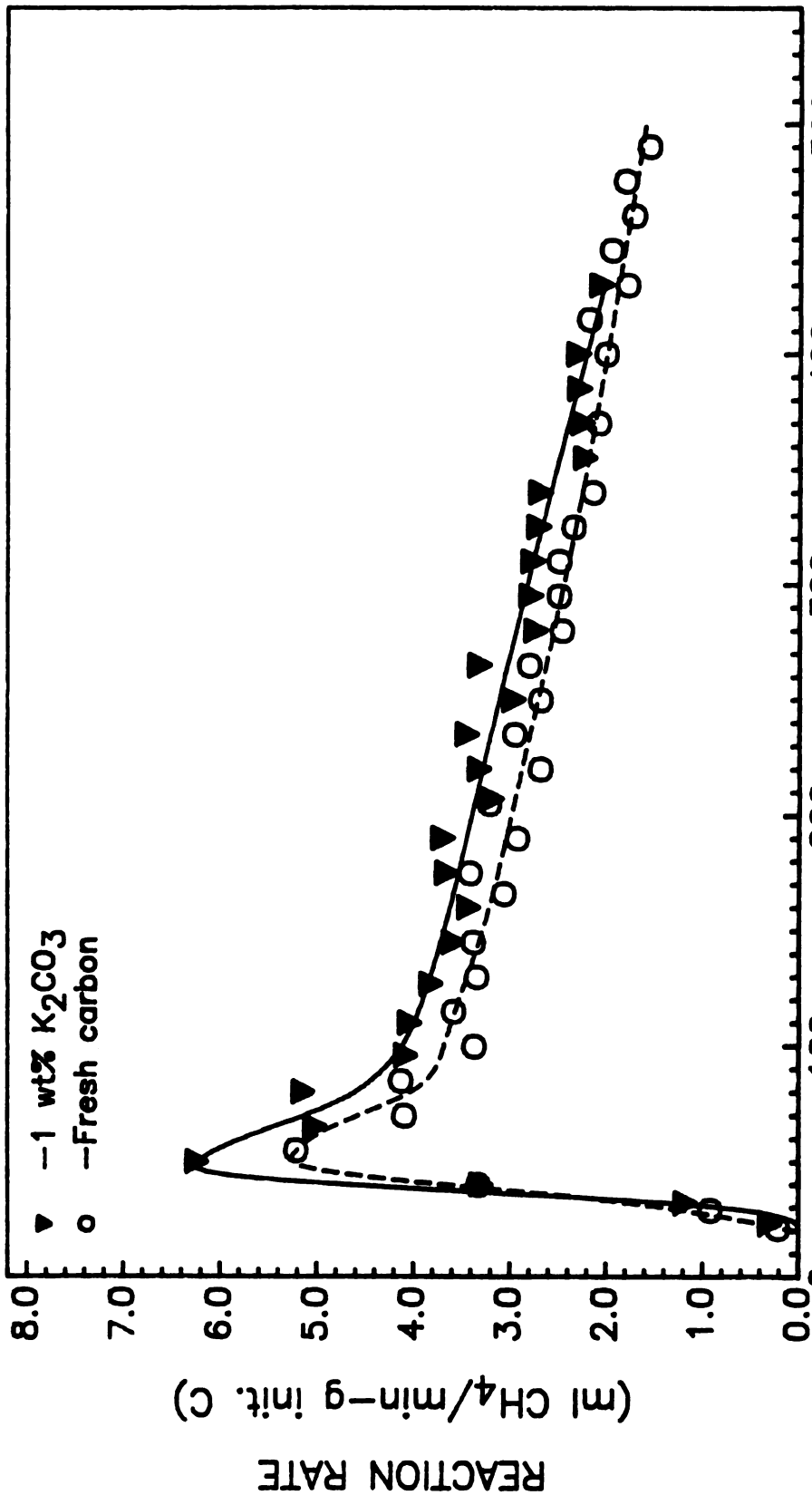

Figure 5.6 Absolute methane evolution rate from Raven 16 at 865 °C and 500 psig H_2.

heating the carbon sample is started. The methane evolution rate increases as reaction temperature is increased, approaching steady state of 865 ° C after 50 min reaction time. In all experiments carbon conversion is less than 10% when the steady state temperature is reached.

The conversion of carbon in each experiment is calculated by integrating the curves of methane evolution rate versus time. Complete conversion of 1 g of carbon to methane should yield 2036 ml of methane at 1 atm pressure and 25 ° C temperature, and the ratio of the curve integration to 2036 ml indicates the extent of the reaction. Conversion of carbon to other compunds is negligible because methane is by far the main product. For hydrogasification experiments with fresh and 1 wt% samples, the calculated conversions compared well at all burn off levels with conversions determined by weighing residual samples after experiment, showing that all methane is accounted for. For 10 wt% samples gasified to more than 85%, however, weight conversions were consistently 9-14% lower than the rate conversions. This is due to very short gas collection periods. Cold trap pressures are much lower than the pressure of the reactor effluent stream, and thus within a given period of time more gas is passed through the traps than expected from effluent flow rate. For gas collection periods of 1 min, used for fresh and 1 wt % samples, this effect does not appear to be significant; but, for a gas collection period of 10 seconds used for 10 wt% samples, this effect is severe. In these cases the gasification rates are normalized to weight conversions. The methane evolution rates reported in the Figures are all normalized.

Surprisingly enough, for 10 wt% samples gasified to 20-70% conversions, the rate conversions are lower than weight conversions 3-7%. For instance, in one experiment carried out at 776 ° C and 500 psi the rate conversion was 29% whereas the weight conversion was 66%. In this particular case, the sample

spontaneously burned (the sample became red hot) at room temperature as soon as it was taken out of the reactor and was exposed to the atmosphere. The thermocouple above the sample momentarily registered temperatures higher than 100 ° C. It thus seems that at low conversions some highly active complex is formed on carbon surface which readily reacts with oxygen even at room temperature. Therefore, for these samples the measured rates were normalized not to measured weights, but, instead, by reducing them by 10%, similar to the case of samples gasified to high burn off levels. The normalized rates are reported in Figure 5.3.

The results show that methane evolution rate decreases at steady state as carbon is consumed for fresh and 1 wt% K_2CO_3 loaded carbon samples (Figure 5.6). The addition of 1 wt% catalyst is seen to have little catalytic effect. In contrast, the methane evolution rate for the 5 wt% and 10 wt% loaded samples increases as carbon is consumed, reaching a peak at 60% conversion for both loadings (Figures 5.1 and 5.3). It is interesting to note that the initial steady state methane evolution rate for the 5 wt% loaded sample is nearly the same as that for the fresh carbon sample without catalyst. This observation cannot be explained satisfactorily at this point because the 10 wt% sample behaves differently.

5.5.2.1.2 Treated Carbon Black

Reaction rate data of differently-treated "10 wt%"-carbon samples are presented in Figures 5.7-5.10. Treatments such as oxidizing, degassing and gasifying, individually or in combination, were used to obtain more insight into the nature of the carbon surface during gasification.

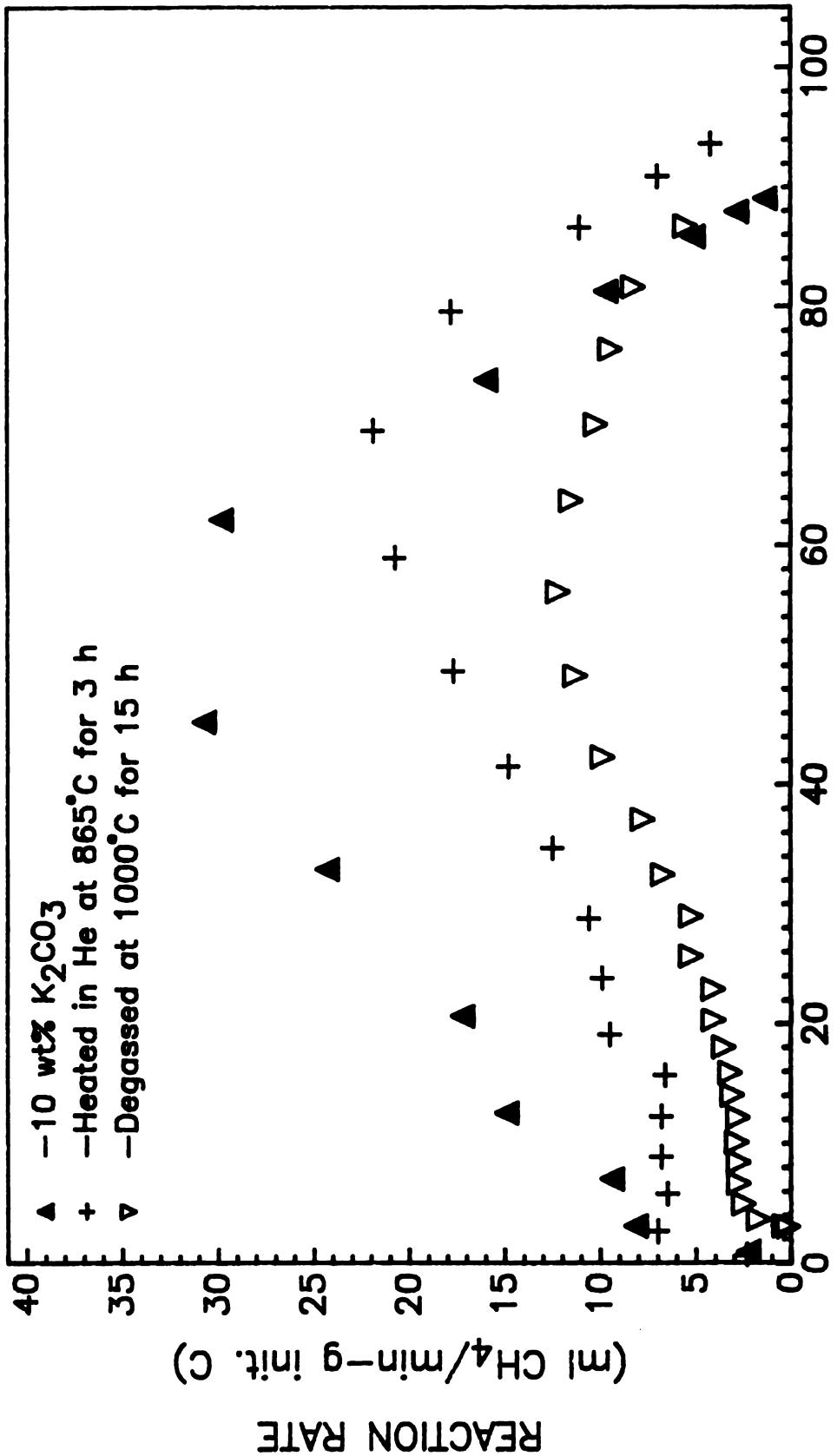

Figure 5.7 Catalyzed gasification rate at 865 ° C and 500 psig H_2 versus conversion.

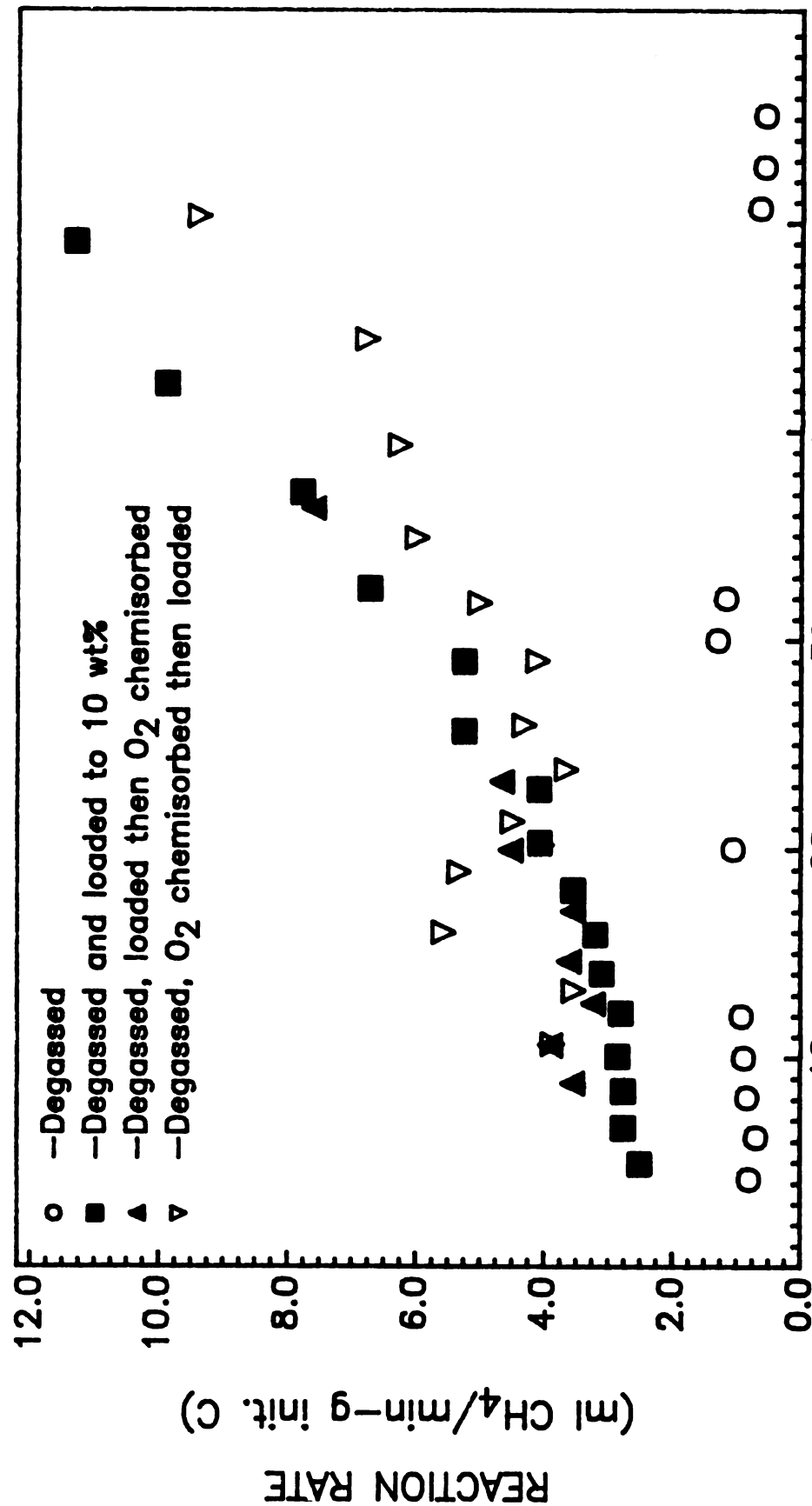

Figure 5.8 Effect of oxidation at 400 ° C and catalyst addition on gasification rate at 865 ° C and 500 psig H_2 of degassed carbon.

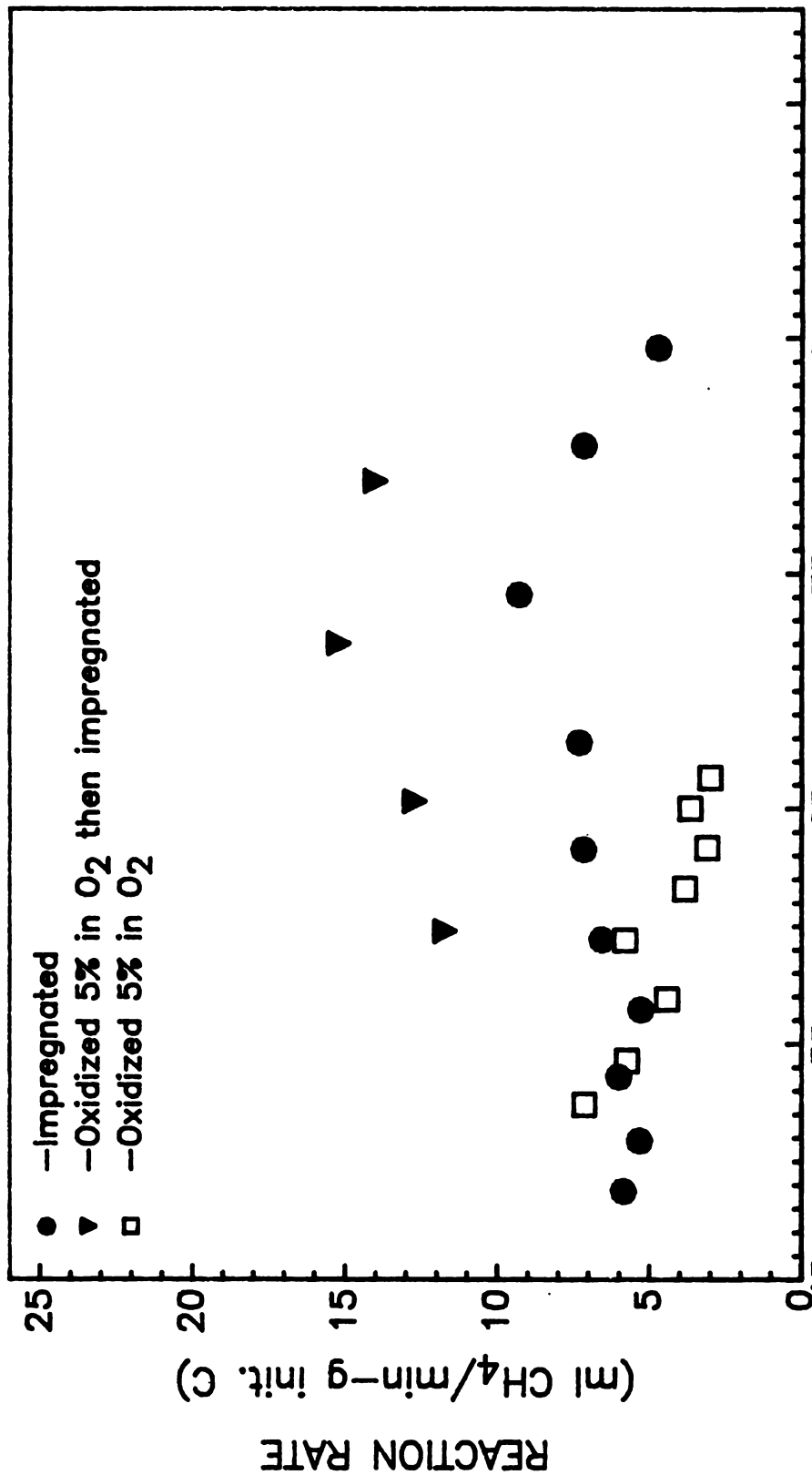

Figure 5.9 Effect of oxidation at 400 °C and catalyst addition on gasification rate at 865 °C in H_2 of 47% gasified carbon.

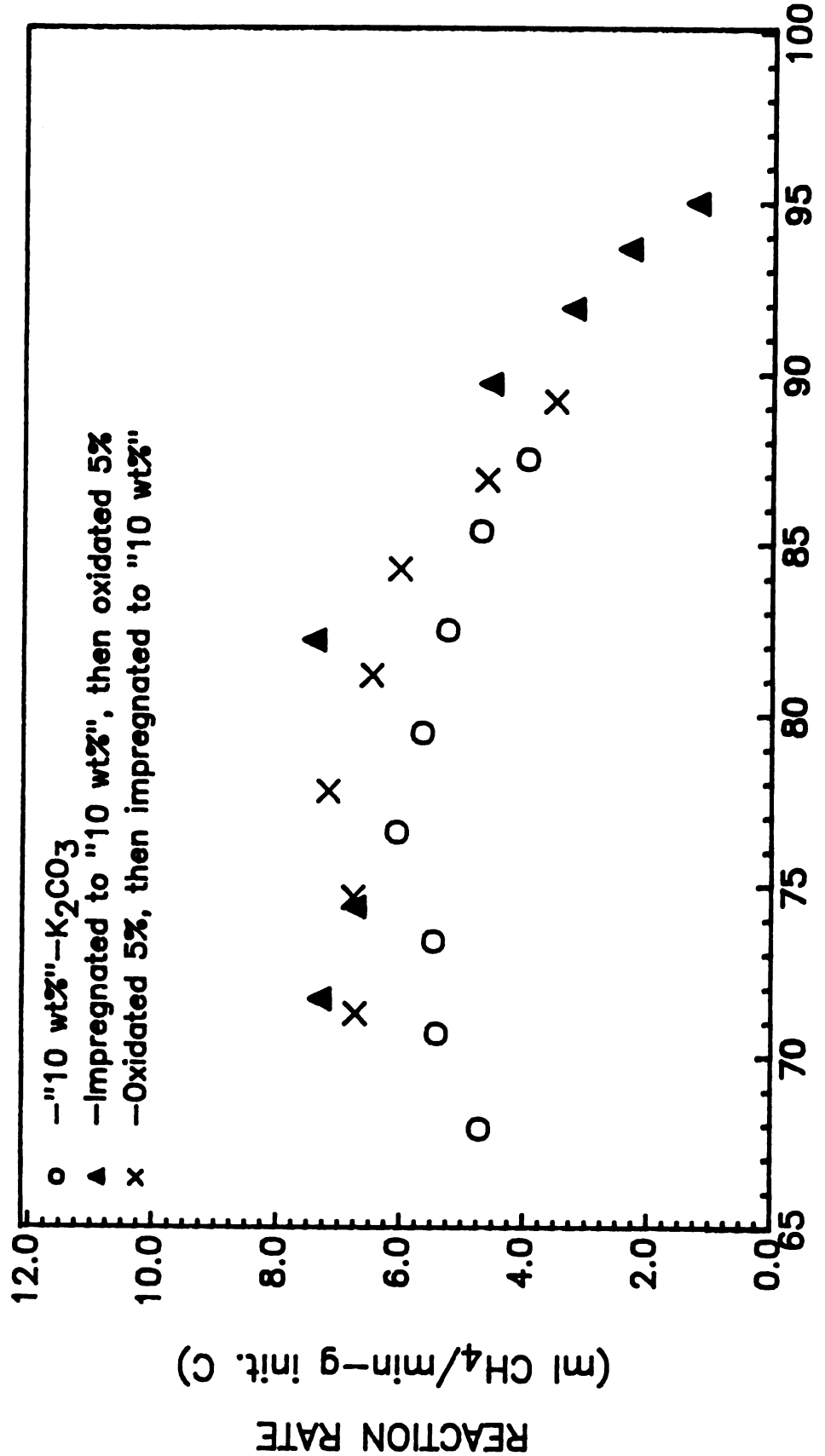

Figure 5.10 Effect of oxidation at 400 ° C and catalyst addition on gasification rate of 65% gasified carbon at 865 ° C in H_2.

Generally, such treatments did not change the trend of reactivity of samples versus time or conversion, though the absolute rates were influenced. Heating in helium (at 865 ° C for 3 h) after impregnation or degassing prior to impregnation reduced the reaction rates of the samples significantly, with degassing effect being more severe (Figure 5.7). Oxygen chemisorption at 400 ° C either before or after impregnation did not enhance the reactivity of a degassed fresh carbon sample (Figure 5.8). However, the reactivity of a pure carbon sample gasified to 47% or 65% conversion and then oxidized at 400 ° C before impregnation did increase to some extent (Figures 5.9 and 5.10). Again, the experimental results were fairly reproducible.

5.5.2.2 Catalyst Loss

5.5.2.2.1 Fresh Carbon

The surface of carbon black carbothermically reduces K_2CO_3 to free potassium metal which is readily lost from the carbon bed via vaporization (see Section 5.1.3). The total amount of potassium in the reaction zone of the reactor (sample, sample holder and the quartz lining of the reactor around them) during hydrogasification was calculated from the γ-ray emission rate versus time (Equation 2-15) recorded by the detector. The curves of total amount of potassium in this zone versus time are given in Figure 5.11 for the 5 wt% and 10 wt% samples.

The actual amount of potassium on the carbon black surface, as opposed to the reaction zone, is of greater interest. Thus, following gasification, carbon was removed from the sample holder and the potassium content of the sample itself was measured by NAA. This sample catalyst loading is plotted in Figure 5.12 as a function of conversion for the 10% sample along with the amount of

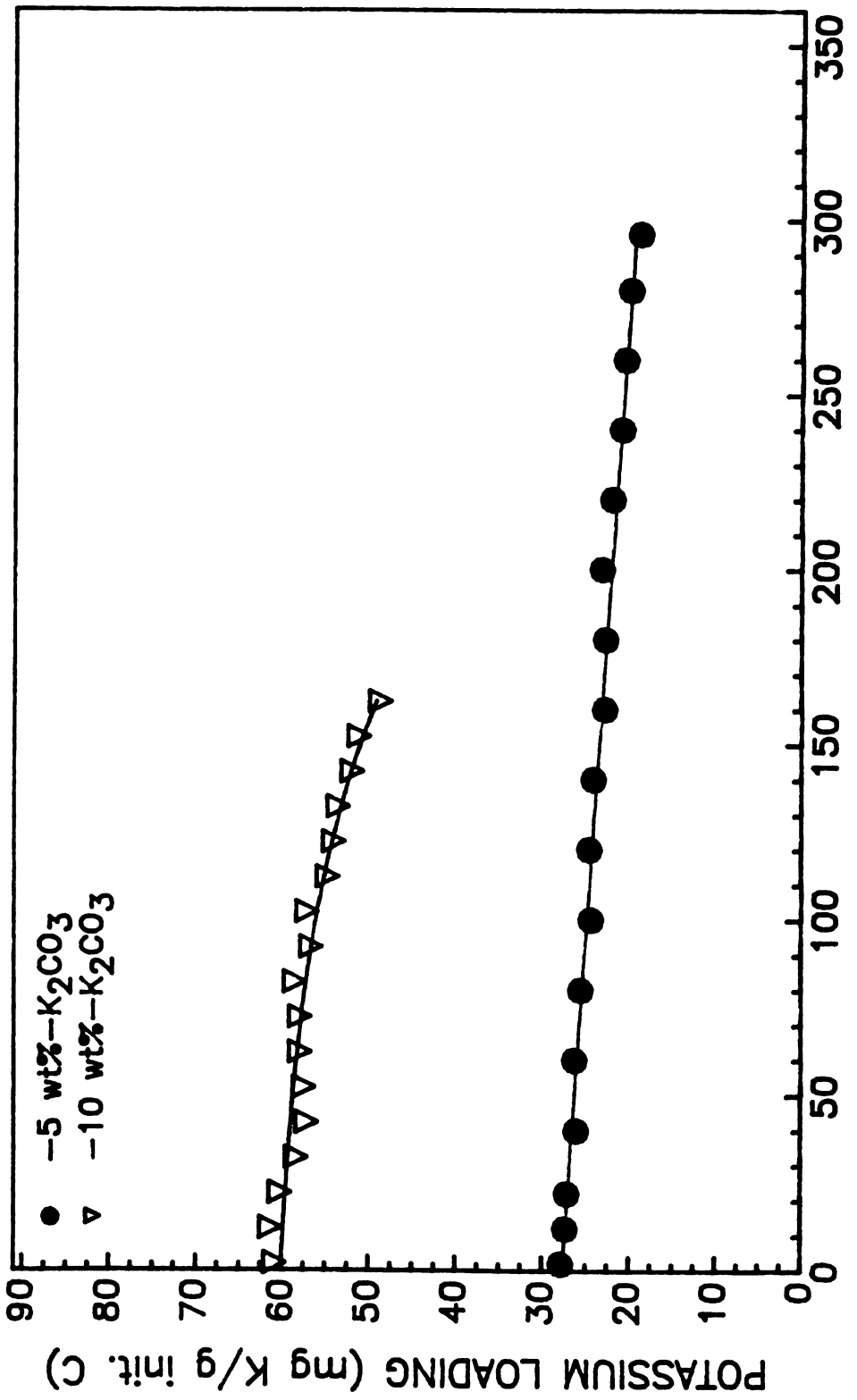

Figure 5.11 Potassium loss from reaction zone during hydrogasification at 865 °C and 500 psig H_2 measured by γ-ray detector.

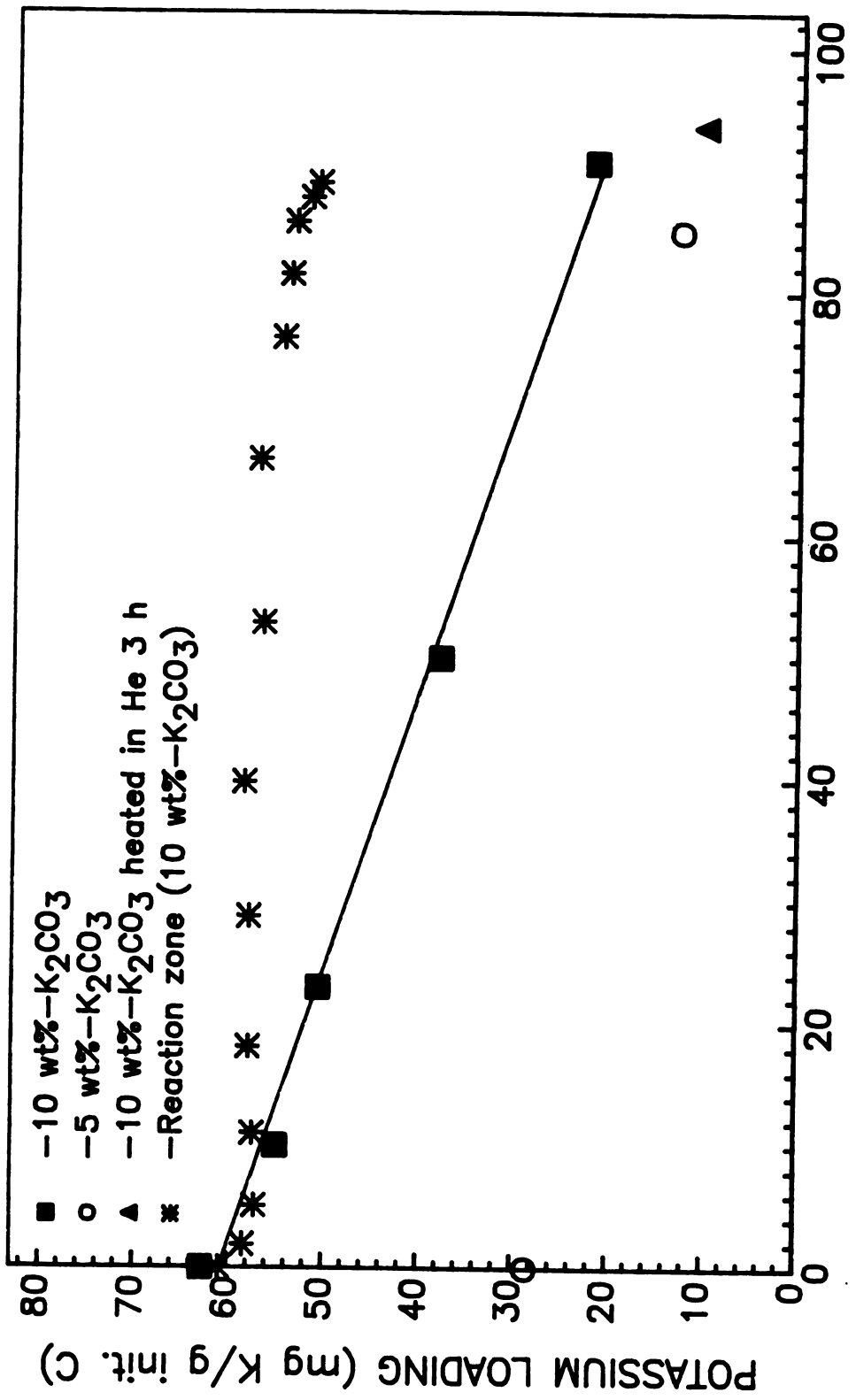

Figure 5.12 Potassium loss from K_2CO_3-loaded Raven 16 during hydrogasification at 865 °C and 500 psig H_2

potassium in the reaction zone. It is seen that potassium loss from the reaction zone via evaporation at 865 ° C in hydrogen is slow, but the potassium loss from the sample is significant. The catalyst loading is seen to decrease linearly as carbon is consumed. The residual loading for residual 10% (pretreated in helium) and 5% loaded samples are also given.

5.5.2.2.2 Treated Carbon Black

The catalyst loss from treated (degassed, oxidized or heated in He) carbon samples at gasification temperatures are shown in Figures 5.13 and 5.14. It is seen that a degassed carbon sample impregnated to 10 wt%-K_2CO_3 lost catalyst during gasification much faster than a sample that was not degassed, to the extent that the amount of the potassium on the carbon reduced to a level less than that of the 5 wt%-K_2CO_3 sample (Figure 5.13). Carbon samples gasified to 47% or 65% conversion and then impregnated also lost catalyst during further gasification much faster than 10 wt% sample (open symbols near 80% conversion). When the 47%-hydrogasified sample was heated in helium at 865 ° C for 3 h, the potassium content reduced to that of the degassed sample at that conversion (open circle at 47% conversion on the middle line in Figure 5.13). In all cases, samples degassed or hydrogasified to moderate or high conversions prior to impregnation lost catalyst much faster than the untreated samples.

Oxygen chemisorption at 400 ° C seemed to partially compensate for the effect of degassing on catalyst loss, but had little effect on the partially gasified samples (Figure 5.14). Comparison of Figures 5.13 and 5.14 reveals that, after 10-20% conversion, the rate of catalyst loss (slope of potassium loading vs. conversion) was not influenced by oxygen chemisorption; the oxidation of degassed samples merely reduced catalyst loss at the early stages of the

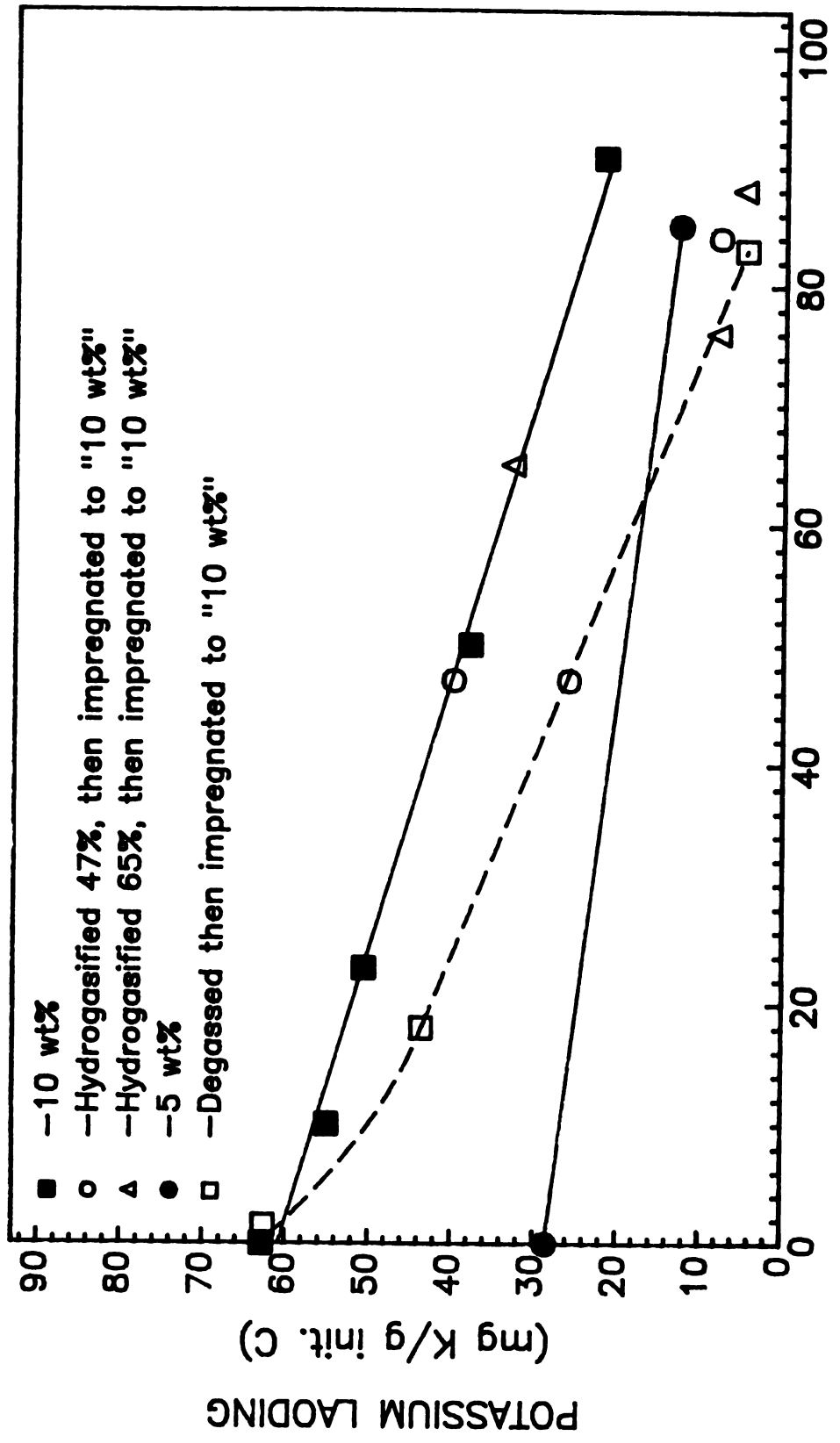

Figure 5.13 Effect of high temperature treatment on potassium content of carbon samples at various levels of conversion (865 °C).

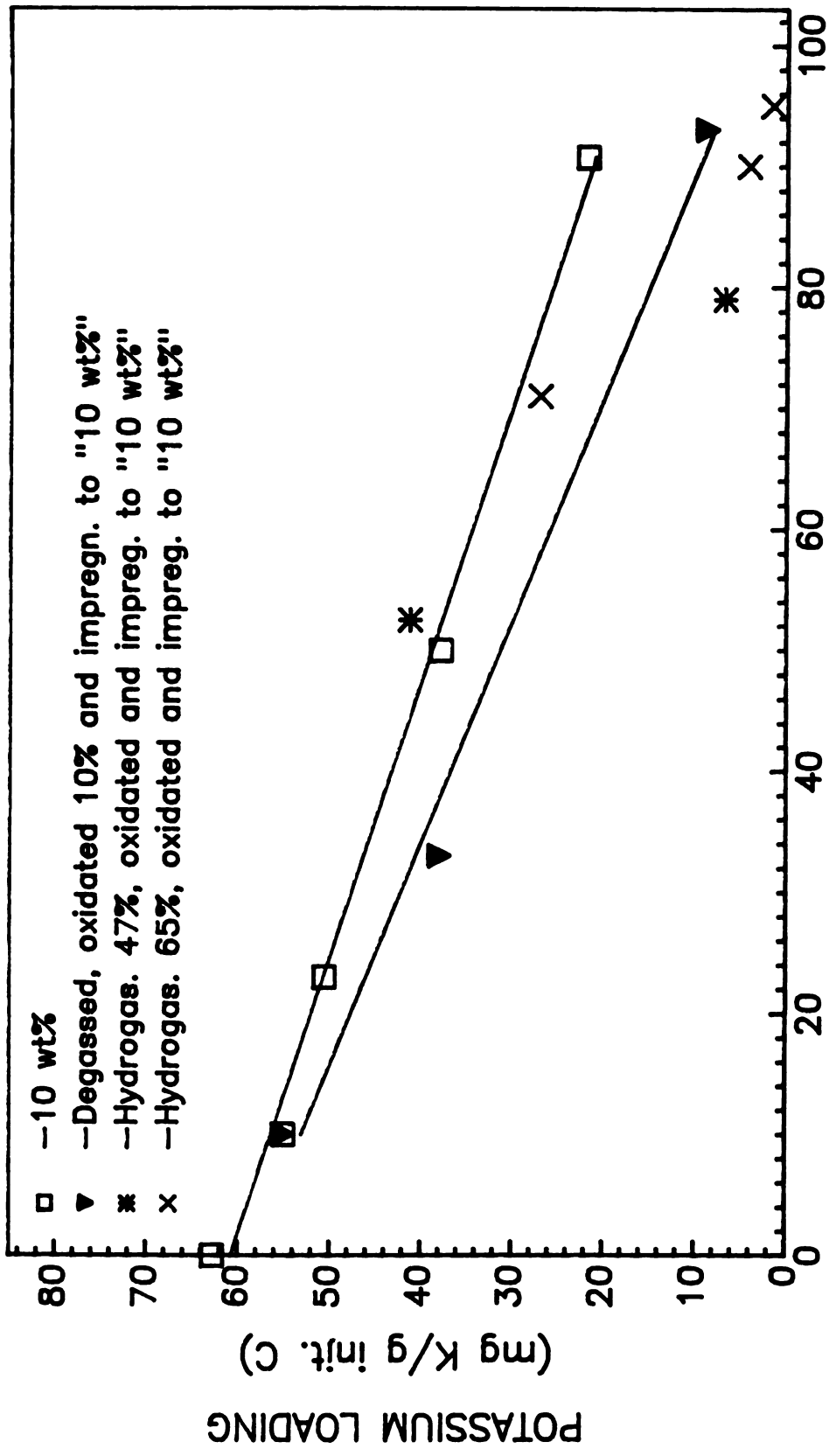

Figure 5.14 Effect of oxidation at 400 °C on potassium content of carbon samples at various levels of conversion (865 °C).

gasification.

5.5.3 Discussion

The main objective of this study was to elucidate some general features such as the extent of the influence of oxygen surface complexes on K_2CO_3-catalysis of hydrogasification. To this end, the K_2CO_3-catalysis of gasification of fresh carbon black was studied first and then the effect of some treatments such as degassing were studied. Here, the general features of the catalysis of gasification of fresh carbon are discussed first, and then the influence of various treatments are discussed with the reinterpretation of the general features in the light of these results.

5.5.3.1 Hydrogasification of Fresh Carbon Black

Because gasification is a heterogeneous reaction, the representation of gasification rate should be based on either a total surface area or active site density. The gasification rates measured for all samples are represented as specific rate (methane evolution rate per unit surface area) based on the total surface area measured as a function of conversion (Figure 3.1). Total surface area is used instead of active surface area because measurement of active surface area is extremely complicated; the magnitude of the area depends on the conditions and gases used and they do not necessarily represent the catalyzed gasification conditions. The specific gasification rate is plotted in Figure 5.15 for each loading as a function of carbon conversion. The specific rates for the uncatalyzed and 1% loaded samples decrease strongly during reaction (by a factor of five), while those for the 5% and 10% loaded samples remain essentially constant or increase slightly in the conversion range of 15-65%.

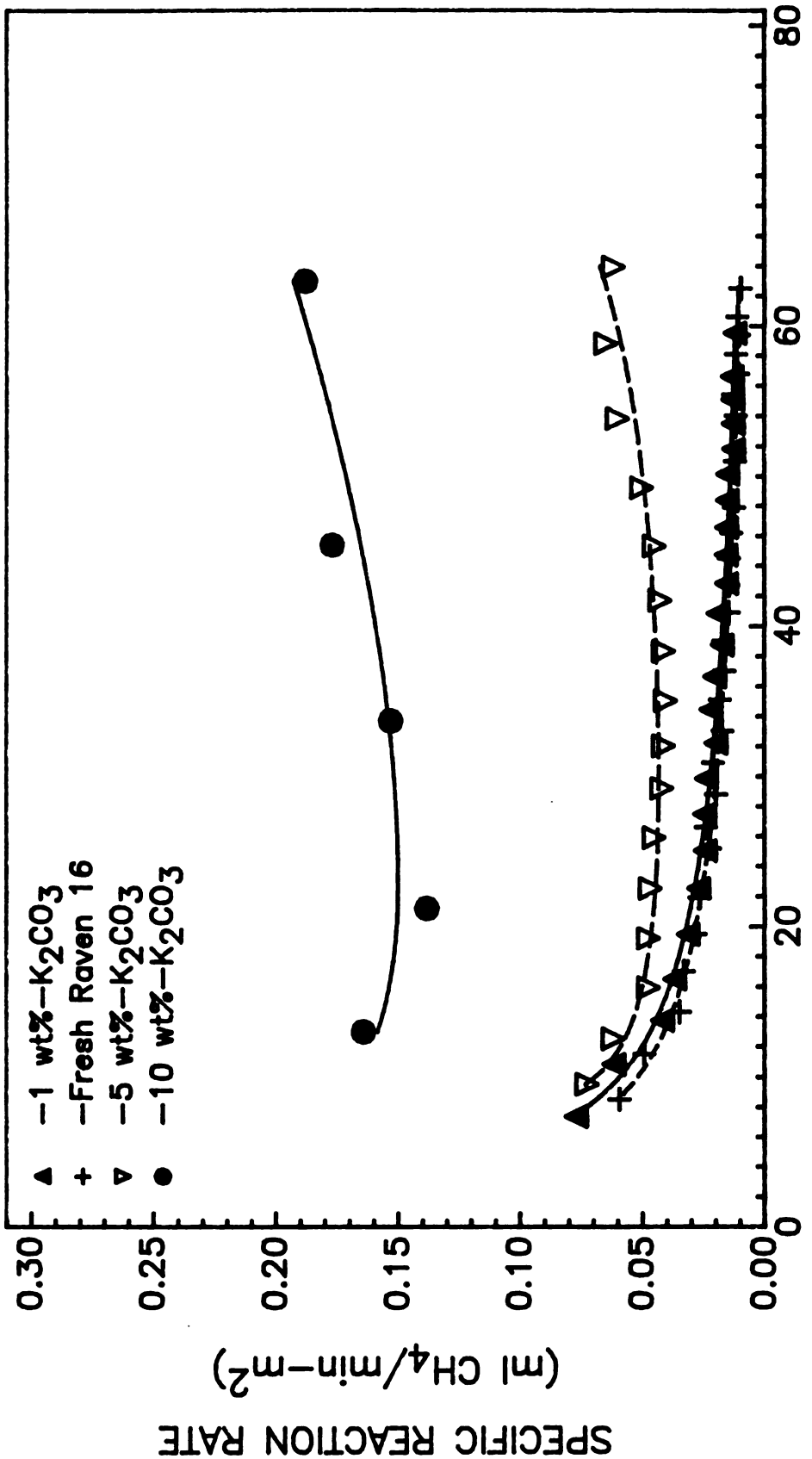

Figure 5.15 Specific methane evolution rate of Raven 16 at 865°C and 500 psig versus carbon conversion.

A convenient and meaningful way of comparing catalyst activities under various conditions is to adapt the relative reaction rate parameter versus conversion (Figure 5.16). The relative reaction rate parameter is defined as the ratio of the gasification rate of a sample at a given conversion to the reaction rate of an uncatalyzed, untreated, fresh carbon sample at the same conversion. When this parameter is equal to one (horizontal dashed line at the bottom of the graph), it implies that a sample has the same activity as a fresh carbon; or in other words, that the catalyst is inactive at that conversion. In Figure 5.16 the relative reaction rates of 1 wt%, 5 wt% and 10 wt% samples are plotted. It is clearly seen that the effect of adding catalyst is not noticeable for the 1 wt% and is initially quite small and increases dramatically during reaction for 5 wt% and 10 wt% samples. This latter observation is extremely important and was the starting point and the cornerstone of further study. The totality of the research presented here was carried out as an attempt to explain this simple and basic observation.

These results provide insight into the role of potassium carbonate in enhancing hydrogen gasification rate. First, some factor other than the mere presence of the carbonate catalyst is also involved; otherwise, the reactivity should decrease as potassium content of the carbon sample is decreased by potassium loss from the sample (Figure 5.12). This is not observed; the reactivity increases as more potassium is lost from the carbon sample. Second, it is clear that the catalyst does more than simply increase the reactivity of existing reactive sites on the carbon surface, for if this were the case, the ratio of catalyzed to uncatalyzed reaction would be constant during gasification; the enhancement factor. Instead, the catalyst must become more active as new surface area is developed and interacts with the catalyst. The interaction produces new reactive sites on the carbon surface, resulting in an overall increase

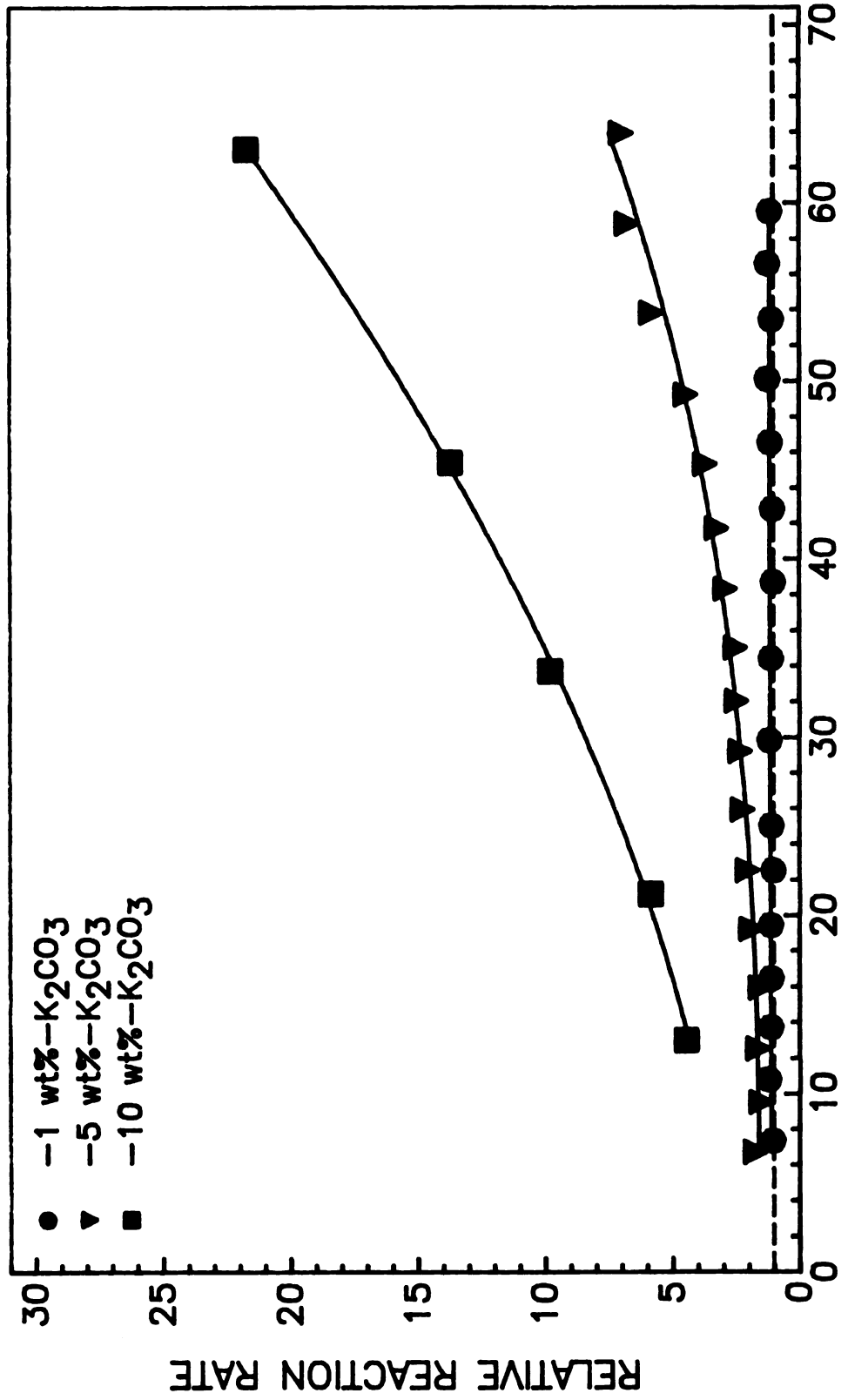

Figure 5.16 Hydrogasification rates relative to uncatalyzed rates versus carbon conversion at 865 °C and 500 psig H_2.

in absolute reaction rate as gasification proceeds. In the absence of catalyst, no new active sites are produced, and the absolute gasification rate decreases slowly, possibly by thermal annealing of active sites.

The constant or slowly increasing value of specific rate for the 5% and 10% loaded samples indicates that in both cases the catalyst present is able to activate, maintain the activity of, and even increase the activity of new surface area formed in gasification. This is surprising, as it appears not enough catalyst is present to cover the extended area formed. A simple calculation shows that, if one assigns a molecular area of 10 $Å^2$ to a potassium atom on the carbon surface, the initial catalyst loadings of 5% (K/C=0.009) and 10% (K/C=0.019) correspond to a monolayer coverage of potassium on areas of 43.6 m^2/g and 87.2 m^2/g, respectively. These areas covered by catalyst are even smaller at high conversion, as approximately 40% of the catalyst is lost at 60% carbon conversion (Figure 5.12). It thus appears that the reactive area which the catalyst activates is a small fraction of the BET area, and that the reactive area is formed at least in proportion to the BET area during gasification. This is in agreement with the general consensus [166] that gasification occurs at edge sites on the carbon surface.

The increase in specific rate for the 10% over the 5% catalyst loading is not easily explained by a simple surface coverage of reactive sites. The ratio of observed specific rates of 10% and 5% samples is approximately three over the entire range of carbon consumption. It is not clear at present as to how this additional catalytic effect, above that predicted by a linear increase with loading, arises. One explanation is that some fraction of the catalyst on the carbon is deactivated at the beginning of gasification or cannot be activated during gasification [167]. For instance, if two weight percent of catalyst is not active, the ratio of active catalyst for the 10% and 5% catalyst becomes 8:3, a ratio

close to the value of three for the observed reaction rates. This concept of inactive catalyst also explains the lack of observed catalytic activity for the 1% loaded carbon sample. The deactivation of catalyst has been suggested to result from reaction with the impurities in the starting carbon or possibly from intercalation of potassium into carbon. The possibility of intercalation at gasification conditions, however, has been discounted at high temperatures for gasification in other environments [159,160,168]. It may well be that a minimum amount of catalyst must be present on the carbon surface in order to provide an environment in which active catalyst species can form; this explanation is the most plausible for the observed gasification behavior.

The rate per catalyst atom present on carbon increases several-fold during gasification, while the catalyst loading per unit area decreases. This seems to indicate that either just a fraction of the catalyst is necessary to activate the carbon surface or the catalyst is activated gradually as higher conversions are approached. In the latter case, most of the catalyst is probably in an inactive form and as new surface area is developed it is activated via interaction with the new surface. Wigmans *et al.* [169], have noted a similar phenomenon, stating that the quality of an active site increases during gasification as catalyst is activated from an inactive state. One explanation is thus that the observed increase in gasification rate is dictated solely by activation of the catalyst. In this case, the carbon surface area would be inconsequential as long as sufficient area is available for the activated catalyst to spread onto.

If catalyst activation is a slow process, one would expect that helium pretreatment at high temperature would facilitate catalyst activation, and therefore result in higher gasification rate. The results of such an experiment are shown in Figure 5.17, in which the sample was held at 865 °C in helium for three hours and then gasified. It is seen that gasification rate was lower after

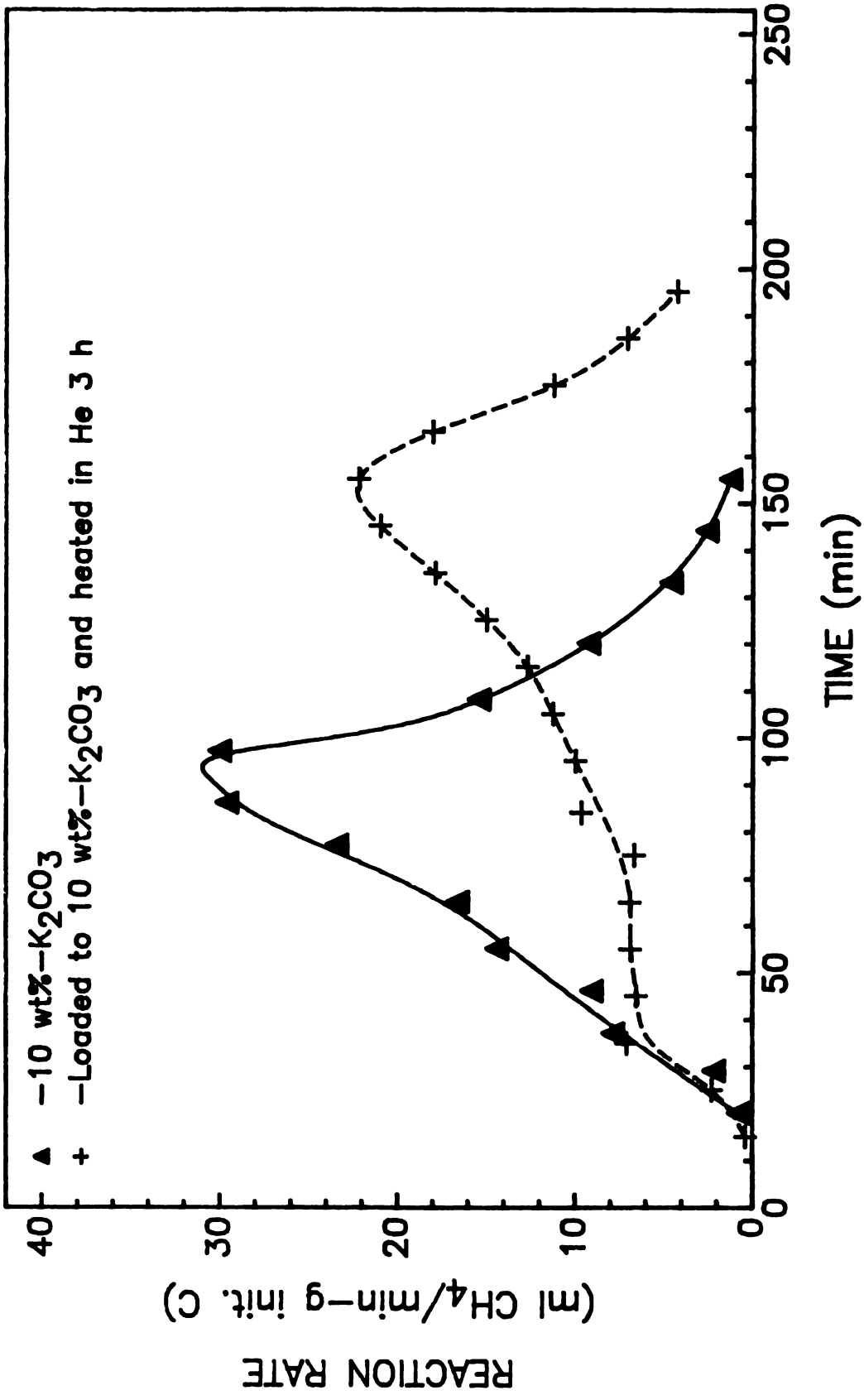

Figure 5.17 Effect of heat treatment on reactivity of impregnated Raven 16 at 865 °C and 500 psig H_2.

pretreatment, indicating that catalyst is either not activated in helium or only activated as carbon is consumed.

5.5.3.2 Potassium Catalyst Loss

The results of potassium catalyst loss measurements (Figures 5.11 and 5.12) indicate that catalyst loss by evaporation out of the reaction zone is relatively slow at 865 ° C in hydrogen. However, catalyst loss during gasification by migration onto the sample holder and by evaporation and condensation onto the quartz insert is significant, as indicated by the results presented in Figure 5.12 for catalyst loading measurements following gasification.

The loss of catalyst is apparently associated with the extent of gasification, and not merely with time of exposure to high temperature. This was illustrated by the experiment in which a 10% loaded sample was held in flowing helium at 865 ° C for three hours. Catalyst loss in this experiment was only 4% (2.4 mg K/g initial carbon) after the extended exposure. The catalyst loss during the gasification which followed, however, was quite similar to that for samples not heated in helium. The final catalyst loading is given by the open circle in Figure 5.12. Sams *et al.* [157] have concluded that K_2CO_3 is not lost from carbon sample appreciably below its melting point of 891 ° C as long as it is in the form of carbonate, and that the formation of free potassium metal is a prerequisite for rapid loss of the catalyst. That is, the interaction of K_2CO_3 with carbon surface is necessary for the reduction and subsequent loss of the catalyst. Thus, it seems that on surface of fresh carbon insufficient number of active sites are present for substantial interaction with K_2CO_3 and the catalyst remains mostly in form of carbonate, or the interaction with carbon surface forms potassium containing complexes that stablize the potassium on the surface. At higher conversions, however, more surface area is developed and more active sites are available, so

that more catalyst is activated and is lost from the sample. This subject will be discussed in more detail in the following Section.

5.5.3.3 Effect of Treatments on Catalysis

The interpretation of the results relevant to the role of oxygen groups in the alkali-catalyzed gasification are more conclusive if the catalyst losses and the catalyst activities are studied together. Some of earlier results are also reinterpreted within the framework of the findings of this Section.

The comparison of potassium loadings in Figures 5.13 and 5.14 shows that a degassed carbon loses potassium much faster than a fresh carbon sample, and that oxidation of the surface at 400 ° C improves the potassium retention ability of the carbon to some extent. This improvement is observed throughout gasification although the rate of the catalyst loss is essentially the same after 20% conversion. The corresponding reaction rates in Figure 5.8, however, show a slight decrease following oxidation. Both the added catalyst retention and lower rate suggest the deactivation of a portion of the catalyst via formation of stable surface compound(s) of potassium upon oxidation of the surface. Harker [170] has attributed the catalytic activity of alkali-metal salt in oxidizing atmospheres to its ability to destroy the acidic surface oxides by neutralization/decarboxylation or attack by free metal. So at this point it is not possible to speculate on the nature of these stable and inactive compound(s). The catalyst that did not interact with these particular oxygen groups remained active.

The results look somewhat different at 47% and 65% conversion. The oxidation did not seem to improve the catalyst retention ability of the carbon, but it did enhance the reaction rates as can be seen in Figures 5.9 and 5.10. In these cases potassium was lost rapidly from the carbon samples and its level was

reduced to that of a 10 wt%-degassed sample when gasified to the same conversion (open triangles and circles around 80% conversion in Figure 5.13; crosses and asterisks above 80% conversions in Figure 5.14). Apparently, at high conversions the stable inactive surface compounds of potassium were not formed, at least to the same extent as at low conversion. Instead, some other intermediate species were formed that were active. The higher activity at the same potassium content in these cases as compared to the degassed samples suggests that either the potassium complexes formed on the surface were different or the portion of the potassium lost from the surface was involved in a mechanism that created more active sites. In the former case, the observation that potassium contents were the same then is just a coincidence.

In either case, the implication is that the carbon surface structure is different at these higher conversions. The surface structure is different due to the fact that significant porosity develops as carbon is gasified. The drastic increase in surface area during gasification, from 15-20 m^2/g in fresh carbon to about 400 m^2/g at 60% conversion (Figure 3.1), is much too high to be accounted for by a simple reduction in the carbon particle diameter, and porosity development is the most plausible explanation. These different structures very likely were also responsible for the lower enhancement of the reaction rates of the uncatalyzed carbon samples when oxidized at higher conversions (Figures 4.6 and 4.7). As discussed earlier (Section 3.3.8), oxygen groups already present in this particular carbon were different on the surface than in the interior; this could be due to the difference of the carbon structure when they were formed. The oxygen surface groups formed upon oxidation are thus most likely different at the higher conversions. This is supported by the pH measurements. The pH value of a suspension of a carbon sample that was oxidized at 400 ° C for two hours after 42% gasification was slightly less acidic

than that of a fresh oxidized carbon (Table 3.5). However, the surface area of this sample is about 14 times larger than the fresh sample, and it is expected that if the same acidic groups were formed to the same extents on both surfaces then the pH of the suspensions would be at least one unit lower in the former case. This is not observed. The reason is probably the existence of still large amounts of the stable basic groups that did not oxidize during the oxidation period of two hours. The acidic groups on the surface formed during oxidation at 400 ° C coexist with basic groups that were already on the surface, thus giving the slightly acidic pH.

Some of the catalyst added at high conversions interacted with the basic groups and formed stable species which retained potassium to the end, similar to a 10 wt%-fresh degassed sample (Figures 5.13 and 5.14). The observation that the potassium content of a "10 wt%"-47% gasified-carbon sample after 3 hours of heating in helium at 865 ° C (lower open circle at 47% conversion in Figure 5.13), was the same as a 10 wt%-degassed sample after 47% gasification supports this idea that stable potassium surface complexes are formed with the basic groups, not with the groups introduced via oxidation at 400 ° C at these high conversions. The non-basic groups, on the other hand, formed catalyst species that were not stable but were active and were, in addition, different from those formed at the lower conversions. These species were responsible for the higher reaction rates of these samples. It should be noted that this enhancement is too large to be accounted for by just the enhancement of the uncatalyzed gasification and it indicates that the catalyst is definitely involved in this process.

The basic oxygen groups did not enhance the reactivity of the uncatalyzed carbon significantly, but it seems that in the presence of potassium carbonate they play an important role in the catalysis process. Perhaps, potassium

carbonate interaction with these groups destabilizes and desorbs the oxygen groups, generating active sites by a process similar to that of the non-basic oxygen groups in the uncatalyzed case.

It has already been shown that the reaction rate per unit surface area (specific reaction rate) of this particular carbon black maintains a fairly constant value after 20% conversion for 5 and 10 wt%-K_2CO_3 fresh carbon samples (Section 5.5.3.1). This can be explained in terms of interaction of the catalyst and the basic oxygen surface groups. As carbon is gasified and higher surface area is developed, more basic oxygen groups within the carbon are exposed. The newly exposed oxygen groups interact with the catalyst present on the surface and form the active intermediate species. Thus as more surface area is developed, active sites are generated and the specific reaction rates remain constant.

Fresh carbon samples that were not degassed or gasified prior to impregnation showed higher activity and better retention of potassium. As discussed earlier, the oxygen groups near the surface of this particular carbon were mainly C=O carbonyl groups that were lost upon degassing or gasification to high conversions. So it seems reasonable that the presence of these carbonyl groups and the higher reactivities are somewhat related. The interaction of the alkali carbonate and these groups to form a potassium surface oxide (C-O-K) definitely is a possibility. This surface oxide has already been shown to be stable at temperatures as high as 700 ° C and is directly proportional the reactivity of char samples in steam gasification [12]. Further evidence for the importance of the initially present non-basic oxygen groups is provided by careful comparison of Figures 5.13 and 5.18. The reaction rates of a 10 wt%-degassed carbon sample are very close to those of the 5 wt%-sample (Figure 5.18). However, the potassium content of the degassed sample is much higher up to 50% conversions,

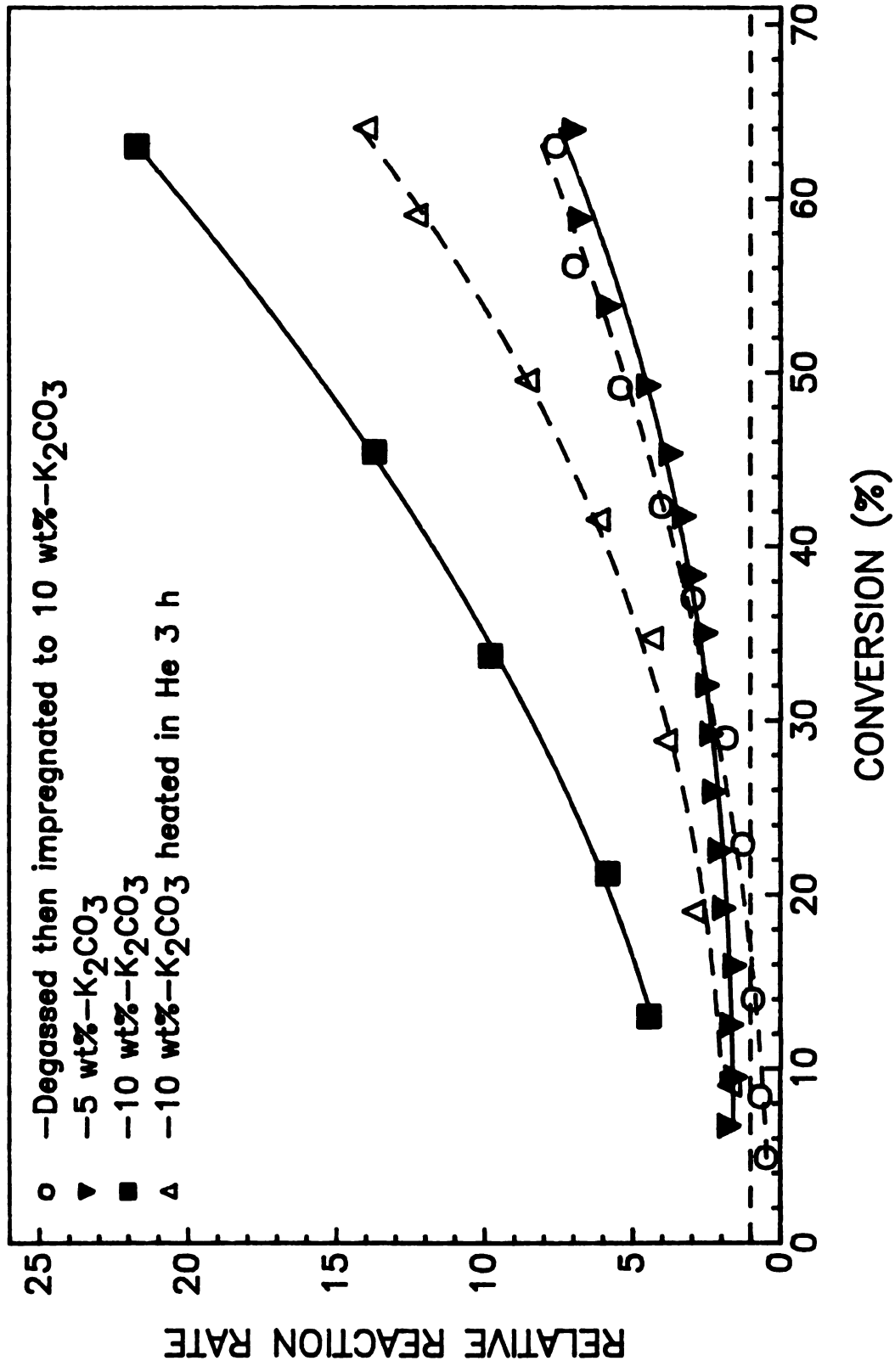

Figure 5.18 Relative gasification rates at 865 °C of heat-treated K_2CO_3-loaded carbons.

as can be seen in Figure 5.13. The immediate conclusion is that a large fraction of the catalyst is inactive in the degassed sample, because of the absence of the carbonyl groups.

When the severity of the heat treatment is reduced by heating an impregnated sample at 865 ° C for 3 h in helium, the reduction in reactivity is much less than the degassed sample (Figure 5.18). In this case the potassium loss is only 4% at the end of the heat treatment, which is not enough to account for the relatively large drop in reaction rate from that of the fresh impregnated carbon. In this less severe treatment fewer oxygen groups are lost and thus the reduction in reaction rate is less. It is worth mentioning that the potassium content in this case was between that of the fresh and the degassed samples throughout the reaction period.

The amount of oxygen lost as CO and CO_2 from the carbon samples during degassing at 1000 ° C was about four times higher than that during heating for three hours in helium at 865 ° C. But the loss in reactivity was not proportional to the oxygen losses (Figure 5.18). At present, this cannot be satisfactorily be explained, but a few speculations can be made. One speculation is that when the carbon sample is cleaned of most of its oxygen by degassing, the oxygen in the carbonate plays a larger role in the catalysis process. Another speculation is that a significant portion of the oxygen groups that were removed from the sample by degassing were inactive groups, probably ether groups. In either case, it can be said with confidence that not all the oxygen present in the carbon is involved in the catalysis process of the alkali carbonate, somewhat contrary to the results of some studies that claim the reactivity of a carbon sample is directly related to its oxygen content [27] or the oxygen trapped on its surface [156]. The involvement of other active sites and the oxygen in the carbonate in the catalysis process have already been proposed in the literature [159]. As

stated earlier, the results of the present study do not rule out the possibility of involvement of other active site that are not necessarily associated with oxygen. These results nevertheless suggest that most of the activities are associated with the oxygen groups.

The fact that surface oxygen groups play a significant role in K_2CO_3-catalysis of both steam gasification (oxidizing environment) and hydrogasification (reducing environment) strongly suggests that the dominating steps in the catalysis process are the interactions between the catalyst and carbon. The enhancement of reaction rates by oxygen surface groups are greater in the catalyzed case, implying that oxygen influences the interaction of K_2CO_3 with either carbon or reactant gases. If oxygen influences the interaction of the catalyst with carbon, then enhancement of the reactivity should be independent of the gaseous environment.

In contrast, if oxygen were to influence the interaction of the catalyst with reactant gas, then oxygen would have to interact with the catalyst or the reactant gas first. The interaction of reactant gas with intermediate species formed from interaction of the catalyst and oxygen surface groups would then be strongly dependent on the nature of the reactant gas; *i.e.*, if this intermediate were more reactive toward oxidizing gases, it would be less reactive toward reducing gases and vice versa. This is not observed; both steam and H_2 gas gasification rates are enhanced by presence of oxygen. On the other hand, if oxygen surface groups interact with reactant gas first to form surface complex(es) which further react with the catalyst, this complex would be expected to be similar to oxygen-hydrogen complexes formed during steam gasification. In this case this complex would readily decompose to CO and H_2 and thus methane formation rate would not be enhanced. Again, this is not observed.

Hence, it seems that oxygen plays a significant role in the interaction of the catalyst with carbon in K_2CO_3-catalyzed gasification of carbon. This suggests that the study of oxygen influence on K_2CO_3-catalysis of hydrogasification is a better choice to probe the intermediate steps because the sources of oxygen are limited to carbonate itself and oxygen impurities in the carbon. In steam or CO_2 gasification, there is a constant supply of oxygen to the carbon surface from the reactant gases and, therefore, it is more difficult to control the formation and the nature of oxygen groups thus formed and to follow oxygen through reaction sequences.

Chapter 6

Conclusions & Recommendations

The results of this study lead to some important conclusions on the role of oxygen surface complexes on alkali-catalyzed hydrogasification of carbon. However, there are still many unanswered questions, and some recommendations are thus made within the framework of the present study to resolve some of the relevant questions.

6.1 Conclusions

6.1.1 Uncatalyzed Hydrogasification

Based on the results of the study of influence of various oxygen complexes on hydrogasification rate of carbon black (in the absence of potassium carbonate) a mechanism is postulated. According to this mechanism, oxygen surface groups enhance the reactivity of the carbon toward hydrogen by generating 'nascent' active sites upon thermal decomposition into CO and CO_2, and not by the "electron transfer" mechanism. These 'nascent' active sites act as the sites for hydrogenation of the carbon surface.

It was found that oxygen complexes near surface of fresh and untreated carbon black Raven 16 are mainly carbonyl groups, and that oxygen complexes in the bulk of the carbon are dominantly basic. Carbonyl groups and acidic groups readily desorb from the surface and create the 'nascent' active sites and therefore are very active. In contrast, the basic groups, possibly chromene groups, are fairly stable and thus inactive.

As higher conversions are obtained, the carbonyl groups are lost from the carbon surface and thus many fewer active sites are generated, resulting in a sharp drop in the activity of the carbon surface. On the other hand, the total surface area of carbon particles increases drastically due to the development of a high degree of porosity, thus exposing the basic oxygen complexes in the carbon bulk. The low activity of the basic oxygen complexes and the high surface area together compensate for the effect of loss of carbonyl groups, hence the slow decrease of overall hydrogasification rate. In addition, prolong degassing desorbs the carbonyl groups and thermally anneals the 'nascent' active sites, resulting in significant loss in reactivity of carbon.

6.1.2 Alkali-Catalyzed Hydrogasification

Potassium carbonate is an effective catalyst (enhanced reaction rate 25 times for the 10 wt%-K_2CO_3 sample). However, there seems to be a minimum amount of potassium carbonate, between 1 wt% and 5 wt%, needed before any catalytic activity can be observed. The interaction of potassium carbonate, in excess of this minimum amount, with carbon involves a small fraction of the carbon surface area which reduces the carbonate to free alkali metal. Subsequent formation of active species generates active sites on the carbon surface in such a way that keeps the activity per unit surface area fairly constant. In the absence of K_2CO_3, the carbon surface is deactivated rapidly due to the thermal annealing and consumption of active sites. A significant portion of the potassium is lost during hydrogasification from carbon bed via vaporization (free potassium metal) or migration onto sample holder surface, but is retained in the reaction zone (on the surface of sample holder, quartz reactor lining or the tip of the exit tube).

The catalyst interacts with different oxygen surface groups to form intermediate species which vary in terms of activity and stability. The results lead to the conclusion that not all oxygen groups are involved in the catalysis process. The oxygen surface complexes that do participate in the catalysis have different activities depending on their natures. The interaction with C=O carbonyl groups forms stable and highly active species which are possible candidates for the formation of C-O-K surface groups. The basic oxygen surface complexes, on the other hand, interact with the catalyst and produce relatively unstable species that enhance hydrogen gasification. It is this formation of active species from basic oxygen groups, otherwise inactive, that is responsible for significant enhancement of hydrogenation rate at higher conversions.

In contrast, the interaction of acidic oxygen groups with the catalyst could not be well characterized and seems to depend on the conversion level or the structure of carbon surface. Probably, at different conversion levels, combustion fixes different proportions of carbonyl groups and various acidic groups which interact distinctively with the catalyst, resulting in a variety of observed hydrogenation rates.

Furthermore, potassium retention on the carbon surface and catalyst activation seem to be two distinctive phenomena. It is possible to retain potassium on the carbon surface without activating it.

Presence of K_2CO_3 does not seem to alter the course of the porosity development within carbon particles during hydrogasification, and the impurities such as sulfur and nitrogen do not seem to play any role in the catalysis.

6.2 Recommendations

There is some degree of speculation involved in the interpretation of the results reported in the present work, and further verification using other techniques is advisable. Here, it has been shown that, first, oxygen plays an important role in alkali-catalysis and, secondly, various oxygen groups on carbon surface have distinctive interactions with the carbon surface. These results provide a rather unique means for further studies of the influence of oxygen on alkali-catalysis.

Various oxygen surface groups should be introduced onto carbon surface by various techniques such as combustion or oxidation by nitric acid, followed by impregnation with potassium carbonate. These samples should then be heated in helium to reaction temperature. During the heat up, the carbonate

and oxygen surface groups will interact and form some intermediate species. The nature of these intermediate species can be probed by adapting a variety of techniques such as XPS and FTIR. Since intermediate species formed from different oxygen groups have different activities, these techniques should identify the active species and eventually reveal more information about the catalysis mechanism. These experiments should also be carried out in hydrogen at various levels of conversion to examine the effect of hydrogen on the interaction and also the effect of change in carbon surface structure. However, extreme care should be taken to avoid exposing samples to air before analysis, for after reaction the samples may readily interact with air even at room temperature (Section 5.5.2.1.1) to form oxygen surface groups which might interfere with the analysis of surface groups.

A knowledge of the nature of the most active intermediate species and the chemistry involved could perhaps lead to the development of a new processing method of coal or new additives so that the oxygen present in coal can be put into a more active form. Economic feasibility of such a processing cannot be evaluated at this point simply because it is not yet known what is involved and exactly what needs to be done.

Another recommendation is to investigate the phenomenon discussed in section 5.5.2.1.1 where some rather active intermediate species, which spontaneously react with air at room temperature, seem to be formed at moderate conversions. If this phenomenon is understood, perhaps after the initial high temperature gasification, the rest of the carbon can be gasified in steam (oxidizing environment) at much lower temperatures so that methane formation is more favored.

Appendix A

Appendix A

Reactor Design Calculations

Flange Design

The thickness of the flange ring can be calculated from Equation A-1 [69]

$$\varsigma_f^2 = -\frac{3P}{4\pi s \sigma_\theta}\left[2(s+1)(A' - lnU)+(s-1)\frac{A''}{U^2} - (s+3)\right] \quad \text{for } U = 1 \qquad \text{(A-1)}$$

where

$$A' = \frac{K_1^2}{K_1^2-1}\ln K_1 + \frac{1+3s}{2(1+s)}$$

$$A'' = \frac{2(1+s)K_1^2}{(s-1)(K_1^2-1)}\ln K_1$$

$$K_1 = \frac{r_1}{r_0}$$

$$\frac{1}{s} = Poisson's\ Ratio\ \mu$$

and

P = effective load, lb_f

σ_θ = tangential stress in plain ring, psi

r_1 = radius of bolt-circle, in

r_0 = inside radius of flange ring, in

ς_f = thickness of flange ring, in

weakest spot of the flange ring; *i.e.*, the spot at which tangential stress becomes equal to the yield strength of the material. Inside radius r_0 was taken to be equal to inside radius of the cylindrical reactor vessel which is 9/16". The bolt-circle radius was taken to be the distance from the center of the flange ring to the outer edge of the bolt holes. The σ_θ was set equal to yield stress of the alloy at room temperature which is 63000 psi [70]. The value of Poisson's ratio μ could not be found for this particular alloy and a value of 0.3 was used; the range of Poisson's ratio is limited between -1 and ½ [66] and varies from 0.25 to 0.42 for most metals and alloys [71]. The effective load P is the sum of gasket sealing stress, the weight of the reactor vessel and the stress due to internal hydrostatic pressure. The sealing stress can easily be calculated

$$\begin{aligned}\text{Sealing stress} &= \text{O-ring perimeter} \times \text{sealing stress per inch of O-ring} \\ &= 13/8" \times \pi \times 100 \text{ lb}_f \\ &= 511 \text{ lb}_f\end{aligned}$$

The stress due to internal hydrostatic pressure is calculated from

$$\begin{aligned}\text{Internal pressure stress} &= \text{O-ring inside area} \times \text{inside pressure} \\ &= (1¼"/2)^2 \times \pi \times 1100 \text{ psi} \\ &= 1350 \text{ lb}_f\end{aligned}$$

where a safety factor of 10% is included for the operating pressure inside the reactor. The weight of the reactor can be estimated by assuming a solid rod of 2" OD × 40" long as the reactor

$$\text{weight stress} = \text{solid rod volume} \times \text{alloy density}$$

$$= (2"/2)^2 \times \pi \times 40" \times 0.330\ \mathrm{lb}_m/\mathrm{in}^3$$

$$= 41.5\ \mathrm{lb}_f$$

where the density is 0.330 $\mathrm{lb_m/in^3}$ [70]. The sum P of all of the above stresses is equal to 1900 lb_f and is a fairly conservative approximation. Substitution of the appropriate values into Equation A-1 yield the required thickness of flange ring:

$$K_1 = \frac{7/4"}{7/16"} = 4$$

$$A' = \frac{4^2}{4^2-1}\ln 4 + \frac{1+3(\frac{1}{0.3})}{2(1+\frac{1}{0.3})}$$

$$= 2.75$$

$$A'' = \frac{2(1+\frac{1}{0.3})4^2}{(\frac{1}{0.3}-1)(4^2-1)}\ln 4$$

$$= 5.49$$

$$\varsigma_f^2 = \frac{3(1900\ lb_f)}{4\pi(\frac{1}{0.3})(63000\ psi)}\left[2(\frac{1}{0.3}+1)(2.75-ln\,1)+(\frac{1}{0.3}-1)(\frac{5.49}{1^2})-(\frac{1}{0.3}+3)\right]$$

$$= 0.0655\ in^2$$

$$\therefore \quad \varsigma_f = 0.256"$$

The thickness of the flange ring is not very sensitive to the magnitude of Poisson's ratio μ; the thickness varies from 0.244" to 0.267" when Poisson's ratio is varied from 0.1 to 0.5, respectively. Thus it is decided to use a plain ring flange of ½" thickness, which is operated quite safely after introducing several conservative assumptions discussed above.

The deflection of the flange ring under the applied stress is calculated from Equation A-2 [69]

$$y = \frac{3(s^2-1)Pr_0^2}{2\pi s^2 E \zeta_f^3}\left[A'\,(K_1^2-1)-(K_1^2\,A'')lnK_1\right] \qquad \text{(A-2)}$$

where E is Young's modulus of elasticity and y is deflection of flange ring.

The Young's modulus of elasticity E for Haynes-25 alloy at room temperature is 34.2×10^6 psi [70]. Substitution of appropriate values into Equation A-2 yields

$$y = \frac{3((\frac{1}{0.3})^2-1)\ 1900\ lb_f\ (\frac{7"}{16})^2}{2\pi(\frac{1}{0.3})^2(34.2\times10^6\ psi)(½")^3}\left[2.75(4^2-1)-(4^2-5.49)ln\,4\right]$$

$$= 0.00098"$$

The thickness and the deflection under stress of the cover disk is calculated similarly using Equations A-1 and A-2; but, in this case the diameter of the hole at the center of the disk, for mounting a Conax fitting needed for insertion of thermocouples into sample bed, is only ½". The yield strength and Young's modulus of elasticity for stainless steel 316 are 30000 psi and 28×10^6 psi, respectively [70]. The calculated disk thickness is 0.611". A 1"-thick cover disk is used for which the deflection under stress is found to be 0.00014".

Thermal Stresses

Temperature Profile

The temperature profile can be derived by solving Equation 2-5 subject to two boundary conditions

$$\frac{d}{dz}(\kappa\frac{dT}{dz}) = 0 \tag{A-3}$$

T = room temperature T_m, 77 °F at $z = 0$

T = furnace temperature T_f at $z = L$

The value of L is set to 9" and Equation A-3 is solved by integrating both sides of the equation w.r.t. z to yield

$$\kappa\frac{dT}{dz} = q \tag{A-4}$$

where q is the constant of integration and by definition is the negative of axial heat flux in the reactor wall. The thermal conductivity κ as a function of T [64] is substituted in the above equation and both sides are integrated again

$$\int_{T_m}^{T_f} \kappa dT = \int_0^L q dz \tag{A-5}$$

where

$$\kappa = 59.06 + 0.0761\,T, \text{ Btu-in/(ft}^2\text{-h-}^\circ\text{F)}$$

and solving for q yields

$$q = \frac{59.06(T_f) + \frac{0.0761}{2}(T_f^2 - T_m^2)}{L} \tag{A-6}$$

For a furnace temperature T_f of 1832 °F (1000 °C) the final temperature profile, the temperature gradient and the heat flux q are

$$T = -776 + 852.9\sqrt{1+8.35\frac{z}{L}} \tag{A-7}$$

$$\frac{dT}{dz} = \frac{3561}{\sqrt{1+8.35\frac{z}{L}}} \tag{A-8}$$

$$q = \frac{2.307\times10^5}{L} \tag{A-9}$$

respectively.

For a cooling length of 9" the temperature gradient varies from a maximum of 395 °F/in at the cooling coils site (z=0) to 129 °F/in at the furnace inlet (z=L) and the heat flux q is 178 Btu/in^2-h.

Shear Strain

The thermal expansion coefficient α by definition is

$$\alpha = \frac{1}{V}\frac{dV}{dT} \tag{A-10}$$

where V is the volume of the control volume under study. Consider a cylindrical shell of a very small thickness Δr and length Δz with radius r and located at point z along the reactor z-axis as the control volume (cylindrical coordinate). The volume of this control element is then $2\pi r \Delta r \Delta z$. Substitution into Equation A-10 then gives

$$\alpha = \frac{1}{r}\frac{dr}{dT} + \frac{1}{\Delta r}\frac{d\Delta r}{dT} + \frac{1}{\Delta z}\frac{d\Delta z}{dT} \tag{A-11}$$

In cartesian coordinates with a control volume of Δx^3, Equation A-10 reduces to

$$\alpha = \frac{3}{\Delta x}\frac{d\Delta x}{dT} \tag{A-12}$$

Thus if it is assumed that thermal expansion in the z direction is not influenced by thermal expansion in other directions, then the last term on the right hand side of Equation A-11 can be replaced by above equation. Since the reactor wall is thick it can also be assumed that the first two terms on the right hand side are equal in magnitude (assume a solid cylinder). Then Equation A- 11 yields

$$\frac{dr}{dT} = \frac{r\alpha}{3} \tag{A-13}$$

Therefore, the shear strain can be estimated by substituting Equation A-8 and the above equation into Equation 2-4

$$\frac{dr}{dz} = \frac{r\alpha}{3} \frac{3561}{\sqrt{1+8.35\frac{z}{L}}} \tag{A-14}$$

From this equation it can be seen that the points of maximum strain are the points on the outside of the reactor wall at the site of cooling coils (r_o,0). At these points the modulus of elasticity G is also a maximum and because E is a maximum over the temperature range of interest and μ is fairly constant with temperature, [73]

$$G = \frac{E}{2(1+\mu)} \tag{A-15}$$

Cooling Coils

The heat flux inside the reactor wall calculated from Equation A-9 is 178 Btu/in^2-h. The heat duty Q of the cooling coils is calculated by multiplying the heat flux q and the cross sectional area A_{rw} of the reactor wall:

$$Q = q \times A_{rw} \tag{A-16}$$

$$= 178\frac{Btu}{in^2\text{-}h} \times \pi \left[\left(\frac{2"}{2}\right)^2 - \left(\frac{7/8"}{2}\right)^2 \right]$$

$$= 452\frac{Btu}{h}$$

The cooling water flow rate is then calculated from an energy balance on cooling water with heat capacity C_p and mass flow rate m and a temperature rise ΔT_c of 10 ° F:

$$m = \frac{Q}{C_p \Delta T_c} \tag{A-17}$$

$$= \frac{452\ Btu/h}{(1\ Btu/lb_m - °F) \times 10\ °F}$$

$$= 49.7\ \frac{lb_m}{h}$$

where heat capacity of cooling water is taken as 1 Btu/lb_m- ° F.

Mass flux $\dot{m}$ inside the cooling coils is then calculated by dividing the mass flow rate m by the internal cross sectional area A_c of ¼" OD copper cooling coils

$$\dot{m} = \frac{m}{A_c} \tag{A-18}$$

$$= \frac{49.7\ lb_m/h}{\pi(\frac{5/32"}{2})^2}$$

$$= 2592\ lb_m/in^2{-}h$$

where inside diameter d of copper cooling coils is 5/32". The Reynolds number R_e is then calculated from the following equation

$$R_e = \frac{d\dot{m}}{\mu_v} \tag{A-19}$$

$$= \frac{5/32\ in \times 2592\ lb_m/in^2{-}h}{0.1916\ lb_m/in{-}h}$$

$= 2114$

where the viscosity of the cooling water μ_v at 75 ° F is 0.95 centipoise or 0.1916 lb_m/in-h.

This value of R_e is in the region between laminar and turbulent regimes [74]. However, this required cooling water velocity inside the cooling coils is only about 1.65 ft/s which is much lower than what is obtained in practice and thus the actual value of R_e during operation is somewhat higher than the above value. Hence, the flow regime can be assumed to be turbulent so that a more realistic estimation of the heat transfer coefficient h_o can be obtained. The heat transfer coefficient for turbulent flows inside a circular tube is calculated from the following equation [74]

$$h_o = 0.023\frac{\kappa_c}{d}\left[1+\left(\frac{d}{L_{cc}}\right)^{0.7}\right]R_e^{0.8}\left(\frac{C_p\mu_v}{\kappa_c}\right)^{1/3} \qquad \text{(A-20)}$$

where L_{cc} is the length of cooling coils and κ_c is the thermal conductivity of cooling water which is 0.349 Btu/ft-h-° F at 75 ° F. Generally, a velocity of 3 ft/s for the fluid velocities in heat exchangers is assumed and thus this value is used for cooling water velocity inside cooling coils. This yields values of 4710 lb_m/in^2-h and 3840 for $\dot{m}$ and R_e, respectively; the temperature rise of cooling water is reduced from 10 ° F to 5.5 ° F. As a first approximation, assume a ratio L_{cc}/d of greater than 50, so that the first bracket in the above equation can be ignored. Substituting appropriate values into the equation to find h_o;

$$h_o = 0.023\left(\frac{0.349\ \frac{Btu}{ft-h-{}^\circ F}}{(\frac{5"}{32})(\frac{1\ ft}{12"})}\right)(3840)^{0.8}\left(\frac{1\ \frac{Btu}{lb_m-{}^\circ F}\times 2.30\ \frac{lb_m}{ft-h}}{0.349\ \frac{Btu}{ft-h-{}^\circ F}}\right)^{1/3}$$

$$= 852 \frac{Btu}{ft^2\text{–}h\text{–}{}^\circ F}$$

The temperature difference driving force ΔT in turbulent regime is taken to be equal to the log-mean temperature differences ΔT_{ln} [74]

$$\Delta T_{ln} = \frac{(T-T_i)-(T-T_o)}{\ln\frac{T-T_i}{T-T_o}} \tag{A-21}$$

$$= \frac{(85\ ^\circ F-75.5\ ^\circ F)-(85\ ^\circ F-70\ ^\circ F)}{\ln\frac{(85\ ^\circ F-75.5\ ^\circ F)}{(85\ ^\circ F-70\ ^\circ F)}}$$

$$= 12\ ^\circ F$$

where it is assumed that the temperature of cooling coil wall is constant and uniform even though heat is transferred only from the side that is soldered to the reactor wall and not from the sides that are exposed to air; *i.e.*, all of the tube surface area of cooling coils is available for heat transfer. This assumption is valid since copper has very high thermal conductivity and, in addition, the copper tubes used were thick-walled.

The total heat transfer surface area A is then calculated from Equation A-22

$$A = \frac{Q}{h\,\Delta T_{ln}} \tag{A-22}$$

$$= \frac{452\ Btu/h}{(852\ Btu/ft^2\text{–}h\text{–}{}^\circ F)\times(12\ ^\circ F)}$$

$$= 0.0442\ ft^2$$

The length of cooling coils L_{cc} is then calculated from Equation A-23

$$L_{cc} = \frac{A}{\pi d} \tag{A-23}$$

$$= \frac{0.0442\ ft}{\pi \times (\frac{5"}{32})(\frac{1\ ft}{12"})}$$

$$= 1.08\ ft$$

This length of cooling coil corresponds to about 2 laps of copper tubing around the outside of the reactor. It is decided to use 6 laps of cooling coils.

After the construction of the reactor the actual cooling water velocity was measured and was found to be about 2 ft/s as opposed to the value of 3 ft/s that is used in Equation A-20. Thus the actual value of R_e is 2560 and the corresponding temperature rise of cooling water is about 8.3 °F. This yields a value of 616 Btu/ft^2-h-°F for h_o from Equation A-20 and 10.3 °F for ΔT_{ln} from Equation A-21. Values of 0.071 ft^2 and 1.74 ft are obtained for A and L_{cc}, respectively. Thus only 3.5 laps of copper cooling coils are needed for the actual operation.

γ-Ray Detection System

γ-Ray Absorption

There are 6" of fire-bricks, two iron sheets of 1/16" thickness, 9/16" of Haynes-25 alloy, 0.5" hydrogen gas and 6" of air between the detector crystal and a sample at the reaction site inside the reactor. The detector is "focused" on the reaction site by inserting at least 6" of lead bricks between the detector crystal and the areas around the sample (Figure 2.3). The extent of absorption of the γ-rays by these shielding materials is calculated from the attenuation coefficients Λ in Table 2.3 and Equation 2-20 which can be rearranged to

$$\frac{I}{I_o} = e^{-\Lambda x} \tag{A-24}$$

Substitution of Λ's from Table 2.3 and above mentioned thicknesses into the above equation yields

$$\frac{I}{I_o}\Big|_{iron} = e^{-(0.380\ cm^{-1})(\frac{2.54\ cm}{1"})(2\times 1/16")}$$

$$= 0.886$$

$$\frac{I}{I_o}\Big|_{fire-brick} = e^{-(0.025\ cm^{-1})(\frac{2.54\ cm}{1"})(6")}$$

$$= 0.683$$

$$\frac{I}{I_o}\Big|_{Haynes-25} = e^{-(0.416\ cm^{-1})(\frac{2.54\ cm}{1"})(9/16")}$$

$$= 0.552$$

$$\frac{I}{I_o}\Big|_{lead} = e^{-(0.578\ cm^{-1})(\frac{2.54\ cm}{1"})(6")}$$

$$= 0.000135$$

$$\frac{I}{I_o}\Big|_{air} = e^{-(0.0000513\ cm^{-1})(\frac{2.54\ cm}{1"})(6")}$$

$$= 1.001$$

Above calculations show that γ-ray absorption by air or hydrogen is negligible and 6" of lead shielding is effective for "focusing" the detector. The overall absorption by shieldings between the detector and the sample can now be calculated by rearranging Equation 2-26 and using Equation 2-27:

$$f_I = \frac{I}{I_o}\Big|_{overall} = \frac{I}{I_o}\Big|_{iron} \times \frac{I}{I_o}\Big|_{fire-brick} \times \frac{I}{I_o}\Big|_{Haynes-25} \qquad \text{(A-25)}$$

$$= 0.886 \times 0.683 \times 0.552$$

$$= 0.334$$

Thus only 33.4% of the γ-rays emitted from a sample at the reaction site inside the reactor will pass through the shielding materials between the detector crystal and the sample.

Sample Activity

The radiation rate I_o from a sample or nuclear disintegration rate $\overline{R}$ is then calculated by taking into account the geometric factor f_d (Eq. 2-28), the detector efficiency ψ for γ-rays and the fraction f_I of the radiation passing through the shielding materials. The desired counting rate is ten times the background counting rate of 5-6 cps and thus the disintegration rate $\overline{R}$ is calculated by modifying Equation 2-29:

$$\overline{R} = \frac{60\ cps}{0.18\psi f_d f_I} \tag{A-26}$$

The factor 0.18 in the denominator is to account for the fact that only 18% of the nuclear disintegrations yield 1.525 MeV γ-rays. Substitution of the appropriate values of f_d from Equation 2-28, f_I from Equation A-25 and a value of 5% for the detector efficiency in the above equation yields

$$\overline{R} = \frac{60\ cps}{0.18\times0.05\times0.0051\times0.334}$$

$$= 3.91\times10^6\ cps$$

$$= 106\ \mu Ci$$

Sample Activation

Once the desired level of radiation and the amount of potassium in a sample are known, the activation time t_a is calculated from Equations 2-13 and 2-14. The maximum allowable level of activity for a sample however is limited to only 100 μCi by Office of Radiation, Chemical and Biological Safety at Michigan State University. Thus for 60 mg of a 10 wt%-K_2CO_3 sample the number of atoms of ^{41}K is

$$N_o^{41} = \frac{0.060\ g \times 10\% \times \frac{0.565\ g\ K}{1\ g\ carbonate} \times \frac{0.069\ g\ ^{41}K}{1\ g\ K}}{\frac{41\ g\ ^{41}K}{1\ mol\ ^{41}K}} N_{avo}$$

$$= 3.44 \times 10^{18}\ atoms$$

Combining Equations 2-13 and 2-14 and solving for t_a yields

$$t_a = -\frac{1}{\epsilon} \ln \left(1 - \frac{\overline{R}}{N_o^{41} \eta \Phi} \right) \tag{A-27}$$

For a Neutron flux Φ of 10^{12} and a cross section η of 1.5×10^{-24} cm^2, above equation yields

$$t_a = -\frac{1}{0.056\ h^{-1}} \ln \left(1 - \frac{3.91 \times 10^6\ cps}{(3.44 \times 10^{18}\ atoms)(1.5 \times 10^{-24}\ cm^2/atom)(10^{12} neutrons/cm^2\text{—}s)} \right)$$

$$= 25.3\ h$$

For such small samples a neutron flux of 10^{13} is used instead which reduces the activation time to 1.41 h or 84 min.

Rupture Disc Sizing

To size the rupture disc it is necessary to determine if the flow through the ruptured disc is sonic or subsonic and then the gas flow rate Q_v (SCFM) and area A_{rd} is calculated [82]. The flow through ruptured disc is sonic if

$$\frac{p_e}{p} \leq \left(\frac{2}{k+1}\right)^{\frac{k}{k-1}} \tag{A-28}$$

where k is the ratio of specific heats and p_e is the exhaust pressure [82]. For hydrogen gas k is equal to 1.41 [82] and if the exhaust pressure p_e is taken to be atmospheric, for a stamped burst pressure of 1450 psi the flow will be sonic flow:

$$\frac{14.7\ psi}{1450\ psi} = 0.0101 < \left[\frac{2}{1.41+1}\right]^{\frac{1.41}{1.41-1}} = 0.527$$

The gas flow constant C for sonic flow is then calculated from the following equation [82]

$$C = \frac{520}{3600}\left[k\left(\frac{2}{k+1}\right)^{\frac{k+1}{k-1}}\right]^{\frac{1}{2}} \tag{A-29}$$

$$= \frac{520}{3600}\left[1.41\left(\frac{2}{1.41+1}\right)^{\frac{1.41+1}{1.41-1}}\right]^{\frac{1}{2}}$$

$= 0.09915$

For sonic flow the area A_{rd} and volumetric flow rate Q_v are related to each other [82]

$$A_{rd} = \frac{Q_v}{22772KpC}\sqrt{W_H(T_m + 460)} \tag{A-30}$$

where K is a constant set to 0.62 by ASME Code regarding rupture discs and W_H is molecular weight of hydrogen gas. Substitution of appropriate values into the above equation yields

$$A_{rd} = \frac{Q_v}{22772\times0.62\times1450\ \psi\times0.09915}\sqrt{2.016\ \frac{g}{mole}\ (77\ ^\circ F + 460)}$$

$$A_{rd} = 1.62\times10^{-5}\ Q_v$$

The smallest size Fike Prebulged rupture disc is ½" in diameter and the maximum gas flow rate through this rupture disc is then calculated from the above equation

$$Q_v = \frac{\left(\frac{½"}{2}\right)^2\pi}{1.62\times10^{-5}} \tag{A-31}$$

$= 12120\ SCFM$

Thus for a full 250 ft^3 and 2500 psi hydrogen gas cylinder it takes 1.5 minutes to reduce the gas cylinder pressure to 1450 psi by venting through the rupture disc to atmosphere, assuming that the 1/8" tubing upstream from the rupture disc does not limit the flow from the cylinder to the rupture disc. In reality, in case of pressure regulator failure or misadjustment, the flow in the 1/8" tubing will be a sonic flow and will be less than the sonic flow through the rupture disc. This implies that the reactor will be safe from any over pressurizing by gas cylinders.

For Fike Conventional Prebulged rupture discs the recommended ratio of operating pressure to burst pressure is 70% [82]. This implies that for an operating pressure of 1000 psi the rupture disc burst pressure should be at least 1430 psi. On the other hand, the ASME Code for the case where a rupture disc device is used as the primary or sole relieving (as is the present case) requires that rupture disc burst pressure not to exceed the maximum allowable working pressure (MAWP) [82]. Thus the reactor should be operated at a temperature such that MAWP is higher than the burst pressure; *i.e.*, MAWP should be at least 1448 psi which is the stamped burst pressure of the purchased ½" rupture disc.

The reactor is originally designed for a MAWP of 1100 psi at 1000 °C using Barlow's formula (Equation 2-1). When MAWP is set to 1448 psi, the operating temperature of the reactor vessel should be reduced to a limit where the rupture disc fractures before the reactor is damaged. To this end, the normal tensile and compressive stresses in the reactor wall have to be calculated for an internal presure p of 1450 psi and then be coupled with thermal shear stresses. The resulting overall maximum normal stresses σ_{max} calculated from Mohr's circles will determine the maximum allowable operating temperature.

The normal tensile and compressive stresses are calculated from Equations 2-7 through 2-9. The thermal shear stresses are assumed to have the same magnitude as those at 1000 °C operating temperature (Table 2.1). The Mohr's circle results indicate that σ_{max} is equal to 2136 psi and 1737 psi at (r_i, L) and (r_o, L), respectively. The rupture stress $\sigma_{rupture}$ in 10000 h is about 2140 psi at 970 °C and 2650 psi at 950 °C

[64]. Therefore, an operating temperature of 950 ° C or lower is quite safe.

This temperature is very close to the original designed temperature of 1000 ° C for a MAWP of 1100 psi. The reason is that the original design was based on Barlow's design formula (Equation 2-1) which is more on the safe side than the Lamé's formula which is used for the above analysis.

LIST OF REFERENCES

LIST OF REFERENCES

[1] Seglin, L., R. Geosits, B. R. Franko, and G. Gruber, *ACS Adv. Chem. Ser.* **146**, 1 (1975).

[2] Gruber, G., *Ibid*, 31.

[3] Tessi du Montay, C. M., and C. R. Marechal, *British Patent No. 2548* (1867).

[4] Tomita, Akira and Yasuhatsu Tamai, *J. Cata.* **27**, 293 (1972).

[5] Tomita, A. and Y. Tamai, *J. Phys. Chem.* **78**, 2254 (1974).

[6] Tomita, A., N. Sato and Y. Tamai, *Carbon* **12**, 143 (1974).

[7] McKee, D. W., *Ibid*, 453.

[8] Nahas, N. C., *Fuel* **62**, 239 (1983).

[9] Kubiak, H., H. J. Schroter, A. Sulimma and K. H. van Heek, *Ibid*, 242.

[10] Huttinger, Klaus J. *Ibid*, 166.

[11] Mims, C. A. and J. K. Pabst, *ACS Div. Fuel Chem. Prepr.* **25(3)**, 263 (1980).

[12] Mims, C. A. and J. K. Pabst,*Fuel* **62**, 176 (1983).

[13] Juntgen, Harald, *Fuel* **62**, 234 (1983).

[14] Huttinger, Klaus J. and R. Minges, *Fuel* **65**, 1122 (1986).

[15] McKee, D. W. and D. Chatterji, *Carbon* **13**, 381 (1975).

[16] McKee, D. W. and D. Chatterji, *12th Biennial Conference on Carbon* pp. 189-191, Pittsburgh, Pennsylvania (1975).

[17] McKee, D. W. and D. Chatterji, *Carbon* **16**, 53 (1978).

[18] McKee, D. W., C. L. Spiro, P. G. Kosky and E. J. Lamby, *Fuel* **62**, 218 (1983).

[19] Veraa, M. J. and A. T. Bell, *Ibid* **57**, 194 (1978).

[20] Huttinger, K. J. and R. Minges, *Ibid* **65**, 1112 (1986).

[21] Mims, C. A. and J. K. Pabst, *Proc. Int. Conf. on Coal Science*, pp. 730-736, Verlag Gluckauf GmbH, Essen (1981).

[22] Mims, C. A., K. D. Rose, M. T. Melchior and J. K. Pabst, *J. Am. Chem. Soc.* **104**, 6886 (1982).

[23] Yuh, S. J., and E. E. Wolf, *Ibid* **63**, 1604 (1984).

[24] Wood, B. J., R. H. Fleming and H. Wise, *Ibid* **63**, 1600 (1984).

[25] Wood, B. J., R. D. Brittain and K. H. Lau, *Carbon* **23**, 73 (1985).

[26] Long, F. J., and K. W. Sykes, *J. Chim. Phys.* **47**, 361 (1950).

[27] Saber, J. M., J. L. Falconer and L. F. Brown, *Ibid* **65**, 1356 (1986).

[28] Wen, W. Y., *Cata. Rev. Sci. Eng.* **22**, 1 (1980)

[29] Wigmans, T., H. Haringa and J. A. Moulijn, *Fuel* **62**, 186 (1983).

[30] Wigmans, T., J. vanDoorn and J. A. Moulijn, *Ibid* **62**, 190 (1983).

[31] Freriks, I. L. C., H. M. H. vanWechem, J. C. M. Stuiver and R. Bouwman, *Ibid* **60**, 465 (1981).

[32] Yuh, S. J., and E. E. Wolf, *Ibid* **62**, 252 (1983).

[33] Cerfontain, M. B. and J. A. Moulijn, *Ibid* **62**, 256 (1983).

[34] Sancier, K. M., *Ibid* **62**, 331 (1983).

[35] Sancier, K. M., *ACS Div. Fuel Chem. Prepr.* **28(1)**, 62 (1983)

[36] Huffman, G. P., F. E. Huggins, R. G. Jenkins, A. Piotruswski, F. W. Lytle and R. B. Greegor, *Fuel* **65**, 1339 (1986).

[37] Wood, R. E. and G. R. Hill, *ACS Div. Fuel Chem. Prepr.* **17(1)**, (1972).

[38] Gardner, N., E. Samuels and K. Wilks, *Adv. Chem. Ser.* **131**, 217 (1974).

[39] Cao, J. R. and M. H. Back, *Carbon* **23**, 141 (1985).

[40] Blackwood, J. D., *Ibid* **12**, 14 (1959).

[41] Hashimoto, K., K. Miura, J. J. Xu and A. Watanabe, *Chem. Lett.* **5**, 555 (1985).

[42] Sams, D. A., Tevan Talverdian and F. Shadman, *Fuel* **64**, 1208 (1985).

[43] Kolthoff, I. M., *J. Am. Chem. Soc.* **54**, 69 (1932).

[44] Villars, D. S., *Ibid* **69**, 214 (1947).

[45] Villars, D. S., *Ibid* **70**, 3655 (1948).

[46] Studebaker, M. L., E. W. D. Huffman, A. C. Wolfe and L. G. Nabors, *Ind. Eng. Chem.* **48**, 162 (1956).

[47] Boehm, H. P., E. Diehl, W. Heck and R. Sappok, *Angew. Chem. Inter. Edit.* **3(10)**, 669 (1964).

[48] Voll, M. and H. P. Boehm, *Carbon* **9**, 481 (1971).

[49] Studebaker, M. L. and R. W. Rinehart Sr., *Rubb. Chem. Tech.* **45**, 106 (1972).

[50] Barton, S. S., G. L. Boulton and H. Harrison, *Carbon* **10**, 395 (1972).

[51] Puri, B. R., D. D. Singh, J. Nath and L. R. Sharma, *Ind. Eng. Chem.* **50**, 1071 (1958).

[52] Puri, B. R. and R. C. Bansal, *Carbon* **1**, 457 (1964).

[53] Barton, S. S., D. Gillespie and B. H. Harrison, *Ibid* **11**, 649 (1973).

[54] Garten, V. A., D. E. Weiss and J. B. Willis, *Aust. J. Chem.* **10**, 309 (1957).

[55] Barton, S. S. and B. H. Harrison, *Carbon* **13**, 283 (1975).

[56] King, A., *J. Chem. Soc.* 1937, p. 1489.

[57] Garten, V. A. and D. E. Weiss, *Aust. J. Chem.* **8**, 68 (1955).

[58] Garten, V. A. and D. E. Weiss, *Ibid* **10**, 309 (1957).

[59] Walker Jr., P. L. and J. Janov, *J. Coll. Inter. Sci.* **28**, 449 (1968).

[60] Dubinin, M. M., *Carbon* **18**, 355 (1980).

[61] Gray, H. R.,"*Testing for Hydrogen Environment Embrittlement: Experimental Variables,*" *ASTM Special Technical Publication 543*, pp. 133-151, Los Angeles, Calif., 25-30 June 1972.

[62] Chandler, W. T. and R. J. Walter, *Ibid*, pp. 170-197.

[63] Bhattacharyya, S., E. J. Vesely, Jr. and V. L. Hill, *J. Materials for Energy Systems* **3(4)**, 12 (1982).

[64] Simmons, Ward F. and Howard C. Cross,"*The Elevated-Temperature Properties of Selected Super-Strength Alloys*," ASTM *Special Technical Report No. 160*, pp. 20 and 133-142 (1954).

[65] Seely, Fred B. and James O. Smith,"*Advanced Mechanics of Materials*," 2nd ed., Chapter 10, John Wiley & Sons, New York, N.Y. (1952).

[66] *Ibid*, pp. 69 and 220-228.

[67] Waters, E. O., D. B. Wesstrom, D. B. Rossheim and F. S. G. Williams, *A.S.M.E. Transactions, FSP-59-4* **59**, 161 (1937).

[68] Private communication with the manufacturer.

[69] Waters, Everett O. and J. Hall Taylor, *Mech. Eng.* **49**, 531 (1927)

[70] Perry, Robert H. and Cecil H. Chilton,"*Chemical Engineers' Handbook*," 5th ed., pp. **23**-38-**23**-53, McGraw-Hill Book Co., N.Y. (1973).

[71] Baumeister, T., E. A. Avallone and T. Baumeister III,"*Marks' Standard Handbook for Mechanical Engineers*," 8th ed., pp. **5**-5 and **6**-11, McGraw- Hill Book Co., N.Y. (1978).

[72] Seely, Fred B. and James O. Smith,"*Advanced Mechanics of Materials*," 2nd ed., pp. 49-67, John Wiley & Sons, New York, N.Y. (1952).

[73] Dieter Jr., George E.,"*Mechanical Metallurgy*," p. 36, McGraw Hill Book Company Inc., New York, 1961.

[74] McCabe, W. L. and J. C. Smith,"*Unit Operations of Chemical Engineering*," 3rd ed., pp. 312-320, McGraw Hill Book Company, New York, N.Y. (1976).

[75] Bird, R. B., Warren E. Stewart and Edwin N. Lightfoot,"*Transport Phenomena*," pp. 317-319, John Wiley & Sons, Inc., New York, N.Y. (1960).

[76] Lederer, C. M. and V. S. Shirely,"*Table of Isotopes*," 7th ed., pp. 101-102, John Wiley & Sons Inc., New York, N.Y., 1978.

[77] Chase, G. D. and J. L. Rabinowitz,"*Priciples of Radioisotope Methodology*," 2nd ed., pp. 136-152, Burgess Publishing Co., Minneapolis, MN 1965.

[78] Office of Radiation, Chemical and Biological Safety,"*Radiation Safety Study Guide*," pp. 56-58, Michigan State University, East Lansing, MI, 1982.

[79] Lamarsh, John R.,"*Introduction to Nuclear Engineering*," pp. 75-87, Addison-Wesley Publishing Co., 1975.

[80] Private communication with the manufacturere.

[81] Supelco Inc., *GC Bulletin 760C*, pp. 2-4, 1983.

[82] Fike Metal Products Corporation, *Catalog No. 7888,"Rupture Discs, Explosion Vents & Other Pressure Relief Devices,"* 1983.

[83] Brunauer, Stephen, P. H. Emmett and Edward Teller, *J. Am. Chem. Soc.* **60**, 309 (1938).

[84] Pierce, Conway and Bland Ewing, *J. Phys. Chem.* **68**, 2562 (1964).

[85] Ladd, W. A. and M. W. Ladd, *Rubb Chem. Tech.* **34**, 697 (1961).

[86] Donnet, J. B. and J. C. Bouland, *Rev. Gen. Caoutchouc* **41**, 407 (1964).

[87] Emmett, P. H. and Martin Cines, *J. Phys. Coll. Chem.* **51**, 1329 (1947).

[88] Anderson, R. B. and P. H. Emmett, *J. Appl. Phys.* **19**, 367 (1948).

[89] Janzen, Jay and Gerard Kraus, *Rubb. Chem. Tech.* **44**, 1287 (1971).

[90] Klyne, R. A., B. D. Simpson and M. L. Studebaker, *Ibid* **46**, 192 (1973).

[91] Pausch, J. B. and C. A. McKalen, *Ibid* **56**, 440 (1983).

[92] de Boer, J. H., B. G. Linsen, Th. van der Plas and G. J. Zondervan, *J. Catal.* **4**, 649 (1965).

[93] Voet, A., T. G. Lamond and D. Sweigart, *Carbon* **6**, 707 (1968).

[94] Smith, W. R. and G. A. Kasten, *Rubb. Chem. Tech.* **43**, 960 (1970).

[95] Lamond, T. G. and C. R. Price, *J. Coll. Interf. Sci.* **31**, 104 (1969).

[96] Turkdogan, E. T., R. G. Olsson and J. V. Vinters, *Carbon* **8**, 545 (1970).

[97] Lamond, T. G. and H. Marsh, *Carbon* **1**, 281 (1964).

[98] Heckman, F. A., *Rubb. Chem. Tech.* **37**, 1245 (1964).

[99] Walker Jr., P. L., *American Scientist* **50**, 259 (1962).

[100] Riley, H. L., *Chem. & Ind.* **58**, 391 (1939).

[101] Bisco, J. and B. E. Warren, *J. Appl. Phys.* **13**, 364 (1942).

[102] Hofmann, A. R., G. Rudorff, R. Holst, W. Ruston, A. Russ, and G. L. Ruess, *Z. Anorg. Chem.* **255**, 195 (1947).

[103] Hall, C. E., *J. Appl. Phys.* **19**, 271 (1948).

[104] Donnet, J. B. and J. C. Bouland, *Rev. Gén. du Caoutchouc* **41**, 407 (1964).

[105] Heckman, F. A. and D. F. Harling, *Rubb. Chem. Tech.* **39**, 1 (1966).

[106] Hess, W. M., L. L. Ban, F. J. Echert, and V. Chirico, *Rubb. Chem. Tech.* **41**, 356 (1968).

[107] Donnet, J. B., J. Schultz and A. Eckhardt, *Carbon* **6**, 781 (1968).

[108] Heidenreich, R. D., W. M. Hess and L. L. Ban, *J. Appl. Cryst.* **1**, 1 (1968).

[109] Ergun, Sabri, *Carbon* **6**, 141 (1968).

[110] Marsh, P. A., A. Voet, T. J. Mullens, and L. D. Price, *Rubb. Chem. Tech.* **43**, 470 (1970).

[111] Ban, L. L. and W. M. Hess, *Proc. Annu. Meet. Elect. Microsc. Soc. Am.* **26th**, 256 (1968).

[112] Harling, D. F. and F. A. Heckman, *Mater. Plast. Elastomeri* **35**, 80 (1969).

[113] Briggs, D. and M. P. Seah,"*Practical Surface Analysis*," pp. 5-8, John-Wiley & Sons, Chichester, England 1983.

[114] *Ibid*, pp. 519-520.

[115] Garten, V. A. and D. E. Weiss, *Aust. J. Chem.* **8**, 68 (1955).

[116] Treptau, M. H., H. Zoheidi and D. J. Miller, *ACS Div. Fuel Chem. Prepr.* **31(3)**, 150 (1986).

[117] Smith, J. M. and H. C. Van Ness,"*Introduction to Chemical Engineering Thermodynamics*," 3rd ed., p. 390, McGraw Hill Book Co., New York, 1975.

[118] Bone, W. A. and D. S. Jerdan, *J. Chem. Soc.* **71**, 41 (1897).

[119] *Ibid* **79**, 1042 (1901).

[120] Pring, J. N. and R. S. Hutton, *Ibid* **89**, 1591 (1906).

[121] Bone, W. A. and H. F. Coward, *Ibid* **93**, 1975 (1908).

[122] Pring, J. N., *Ibid* **97**, 498 (1910).

[123] Cao, J. R. and M. H. Back, *Carbon* **20**, 505 (1982).

[124] Blackwood, J. D., *Aust. J. Chem.* **12**, 14 (1959).

[125] Pring, J. N. and D. M. Fairlie, *J. Ind. Eng. Chem.* **4**, 812 (1912).

[126] Ibid, *J. Chem. Soc.* **101**, 91 (1912).

[127] Browning, L. C. and P. H. Emmett, *J. Am. Chem. Soc.* **73**, 581 (1951).

[128] Saunders, S. W., *J. Phys. Chem.* **28**, 1151 (1924).

[129] Levine, I. N.,"*Physical Chemistry*," p. 157, McGraw Hill Book Co., New York, 1978.

[130] Himmelblau, David M.,"*Basic Principles and Calculations in Chemical Engineering*," 4th ed., pp. 583-586, Prentice-Hall Inc., Englewood Cliffs, New Jersey, 1982.

[131] Squires, A. M., *Trans. Inst. Chem. Engrs.* **39**, 3 (1961).

[132] Zielke, C. W. and E. Gorin, *Ind. Eng. Chem.* **47**, 820 (1955).

[133] Blackwood, J. D., *Aust. J. Chem.* **15**, 397 (1962).

[134] Blackwood, J. D. and D. J. McCarthy, *Ibid* **19**, 797 (1966).

[135] Shaw, J. T., *National Coal Board Gasification Note* **No. 29** (1977).

[136] Satterfield, C. N.,"*Mass Transfer in Heterogeneous Catalysis*," p. 231, Krieger Publishing Company, Huntington, N.Y., 1981.

[137] *Ibid*, pp. 133-139.

[138] Thiele, E. W., *Ind. Eng. Chem.* **31**, 916 (1939)

[139] Mantell, C. L.,"*Carbon and Graphite Handbook*," p. 21, Interscience Publishers, John Wiley & Sons Inc., N.Y., 1968.

[140] Wilke, C. R. and C. Y. Lee, *Ind. Eng. Chem.* **47**, 1253 (1955).

[141] Boyd, C. A., N. Stein, V. Steingrimson, and W. F. Rumpel, *J. Chem. Phys.* **19**, 548 (1951).

[142] Marrero, T. R. and E. A. Mason, *J. Phys. Chem. Ref. Data* **1**, 3 (1972).

[143] Satterfield, C. N.,"*Mass Transfer in Heterogeneous Catalysis*," pp. 33-42 and 157, Krieger Publishing Company, Huntington, N.Y., 1981.

[144] Graham, D., *J. Phys. Chem.* **61**, 1310 (1957).

[145] Hart, P. J., F. J. Vastola and P. L. Walker Jr. *Carbon* **5**, 363 (1967).

[146] Phillips, R., F. J. Vastola and P. L. Walker Jr. *Ibid* **8**, 197 (1970).

[147] Dollimore, J., C. M. Freedman, B. H. Harrison and D. F. Quinn, *Ibid*, 587.

[148] Levine, Ira N.,"*Physical Chemistry*," p. 516, McGraw Hill Book Co., New York, 1978.

[149] Mims, C. A., R. T. K. Baker and J. J. Chludzinski, *ACS Div. Fuel Chem. Prepr.* **28(1)**, 71 (1983).

[150] Roscoe and Schorlemmer,"*Treatise on Chemistry*," (1883).

[151] Fox, D. A. and A. H. White, *Ind. Eng. Chem.* **23**, 259 (1931).

[152] Cerfontain, M. B. and J. A. Moulijn, *Fuel* **65**, 1349 (1986).

[153] Huhn, F., J. Klein and H. Juntgen, *Fuel* **62**, 196 (1983).

[154] Yokoyama, S., K. Miyahara, K. Tanaka, J. Tashiro, and T. Takukuwa, *Nippon Kagaku Kaishi* **6**, 974 (1980).

[155] Mims, C. A. and J. K. Pabst, *ACS Div. Fuel Chem. Prepr.* **25**, 258 (1980).

[156] Hashimoto, K., K. Miura, J. J. Xu, and A. Watanabe, *Chem. Lett.*, 555-556 (1984).

[157] Sams, D. A., T. Talverdian and F. Shadman, *Fuel* **64**, 1208 (1985).

[158] Kapteijn, F., J. Jurriaans and J. A. Moulijn, *Fuel* **62**, 249 (1983).

[159] Tromp, P. J. J. and E. H. P. Cordfunke, *Thermochimica Acta* **77**, 49 (1984).

[160] Ferguson, E., R. Schlogl and W. Jones, *Fuel* **63**, 1048 (1984).

[161] Kuhn, L. and H. Plogmann, *Fuel* **62**, 205 (1983).

[162] Formella, K., P. Leonhardt, A. Sulimma, K.-H. van Heek, and H. Juntgen, *Fuel* **65**, 1470 (1986).

[163] Bruno, G., L. Carvani and G. Passoni, *Ibid*, 1473.

[164] Puri, B. R. and R. S. Hazra, *Carbon* **9**, 123 (1971).

[165] Froment, G. F. and K. B. Bischoff,"*Chemical Reactor Analysis & Design*," pp. 178-184, John Wiley & Sons, New York, N.Y., 1979.

[166] Wood, B. J. and K. M. Sancier, *Cata. Rev. Sci. Eng.* **26**, 233 (1984).

[167] Wigmans, T., R. Elfring and J. A. Moulijn, *Carbon* **21**, 1 (1983).

[168] Rao, Y. K., A. Adjorlolo and J. H. Haberman, *Carbon* **20**, 207 (1982).

[169] Wigmans, T., J. C. Goebel and J. A. Moulijn, *Carbon* **21**, 295 (1983).

[170] Harker, H, *Proc. 4th Biennial Conf. Carbon*, pp. 125-139 (1959).